TAMPEREEN TEKNILLINEN YLIOPISTO
TAMPERE UNIVERSITY OF TECHNOLOGY

Matti Viikinkoski

Shape Reconstruction from Generalized Projections

Julkaisu 1358 • Publication 1358

Tampere 2015

Tampereen teknillinen yliopisto. Julkaisu 1358
Tampere University of Technology. Publication 1358

Matti Viikinkoski

Shape Reconstruction from Generalized Projections

Thesis for the degree of Doctor of Philosophy to be presented with due permission for public examination and criticism in Tietotalo Building, Auditorium TB214, at Tampere University of Technology, on the 8th of January 2016, at 12 noon.

Tampereen teknillinen yliopisto - Tampere University of Technology
Tampere 2015

ISBN 978-952-15-3665-6 (printed)
ISBN 978-952-15-3673-1 (PDF)
ISSN 1459-2045

Abstract

In this thesis we develop methods for recovering the three-dimensional shape of an object from generalized projections. We particularly focus on the problems encountered when data are presented as discrete image fields. We demonstrate the usefulness of the Fourier transform in transferring the image data and shape model projections to a domain more suitable for gradient based optimization. To substantiate the general applicability of our methods to observational astronomy, we reconstruct shape models for several asteroids observed with adaptive optics, thermal infrared interferometry, or range-Doppler radar. The reconstructions are carried out with the ADAM software package that we have designed for general use.

Preface

The research presented in this thesis has been carried out in the department of mathematics at Tampere University of Technology during the years 2010-2015.
I am extremely grateful to my supervisor, Professor Mikko Kaasalainen, for continuous encouragement and guidance.
I would like thank my thesis pre-examiners, Professor Jari Kaipio and Professor Otmar Scherzer, for valuable comments and suggestions.
I also wish to thank Josef Ďurech and Marco Delbo for discussions and advice.

Tampere, November 25, 2015

Matti Viikinkoski

Contents

1 Introduction and background

Recovering the shape of a three-dimensional object from observations is a problem of fundamental importance. Applications include medical imaging, machine vision, pattern recognition, remote sensing, and astronomy, to name just a few. Depending on the type of observations, the problem is called shape from shading (Zhang et al., 1999), structure from motion (Favaro and Soatto, 2007), or more generally, geometric tomography (Gardner, 2006). All of these are examples of generalized projections (Kaasalainen and Lamberg, 2006). As its name implies, a generalized projection is a generalization of the usual geometric projection operator, projecting a 3-D model onto a 1-D or 2-D space taking into the account illumination and the scattering effects. For instance, a pixelated 2-D thermal flux map of a surface, whose temperature depends on solar insolation and the heat conductivity of subsurface layers, is an example of generalized projection operator considered in this thesis. This is a typical ill-posed problem in the sense of Hadamard, since the observations do not contain high frequency information and are corrupted by noise. Inverting the shape directly leads to suboptimal results, as the noise present in observations is amplified during the shape optimization process. Regularization methods can be used to introduce additional constraints into an ill-posed problem, making the reconstruction of the shape solution tractable. Usual assumptions include smoothness or topology constraints. For example, an expected shape of an organ in medical imaging inferred from statistical analysis can be used as a prior to convert the inherently ill-posed problem into conditionally well-posed one.

In this thesis, we consider the problem of reconstructing shape from pixel image fields, which result from generalized projections combined with low-pass filtering and sampling operators. While the forward problem is straightforward enough, recovering shape information from pixels is complicated, especially when the observation geometries in a coordinate system fixed to the surface are not known a priori. Direct comparison between the pixel values of data image and the projected shape model is ineffective, since the non-negligible pixel size requires the integration of intensity over a finite area corresponding to the pixel, destroying analytical gradient information. Information can be retained by examining how the shape model is projected within the grid defined by pixel boundaries. However, this method is often suboptimal, as it is sensitive to the choice of initial offset between the projected model and the data image. A more efficient approach is to delocalize pixels by transferring both the projected model and the data into Fourier domain, converting the pixelated image into a continuous complex-valued function on the frequency domain, where the pixel size corresponds to the highest spatial frequency of interest. The transformation to Fourier domain facilitates the description of the reconstruction process in such a compact way that the difference between different data modes is often only the instrument-specific projection mapping. For instance, we will demonstrate that the Fine Guidance Sensor data from the Hubble space telescope can be processed with the same algorithm that is used for adaptive optics images, which is not evident from their description on the spatial domain.

The choice of correct shape support is vital in shape reconstruction. Typically, surface representations can be divided into two categories: implicit and parametric. Using implicit representation

leads naturally to level set methods (Osher and Fedkiw, 2006), which describe the shape using a signed distance function. Parametric representations define the shape as a linear combination of basis functions. The generality of level set methods is sometimes an impediment if the topology of the shape is known a priori. Moreover, extracting the boundary of a shape described as a level set of a function can be computationally demanding. For these reasons, parametric representations are used in this thesis. However, the methods developed here do not depend on a particular shape description.

The reliability of reconstruction is an another problem of equal importance. While it is relative easy to construct a shape fitting the available data, it is nontrivial to gauge the reliability of the shape solution. A straightforward approach by the Markov Chain Monte Carlo (MCMC) sampling from the posterior distribution is inefficient partially due to large number of parameters required for shape representation. In addition, the error distribution is usually unknown. The MCMC method can produce overly optimistic reliability estimates due to the fact that the large variations of shape parameters can cause inadmissible (e.g., self-intersecting) shapes, forcing the procedure to focus on regions of shape variation that are too small. Moreover, the posterior distribution of shape parameters does not tell us much about the reliability of shape model with respect to data, but only about the variability of parameters within one particular shape support. There could be shapes that fit the data better, but cannot be represented by the selected shape support. The partial solution advocated in this thesis is to use several different shape representations and regularization methods: it is conceivable that all the representations should produce similar shapes if the solution is well constrained by the data. A lack of resemblance between different shape solutions indicates that the shape is not well-determined by the data.

Asteroids are remnants of the early solar system. As most of them are not massive enough to be crushed into a spherical form by gravity, they are manifested almost in any shapes and compositions, moulded by impacts and collisions with other bodies. Due to their richness of structure, asteroids are ideal targets for shape reconstruction methods. Moreover, the shapes of asteroids have scientific importance, as they contain important information about the history and evolution of the solar system. Also, precise orbit determination requires accurate knowledge of the shape, as anisotropic thermal emissions from an asteroid's surface can effect a net force, causing changes in the orbit of the asteroid and potentially nudging asteroids to Earth crossing orbits.

A wide range of astronomical instruments can be used for observing asteroids, for instance disk-integrated photometry, adaptive optics, range-Doppler radar, and thermal infrared interferometry. Moreover, the coverage of one observation session alone is seldom sufficient for 3-D reconstruction, necessitating methods for the integration of widely different, complementary data sources into a coherent shape solution. Additionally, we demonstrate that the methods developed in this thesis may be applied to observations with the Atacama Large Millimeter Array, facilitating 3-D shape reconstruction from thermal infrared data.

This thesis is also intended to serve as a sufficiently self-contained handbook for end-users wishing to use the methods described here. Thus we include some technical details not present in the attached papers, some of which are given in appendices. Moreover, the software package used for reconstructing the shape models in chapter 6 is freely available (Viikinkoski, 2015).

In addition to the publications listed on the next page, results discussed in the thesis are also presented in Ďurech et al. (2012) and Ďurech et al. (2015), in both of which Matti Viikinkoski is a co-author.

2 List of Publications

I Kaasalainen M. and Viikinkoski M. Shape reconstruction of irregular bodies with multiple complementary data sources. *Astronomy & Astrophysics* 543 (2012):A97

II Viikinkoski M. and Kaasalainen M. Shape reconstruction from images: Pixel fields and Fourier transform. *Inverse Problems and Imaging* 8, no. 3(2014) 885-900

III Viikinkoski M., Kaasalainen M. and Ďurech J. ADAM: a general method for using various data types in asteroid reconstruction. *Astronomy & Astrophysics* 576 (2015):A8

IV Viikinkoski M., Kaasalainen M., Ďurech J., Carry B., Marsset M., Fusco T., Dumas C., Merline, W. J., Yang, P., Berthier J., Kervalla, P. and Vernazza, P. VLT/SPHERE- and ALMA-based shape reconstruction of asteroid (3) Juno. *Astronomy & Astrophysics* 581 L3 (2015)

Author's contributions to the coauthored publications:

In I, the author wrote the code used for the shape modelling and generated the models of asteroids Kleopatra and Hermione.

In II, the author developed the Fourier transform method for the shape reconstruction.

In III, the author extended the method developed in the previous article and generated the shape models of various asteroids. The program used for shape modelling was written by the author.

In IV, the author applied the ADAM procedure to the thermal and the adaptive optics observations of asteroid Juno and generated the shape model.

The publication I was partially written by the author, while the publications II-IV were mostly written by the author.

3 Shape support and regularization

3.1 Shape support

The choice of shape representation is an important part of shape modelling. While there are several different representations with attractive properties (e.g. implicit surfaces), the computation of shadowing and lighting effects requires the discretization and meshing of the surface by facets. Thus an effective approach is to represent a shape as a polytope with triangular facets, where the vertex locations are given by the parametrization. This reduces the question of shape representation to the choice of parametrization for the vertex coordinates. Assuming the typical asteroid surface is homeomorphic to the unit sphere, we can consider each coordinate as a function on the sphere, and choosing a suitable basis for functions, expand coordinate functions using this basis. This approach is straightforward to generalize to multiple bodies such as binaries. Typical such bases are spherical harmonics, spherical wavelets, and spherical splines. Our experiments suggest that parametrizations which expand each coordinate function separately tend to produce suboptimal results since they ignore the geometric dependencies and constraints between coordinates when considering surfaces represented by non-tangled meshes. Thus we have found it useful to consider two parametrized but conceptually different shape supports: octantoids based on spherical harmonics, and subdivision surfaces.

3.1.1 Octantoids

Our aim is to find a general surface parametrization for the reconstruction of non-starlike shapes from generalized projections. A popular approach is the usual spherical harmonics representation in which each coordinate function is represented independently as a spherical harmonics series (e.g. Zacharopoulos et al., 2006). However, while this parametrization is powerful enough to represent any shape that can be parametrized on the unit sphere S^2 (with sufficient continuity properties), it requires excessive smoothness regularization during the inversion process. What is more, the actual topology of the mesh of the evaluation points on the surface may change (which does not happen in the starlike case): the mesh can cross itself and become "tangled" as its vertices are allowed to move freely. Thus, instead of trying to find a regularization method to stabilize the surface topology, we decided to try a different approach by finding a representation that is general enough to represent non-starlike asteroid shapes, yet more stable than the usual spherical harmonics representation in the inversion process.

We consider surfaces that may be represented in the form

$$\mathbf{x}(\theta,\varphi) = \begin{cases} x(\theta,\varphi) = & e^{a(\theta,\varphi)} \sin\theta\cos\varphi, \\ y(\theta,\varphi) = & e^{a(\theta,\varphi)+b(\theta,\varphi)} \sin\theta\sin\varphi, \\ z(\theta,\varphi) = & e^{a(\theta,\varphi)+c(\theta,\varphi)} \cos\theta, \end{cases} \tag{3.1}$$

where a, b and c are conveniently expressed as linear combinations of the (real) spherical harmonic functions $Y_l^m(\theta,\varphi)$, with coefficients (a_{lm}), (b_{lm}) and (c_{lm}), respectively. The coordinates (θ,φ),

$0 \le \theta \le \pi$, $0 \le \varphi < 2\pi$, parametrize the surface on the unit sphere S^2 but not represent any physical directions such as polar coordinates. We use the exponential representation to ensure that the generalized radii e^a, e^{a+b}, e^{a+c} are all positive. As usual, the Laplace series for a, b, c are useful for keeping the number of unknowns; i.e., the coefficients of Y_l^m, small and the surface smooth. If $b = c = 0$, this representation is the usual starlike one with the radius $\exp(a)$, but we have found that even if the target is starlike, the octantoid form allows the capture of detail better, and b and c can be represented with considerably fewer terms than the main function a. The number of shape parameters is thus between the $(l_{\max} + 1)^2$ of the starlike case and $3(l_{\max} + 1)^2$, when $l_{\max}$ is the largest degree of the function series. It is clear that our representation is more restrictive than the general spherical harmonics representation, for the coordinate functions cannot change sign within each S^2-octant. We call shapes that can be represented in the form (3.1) *octantoids*. For a body to be an octantoid, it must be possible to choose the origin (inside the body) and coordinate axes such that if the body is cut along the coordinate planes, there is only one piece from each octant (and the pieces join together smoothly). For example, the ellipsoid is the simplest octantoid, as it can be represented in the form (3.1) by choosing functions a, b and c to be constants so that the semiaxes are the generalized radii. A curved banana is an example of a strongly non-starlike octantoid. From irregular small asteroids to planets, the currently known shapes of solar system can be well-approximated by octantoids. A non-octantoid body is typically made of sculpted material with great tensile strength and it has a markedly twisted shape, whereas processes guided by gravitation (accumulation etc.) tend to favour octantoid shapes.

The drawback of this representation is its globality: one might want less smoothness regularization in some regions than in others. When more local control is desired (e.g., a feature clearly visible in fly-by images or in radar), the representation (3.1) may be expanded with spherical splines or spherical wavelets to provide local detail without affecting the global shape. Depending on the desired level of resolution and the non-starlike irregularity of the surface, the number of free function series coefficients is typically between 50 and 300 from low- to mid-resolution. Function series are seldom useful for high resolution, where one may ultimately want to adjust the position of each vertex separately.

3.1.2 Subdivision control points

Subdivision surfaces offer local control more than global representations like function series. Beginning with an initial set of vertices and corresponding triangles, called a control mesh, the surface is iteratively refined by adding new vertices and computing new positions for old vertices. The vertex coordinates of the control mesh form the parameter set defining the surface. Each subdivision step smoothes out the surface in a higher level of resolution. Well-behaving subdivision schemes converge to a smooth limit surface.

We describe the Loop subdivision scheme (Loop, 1987). Considering a vertex p with immediate neighbours $p_0, \ldots, p_{n-1}$, the subdivision method first creates new vertices by splitting each edge:

$$q_i = \frac{3p + 3p_i + 3p_{i-1} + p_{i+1}}{8}, \qquad i = 0, \ldots, n-1, \tag{3.2}$$

where the indices should be interpreted as modulo n. After the vertex creation step, the position of the vertex p is refined:

$$p' = (1 - n\beta)p + \beta \sum p_i. \tag{3.3}$$

The multiplier β is usually chosen to be

$$\beta = \frac{1}{n}\left[\frac{5}{8} - \frac{(3 + 2\cos(2\pi/n))^2}{64}\right], \tag{3.4}$$

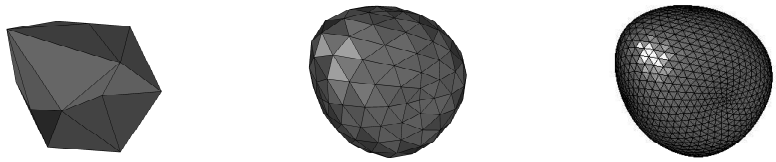

Figure 3.1: Original control mesh (left) with 18 vertices (54 coordinates) as the shape parameter set and 32 facets, after two $\sqrt{3}$-subdivision steps (middle), and after four subdivision steps (right).

but other choices are also possible. The limit surface is smooth; C^2 at the ordinary vertices (i.e. vertices that have 6 neighbours) and C^1 at extraordinary vertices. The number of free control points for model rendering is similar to or somewhat lower than the number of function series coefficients (for a comparable level of resolution).

The main computational aspect with subdivision methods is that the number of facets increases exponentially with the number of divisions. After n subdivision steps, each facet that has been divided has produced 4^n subfacets. An alternative scheme to Loop subdivision is the $\sqrt{3}$-subdivision (Kobbelt, 2000). Instead of splitting the edges, the $\sqrt{3}$-scheme subdivides facets by inserting a new vertex to the facet centroid and connecting it to the vertices of the facet (Fig. 3.1). The main attraction of the $\sqrt{3}$-subdivision compared to the Loop subdivision is the slower increase (3^n) of facets, while performing similarly in the limit.

In practice, it is usually a good idea to choose the initial control mesh to be an ellipsoid or a scaled convex surface obtained from lightcurve inversion, with a suitable number of vertices for the mesh. The subdivision surface is more sensitive to the size of the initial shape than the octantoids; the term a_{00} in the representation (3.1) controls the scale of the shape, while all the parameters of the subdivision surfaces have only a local effect. Thus it may be beneficial to introduce a global scaling term to facilitate faster convergence. The number of subdivision steps should be chosen carefully: while each subdivision increases resolution and stability by spreading the influence of each parameter to a larger number facets, the computational burden grows exponentially. Instead of subdividing all the facets, better performance may be obtained with adaptive subdivision, where only facets benefiting from increased resolution are subdivided. However, how to do this automatically during optimization is not obvious. A heuristic inclusion of surface regions to be refined based on a ranking of the improvement of the fit is one possibility (cf. the χ^2-sensitivity map of Kaasalainen and Viikinkoski, 2012); visual inspection of the model fit and a graphical user interface can guide in this.

3.2 Regularization

In this thesis, it turns out that finding a feasible regularization method is typically the most delicate part of problem solving. Ideally, both the shape representation and regularization method should be chosen to complement each other. The shape support should be general enough to represent probable shapes, and the regularization should prevent unrealistic or degenerate shapes while, at the same time, reveal the features present in the data.

Subdivision surfaces have somewhat different smoothness properties in this regard. It is well known that the Loop subdivision converges to a smooth surface, so each subdivision step will produce a smoother result. However, it is computationally expensive to take a large number of subdivision steps. Therefore it is advantageous to combine a few, usually two or three, subdivision steps with mesh-based regularization methods.

While not strictly necessary, it is convenient to assume that the triangular mesh representing the shape forms a manifold. This assumption makes the checking of shadowing and illumination both conceptually and computationally simpler. It is imperative to avoid self-intersections, as they introduce errors to the fitting process. One approach is to explicitly check for intersecting facets and retriangulate if required. However, triangulation and intersection tests are costly, and usually optimization steps leading to self-intersections are suboptimal. A better approach is to prevent self-intersections in the first place.

Regularization methods used for shapes may be divided into three different categories: methods depending on the parametrization of the shape, methods using the triangular mesh that independent of parametrization, and finally regularization methods restricting shape using the physical principles.

3.2.1 Octantoid regularization

For octantoids, the choice is remarkably easy. The usual representation for starlike shapes can be obtained by setting $b = c = 0$ in the parametrization (3.1). If we think of starlike surfaces as our basic "stable" shapes, an intuitively obvious measure for shape complexity is a weighted norm of the coefficients $\{b_{lm}\}$ and $\{c_{lm}\}$ (and possibly $\{a_{lm}\}$). We thus define

$$\eta = \sum_{l,m} l(b_{lm}^2 + c_{lm}^2), \quad \eta_0 = \sum_{l,m} l(a_{lm}^2 + b_{lm}^2 + c_{lm}^2). \tag{3.5}$$

We note that for an ellipsoid $\eta = \eta_0 = 0$ as the only nonzero coefficients are a_{00}, b_{00}, and c_{00}. This reflects the compact information content of the octantoid parametrization: representing an ellipsoid in the more usual starlike formulation with $b = c = 0$ would require an infinite spherical harmonics series for a. Using η_0 also formally solves the nonuniqueness problem of the choice of (θ, φ): for a given octantoid, the optimal parametrization is the one with the smallest η_0 (when the spherical harmonics series are truncated at some $l_{\max}$).

3.2.2 Mesh regularization

Since the octantoid regularization is restricted to octantoids, more general regularization methods independent of parametrization are required. Many iterative mesh smoothing methods (see e.g. Alliez and Lévy, 2010) may be used for regularization by using the size of iterative step as a measure of mesh quality, resulting inhibition of optimization steps increasing the measure. However they often tend to oversmooth the shape, hiding important features present in the data.

The regularization measure (3.5) mostly affects the global surface shape. In some cases, a regularization method for smoothing out local irregularities is required. We define a local smoothing regularization as in Kaasalainen (2011) as follows:

$$\gamma_1 = \frac{1}{\sum_i A_i} \sum_{i\ j} A_j(1 - \nu_i \cdot \nu_j), \tag{3.6}$$

where A_i is the area of the facet i and ν_i its unit normal vector. The sum is over all those facets j that are adjacent to the facet i and tilted above its plane. In effect, this regularization prefers locally convex features.

Regularization based on dihedral angles penalizes large angles between adjacent facet normals; i.e., the regularization prefers planar regions. We thus want to minimize

$$\gamma_2 = \sum_{i,j\in\mathcal{T}} w_{ij}(1 - \nu_i \cdot \nu_j), \tag{3.7}$$

where $\mathcal{T}$ are the facets of the mesh, and ν_k is the unit normal vector corresponding to the facet k. The sum is over all those facets j that are adjacent to the facet i, and the weights w_{ij} are usually chosen to be unity. As a special case, we may suppress only concave features, obtaining the usual convex regularization.

To prevent degenerate facets and maintain a homogeneous mesh, it is advantageous to inhibit large variations in facet areas:

$$\gamma_3 = \sum_i \left(\frac{A_i}{\bar{A}} - 1 \right)^2 , \tag{3.8}$$

where $\bar{A}$ is the mean facet area of the polyhedron. In practice, the regularization functions η and γ_1 are sufficient for octantoid surfaces, while γ_2 and γ_3 are useful for the subdivision surfaces. Unrealistically sharp angles can be prevented with γ_2, but too large a weight will inhibit convergence.

3.2.3 Physically based regularization

Finally, using the prior knowledge that the shapes we are modelling are rotating bodies affected by their own gravitational field, we may describe two additional regularization methods based on physical properties of the asteroids. We introduce a physical regularization function for non-monolithic bodies by constraining the gravitational slope so that steep rubble-pile slopes are avoided:

$$\gamma_4 = \frac{1}{\sum_i A_i} \sum_i A_i \left[1 - \nu_i \cdot \nabla\Phi(x_i) \right] ,$$

where x_i is the centroid of the facet i, and $\Phi(x)$ is the gravitational potential computed from the tetrahedra formed by the centroid of the body and the facet triangles (e.g Werner, 1994). The gravitational slope for the facet i is $\arccos(\nu_i \cdot \nabla\Phi(x_i))$. While the gravitational slope regularization is usually too constricting to be used during the optimization, it may be used to gauge the physical feasibility of the solution if constant density is assumed.

For a rotating body, the inertia tensor I determines its rotation state.The inertia tensor of polygonal model can be determined easily (Dobrovolskis, 1996) if constant density is assumed. The typical spin state of an asteroid corresponds to the minimal energy state, i.e. rotation with respect to the principal axis I_z of maximum moment of inertia (Pravec and Harris, 2002). Thus the inertia regularization should chosen to minimize the term

$$\gamma_5 = 1 - \cos(\theta)^2,$$

where θ is the angle between I_z and the rotation axis of the asteroid.

3.3 Reliability estimation

The octantoid representation or the subdivision mesh tends to produce shape estimates that can interpreted as “asteroid-like” surfaces, but it is not initially obvious which surface features of the model are actually present in the data, and which are the side effects of the shape support and the regularization used.

In statistical inversion, Markov chain Monte Carlo (MCMC) methods are used to obtain a reliability estimate for the model parameters. However, in our case, modelling and systematic errors usually dominate (Kaasalainen and Ďurech, 2006) and the error distribution is not known, making a statistical approach to the problem difficult. Moreover, the posterior distribution of

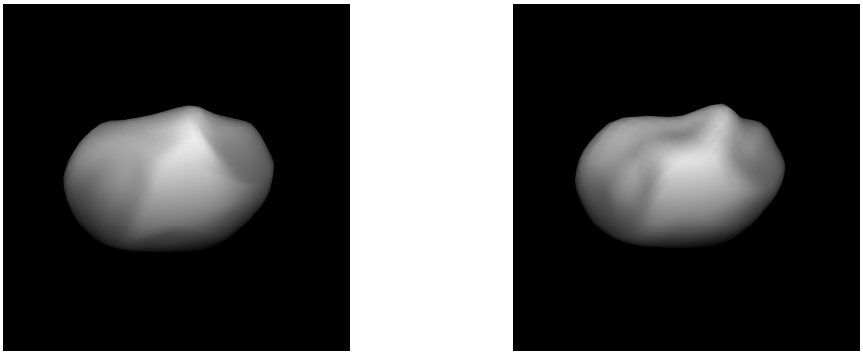

Figure 3.2: Model of asteroid (41) Daphne from adaptive optics images, reconstructed as a subdivision surface (left) and an octantoid (right).

shape parameters from MCMC will not really tell much about the reliability of the model with respect to data, but only about the distribution of the estimate within the adopted shape support. We have found that this could result in an overly optimistic conception of the reliability of the result, simply because the acceptable shape results cannot be probed widely enough using one shape support only. The Monte Carlo procedure focusses on regions of shape variation that are too small for both computational and geometric reasons. In addition, the computation of the model fit is time consuming if the data set and parameter space are large, making MCMC estimation computationally expensive.

To circumvent these obstacles, we have found the following approach fast and robust in practice. Any real feature of the model based on the data should also be present if another, independent model type such as a shape support is used. When model errors dominate, it is thus better to sample the "model space" within some goodness-of-fit χ^2 than the χ^2-space with some fixed model. As an example, shape models of the asteroid Daphne from adaptive optics images and photometry (see section 6.1), using both the octantoid representation and subdivision surfaces, are shown in Fig. 3.2. The models are quite similar and fit the data equally well, and their difference gives an idea of the real level of resolution. The MCMC probing with either shape support leads to small differences that are unrealistic(insignificant compared to those in Fig. 3.2). Even the shape-support test is likely to produce reliability limits that are too optimistic; the model error can be further enlarged by e.g. introducing random fluctuations in the scattering properties over the surface. This principle could be developed into a meta-level Monte Carlo procedure that probes the space of possible model types using latent parameters.

We conclude that shape sampling based on a fixed model type seems to lead to overly optimistic resolution with artificial details. A typical example of this is the radar model of the asteroid Itokawa that portrayed imaginary detail at the resolution level expected from the data while not capturing even the large-scale features. There was nothing wrong with the model fit to the data as such: the inverse problem was not unique (or very unstable) because of the restricted observing geometries and instrumental projection, but the constrained shape support of the program did not reveal this (Nolan et al., 2014; Ostro et al., 2005).

4 Shape reconstruction

In this chapter, we develop methods for reconstructing 3-D shapes from pixel fields. We present a projection method in the image plane that retains analytical partial derivatives with respect to shape parameters, making it possible to use gradient based optimization methods for minimizing the difference between the data and the model. While direct fitting of pixel values is straightforward and transparent, there are several problems with this approach. An alternative way is to transform from the image plane to the Fourier plane, converting the pixellated image into a continuous complex valued function on a frequency domain.

In the first sections, we describe a scattering model and an algorithm for facet visibility determination, followed by a general method for shape reconstruction in the image plane. After that we turn to the Fourier transform method, showing that the two-dimensional Fourier transform of the projected polyhedron and its derivatives can be calculated analytically. Finally, in the last section, we describe the All-Data Asteroid Modelling (ADAM) procedure. Detailed descriptions of the transformation matrices and derivative calculations are provided in the appendix.

4.1 Scattering laws and visibility

Model detail is ultimately constrained by the facet size. For visibility determination, we usually assume that a facet is the smallest unit: Every facet is either fully visible or invisible. An exception to this is considered in Kaasalainen and Viikinkoski (2012), where reconstruction from HST/FGS data in spatial domain is explored; in that case a facet is too coarse a unit for calculating the response of the instrument.

Let ω and ω_0 be, respectively, the viewing and the illumination directions; $\omega_0, \omega \in S^2$. Moreover, let ν the unit normal of the facet. As the surface is not necessarily convex, the facet may be occluded by other facets. The set of facets approximating the visible and illuminated portion $\mathcal{A}_+(\omega_0, \omega)$ of the surface can be determined by ray-tracing. A computationally fast form of this, approximate but sufficiently accurate for most of our purposes and easily refinable for higher accuracy, was given in Kaasalainen and Torppa (2001). We describe the algorithm in detail:

1. For each facet f with the vertices v_i, the unit normal ν and centroid c, we determine the set the facets $\mathcal{B}(f)$ that are potential blockers of the facet f: a facet g belongs to $\mathcal{B}(f)$ if
   - Some vertex w_i of the facet g is above the local horizon of the facet f: $\nu \cdot (w_i - c) > 0$, and
   - facet g is facing the facet f: $\nu_g \cdot (w_i - c) < 0$, where ν_g is the unit normal of the facet g.
2. The facet f is in $\mathcal{A}_+(\omega_0, \omega)$ if
   - the dot products $\omega \cdot \nu$ and $\omega_0 \cdot \nu$ both are positive, and

- the rays from the facet centroid to the directions ω and ω_0 do not intersect any other facet in the set $\mathcal{B}(f)$.

Note that the set $\mathcal{B}(f)$ does not depend on viewing or illumination directions; thus it needs to be recalculated only when the model changes. This facilitates a considerable reduction in the number of ray-triangle intersection tests.

Next, we consider how light scattering from a facet may be modelled. The model representation is a polyhedron that is projected onto some projection plane $(\xi, \eta) \in \mathbb{R}^2$ via a linear transformation (Kaasalainen, 2011; Kaasalainen and Lamberg, 2006). Let $\mathcal{P} : \mathbb{R}^3 \to \mathbb{R}^2$ be the operator for this linear mapping. Then the projection $\mathcal{P}T_i$ of each facet T_i is assigned a brightness factor B_i depending on the visibility, attitude, and surface scattering or radiation flux model of the facet. The scattering model $S(\mu, \mu_0, \alpha)$ is typically dependent on the cosines μ and μ_0 between the surface normal and, respectively, the viewing and illumination directions, and on the angle α between the latter two (Kaasalainen and Lamberg, 2006). Since the projection cosine μ is traditionally taken as a fixed factor in S, we write

$$B_i = \begin{cases} S_i(\mu, \mu_0, \alpha)/\mu, & \mu, \mu_0 > 0, \\ 0, & \text{otherwise.} \end{cases}$$

Typical scattering models are combinations of Lommel-Seeliger and Lambert scattering models (Kaasalainen and Torppa, 2001) and the Hapke model (Hapke, 1981). As far as their role in B_i is concerned, models of thermal surface radiation flux are essentially similar to the scattering models, except that they have a time-lag component as discussed in 5.5.

4.2 Reconstruction in the image plane

Using the same notation as in the previous section, the forward problem may be formulated as follows: For each point on the projection, we assign a factor $I(\xi, \eta) \in \{0, 1\}$, a piecewise constant integer function encoding the visibility and illumination (VI) condition of the point (ξ, η). This constitutes the generalized projection or image mapping. In principle, one could determine the exact projection polygons inside which $I(\xi, \eta) = 1$ by considering all intersections due to occluding facets (Kaasalainen, 2011). In practice, this is unnecessarily laborious, so we use the separate projections of the original polyhedron facets. Each facet is checked for VI as a whole by ray-tracing (see above), and the level of resolution can be controlled at will by dividing a facet into subfacets; for example, the radar imaging process usually requires greater accuracy than the thermal infrared. Thus we approximate, for each facet T_i,

$$I_i = \begin{cases} 1, & i \in \mathcal{A}_+(\omega_0, \omega), \\ 0, & \text{otherwise.} \end{cases}$$

Two polygons in a plane (a facet projection of a polyhedral shape model and a pixel frame) overlap, if any of their boundary lines intersect, or if any vertex of either is inside the other. For such cases, one finds all the intersection points, if any, and thus determines the boundary lines of the overlap polygon. The sum of the areas of all the overlap polygons inside a pixel frame, each multiplied by the factors $B_j I_j$ of the corresponding facet, then determine the model intensity P_i^{mod} of the pixel. The derivatives with respect to the vertex coordinates of the polyhedron, and hence the parameter gradients for efficient optimization, follow directly from this. We find the solution that minimizes $\|P^{\text{obs}} - P^{\text{mod}}\|$, where $P^{\text{obs/mod}}$ are the vectors that contain the observed and modelled pixel intensities. Since each feasible facet-pixel overlap pair must be checked, the computational

complexity is proportional to N^2, although the number of function-value computations is smaller than in the N^2 process of the FT sampling below.

We remark that it is possible just to sample the B_i at various points on the surface (or the image plane), and then use these samples to produce the model pixel intensities. However, though fast in computing the forward problem, this is not efficient in shape reconstruction. This is because now there are no analytical partial derivatives with respect to parameters only related to the position in the image plane (such as model size and offset factors, unless there is a significant point-spread function), and other shape parameters have derivatives only through the orientation of the local model surface patches.

4.3 Reconstruction in the Fourier plane

4.3.1 Fourier transform of projected polyhedron

Consider now doing the computations in the Fourier-transformed domain, the plane $(u, v) \in \mathbb{R}^2$. For practical purposes, we define our (two-dimensional) Fourier transform of some function $f(\xi, \eta)$ as follows:

$$\mathcal{F}(u, v) := \int_{\mathbb{R}^2} f(\xi, \eta) e^{-2\pi\imath(u\xi+v\eta)} d\xi d\eta.$$

The point here is that any integral transform that has the same basic properties as FT is suitable for our purposes, so constants and normalizations used in the definition are irrelevant. Indeed, some completely different transforms may be just as good, but we have found the FT approach to converge very well. Also, interferometric data are typically samples of a Fourier transform, given in the frequency (u, v)-plane, so the FT approach is ideal for such cases.

In the following, we use Green's theorem (see e.g. Riley et al., 2006): Let D a region in a plane bounded by a piecewise smooth, simple closed curve C. If L and M are functions on an open region containing D and having continuous partial derivatives, then

$$\iint_D \frac{\partial M}{\partial \xi} - \frac{\partial L}{\partial \eta} d\xi d\eta = \oint_C (L d\xi + M d\eta).$$

Letting $\mathcal{T}$ be the set of facets forming the polyhedron,

$$M(\xi, \eta) = -\frac{1}{2\pi\imath} \frac{u}{u^2 + v^2} e^{-2\pi\imath(u\xi+v\eta)} \text{ and } L(\xi, \eta) = \frac{1}{2\pi\imath} \frac{v}{u^2 + v^2} e^{-2\pi\imath(u\xi+v\eta)},$$

the transform integral can be written, by Green's theorem, as

$$\begin{aligned} \mathcal{F}(u, v) &= \sum_{T_i \in \mathcal{T}} \iint_{\mathcal{P}T_i} B_i \, I(\xi, \eta) e^{-2\pi\imath(u\xi+v\eta)} \, d\xi d\eta \\ &= \sum_{T_i \in \mathcal{T}} B_i \sum_j \frac{1}{2\pi\imath} \int_{\Gamma_{ij}} (L \, d\xi + M \, d\eta) \\ &:= \sum_i B_i \sum_j \mathcal{I}_{ij}(u, v), \end{aligned}$$

where Γ_{ij} are the boundary line segments defining the VI part of the projected facet $\mathcal{P}T_i$, oriented counterclockwise. In practice, these are the edges of entire projected facets (or subfacets) included in the sum depending on their I_i. The facet factor B_i can also include the intrinsic lightness

(albedo) of the local surface, and this can be left as a a free parameter (or a function over the surface). For $(u, v) = (0, 0)$, the Fourier transform is the total brightness of the image:

$$\mathcal{F}(0,0) = \sum_{T_i \in \mathcal{T}} \iint_{\mathcal{P}T_i} B_i \, I(\xi, \eta) \, d\xi d\eta = \sum_i B_i \sum_j \int_{\Gamma_{ij}} \xi \, d\eta,$$

i.e., the last sum is the area of the VI part of $\mathcal{P}T_i$.

For a line segment Γ_{ij} with end points (a, b) and (c, d), $\mathcal{I}_{ij}(u, v)$ can be written in a closed form by substituting the line equations

$$\xi = a(1 - t) + ct$$
$$\eta = b(1 - t) + dt,$$

where $t \in [0, 1]$, so that we have

$$\mathcal{I}_{ij}(u, v) = \frac{1}{4\pi^2(u^2 + v^2)} \frac{(b - d)u - (a - c)v}{(a - c)u + (b - d)v} (e^{-2\pi\imath(au+bv)} - e^{-2\pi\imath(cu+dv)}).$$

The special case where the denominator vanishes can be handled similarly. The summation over $\mathcal{I}_{ij}(u, v)$ can be reordered and speeded up by noting that each polygon edge in the interior is shared by two polygons, so a new factor $\tilde{B}$ can be taken to be the difference between the two B_i, and the edge term is computed only once. Note that this explicitly shows why most of the information in the image is indeed from the limb and shadow boundary curves discussed in Kaasalainen (2011) and Kaasalainen and Viikinkoski (2012). The values of $\tilde{B}$ for interior edges are usually close to zero (indeed, they vanish for the geometric scattering $B_i = const.$), so most of the weight is on the boundary edges. From the above expression, it is obvious that the integral has continuous partial derivatives with respect to the projected vertices, which depend linearly on the original vertices of the facet. Thus the Fourier transform has continuous partial derivatives with respect to the facet vertex coordinates

4.3.2 The ADAM algorithm

We can now write the FT reconstruction procedure as follows:

1. For each data image D_i and observation geometry $\mathcal{E}_i$, the two- dimensional Fourier transform $\mathcal{F}D_i(u, v)$ of D_i is sampled at a set of points $\{(u_{ij}, v_{ij})\}$, $j = 1 \ldots N_i$, on the spatial frequency plane. For pixel images, the transform can be computed by Eq. (4.3.1) when considering each pixel as a polygon, or by using fast Fourier transform functions for chosen grid points (but the time spent for $\mathcal{F}D_i(u, v)$ is irrelevant as most of the computations are for the trial models).

2. The shape parameters a_{lm}, b_{lm}, and c_{lm} are initialized such that Eq. (3.1) represents a sphere approximately equal in size to the target. The control mesh of the subdivision surface can be selected similarly.

3. For each observation geometry $\mathcal{E}_i$, the Fourier transform $\mathcal{F}M_i(u, v)$ of the corresponding projection image M_i of the model is calculated as described in the previous section, together with the partial derivatives of $\mathcal{F}M_i(u, v)$ with respect to the shape parameters.

4. An objective function χ^2 is formed, with the square norm of the complex-valued FT fit error:

$$\chi^2 = \sum_i \lambda_i \sum_{j=1}^{N_i} \left\| \mathcal{F}D_i(u_{ij}, v_{ij}) - e^{2\pi\imath(o_i^x u_{ij} + o_i^y v_{ij})} \mathcal{T}_i(u_{ij}, v_{ij}) \mathcal{F}M_i(u_{ij}, v_{ij}) \right\|^2 + \lambda\gamma^2$$

where (o_i^x, o_i^y) is the offset between the data image D_i and the model image M_i, and, by the convolution theorem, $\mathcal{T}_i$ is the Fourier transform of the point-spread function of the imaging system. The regularization term γ corresponds to Eq. (3.5). Additional regularization measures are also possible, e.g., local convexity, gravitational slope or the inertia tensor (see Sect. 3.2). Usually η, γ_1, and γ_3 are the best choices, as the physical regularization methods tend to restrict the shape too severely during the initial convergence. The weights λ_i assigned to the different data modes should reflect their relative reliability. Often it is not obvious a priori how the weights should be chosen, since different data sets can contribute conflicting information. A rigorous method for the optimal weighting of the data modes is provided by the maximum compatibility estimate (Kaasalainen, 2011).

For disk-integrated photometry, the goodness-of-fit measure is defined as in Kaasalainen and Torppa (2001). The occultation silhouettes (Ďurech et al., 2011) can also be included by using a procedure similar to the one described in the Appendix.

In addition, the intensity level of each data and model image must be normalized. Often it is enough to divide both model M_i and data image D_i by their respective mean intensities. Equivalently, writing

$$\chi^2 := \sum_{ij} \left\| \mathcal{D}_i(u_{ij}, v_{ij}) - \tilde{\mathcal{M}}_i(u_{ij}, v_{ij}) \right\|^2 + \lambda\gamma^2,$$

we have (Carry et al., 2010)

$$\chi^2_{\mathrm{rel}} = \sum_{ij} \left\| \frac{\mathcal{D}_i(u_{ij}, v_{ij})}{\langle \|D_i\| \rangle} - \frac{\tilde{\mathcal{M}}_i(u_{ij}, v_{ij})}{\langle \|\tilde{M}_i\| \rangle} \right\|^2 + \lambda\gamma^2,$$

where the mean $\langle\cdot\rangle$ is taken over $\{(u_{ij}, v_{ij})\}$, $j = 1 \ldots N_i$. However, sometimes it is better to allow the intensity level of each M_i to be a free parameter and use χ^2; this is useful in the case where the mean intensity of D_i is corrupted by excessive noise in the image background (this is typical for range-Doppler images). This causes the χ^2_{rel}-based solution to have a slightly wrong size to compensate for the "diluted" normalized intensity level inside the actual object region of D_i.

5. The shape parameters, spin vector direction, and the offsets (o_i^x, o_i^y) as well as the possible intensity level factors C_i minimizing χ^2 are determined with a suitable method such as the Levenberg-Marquardt algorithm.

The crux of the idea is that the Fourier transform of the plane-projected mesh of a model polytope is simple to compute analytically, and the partial derivatives with respect to vertex coordinates exist and can be straightforwardly given in a closed form. Since $\mathcal{F}^{-1}\mathcal{F} = \mathbb{I}$, FT retains all the information in the original image. We can list some particular advantages of the FT approach:

- The FT method algorithm is simpler than direct pixel fitting, and convergence of minimization is robust
- Information at any point in the frequency plane comes from all points in the image plane, which increases robustness
- FT sampling can be used to filter the image information at different frequency (i.e., resolution) scales
- Point-spread functions can easily be included into optimization

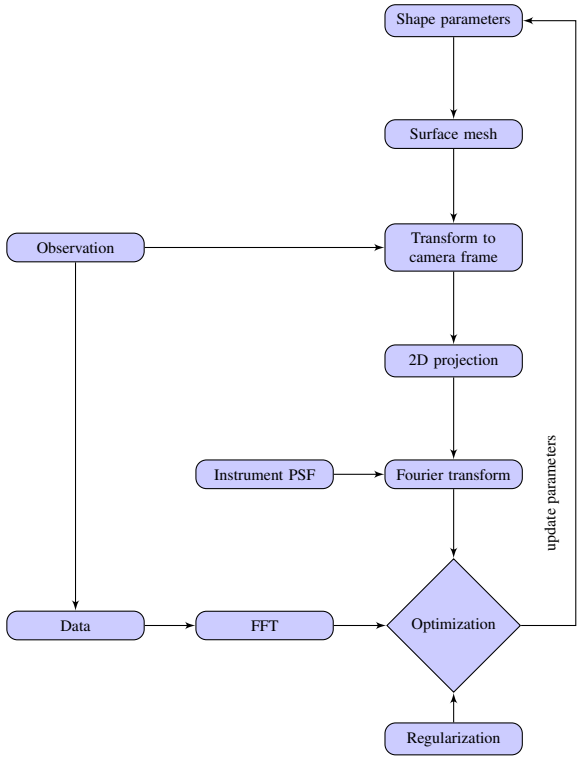

Figure 4.1: ADAM optimization algorithm as a schematic for one image type.

The downside of the FT method is increased computation time and complexity as we move from the sparse boundary curve to the two-dimensional Fourier transform of the projection image. For image fields with N relevant pixels, the boundary curve approach pertains to essentially $\sqrt{N}$ boundary elements and the computational complexity is proportional to N, whereas the complexity of the FT method is proportional to N^2. In all methods, much of computing time is, of course, spent on the same ray-tracing computations. In any case, the polyhedral and Fourier computations are trivially parallel. Each facet or each point on the (u, v)-plane can be considered separately, so the computations can be implemented very effectively on a graphics processing unit.

5 Typical projection operators in astrophysics

Following the development of the general reconstruction algorithm in the previous chapter, we take a closer look at the different generalized operators in astronomy and describe them in the detail required for the modeling.

5.1 Disk-integrated photometry

Disk-integrated photometry is the most abundant source of information on asteroids. A lightcurve (Fig. 5.1) is obtained by observing brightness variations of an asteroid over a time period. It has been shown (Kaasalainen and Torppa, 2001) that a convex model of the asteroid can constructed if enough observations with different viewing geometries are available. However, recovering non-convex features reliably is seldom possible with lightcurves only (Ďurech and Kaasalainen, 2003; Ďurech et al., 2012). On the other hand, lightcurves are crucial for enabling and completing the reconstruction when only few disk-resolved observations are available. Moreover, the inclusion of lightcurves into the inversion process has a regularizing effect that helps to stabilize the shape solution.

Using the notation of the previous chapter, the photometric operator, depending on the view and illumination directions ω and ω_0, can be written in the form

$$L(\omega_0, \omega) = \iint_{\mathcal{A}_+(\omega_0,\omega)} S(\mu_0, \mu, \alpha) d\alpha,$$

where S is a scattering model, and the integration is over the visible and illuminated part of the asteroid. Usually S is assumed to a linear combination of the Lommel-Seeliger and Lambert scattering models:

$$S = \mu\mu_0 \left(\frac{1}{\mu + \mu_0} + c \right),$$

where c is a constant.

Since ADAM utilizes photometric data in addition to disk-resolved data, we note that ADAM can be used to reconstruct a model using only photometric data (simply using only the photometric fit function from the toolbox). This is easy and fast to do (and the shape rendering is even faster than the standard convex inversion of lightcurves), but the result is inevitably unreliable: it is well known that even sizable non-convex shape features require high solar phase angles to show in disk-integrated data (Ďurech and Kaasalainen, 2003; Kaasalainen et al., 2001; Kaasalainen and Ďurech, 2006).

As an example, we show reconstructed shapes of the asteroid Golevka in Fig. 5.3, based on the data in Kaasalainen et al. (2001). Both the subdivision method and the octantoid-based model

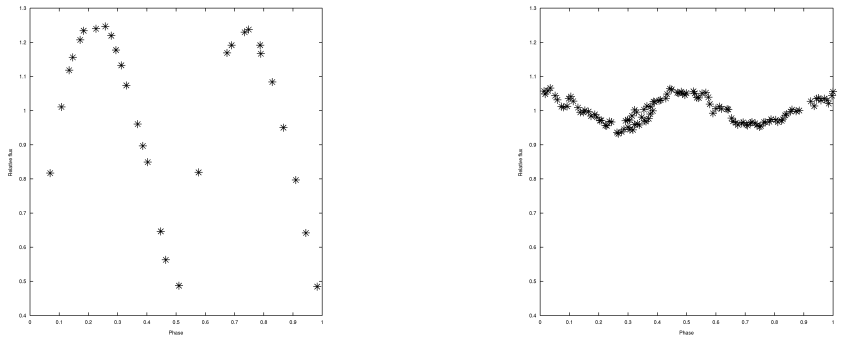

Figure 5.1: Typical relative magnitude optical lightcurves of an asteroid.

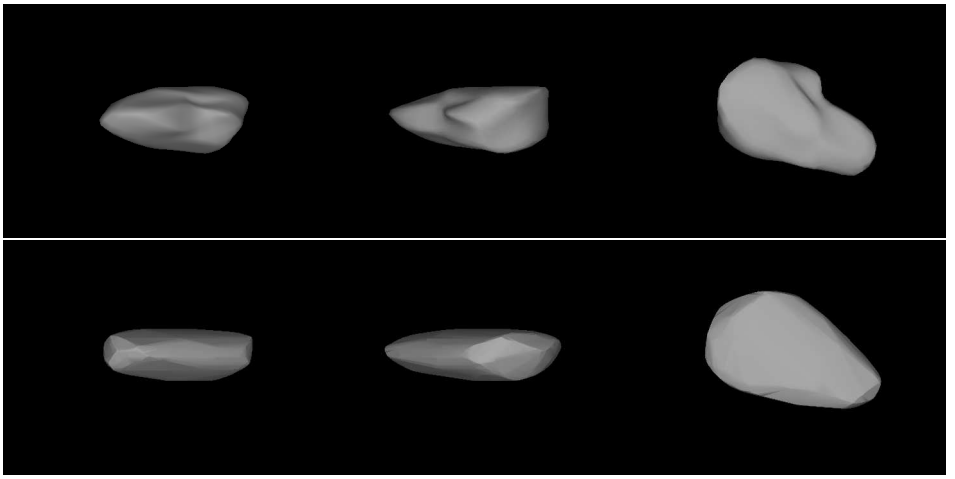

Figure 5.2: Asteroid (3103) Eger reconstructed from disk-integrated photometry. Exceptionally the nonconvex model(top) gives better fit than the convex model(bottom).

display additional detail not seen in the convex model. However, the details are not supported by the data: the convex model gives at least as good a fit as the non-convex, as is almost always the case with lightcurves (so far the only case of a better nonconvex model fit to photometry is that of the asteroid Eger in Ďurech et al., 2012). Indeed, with Golevka and other ground truth cases (maps from space probe missions), even the lightcurve fit with the correct shape and the scattering model assumed in inversion is not better than that with the convex model (Kaasalainen et al., 2001; Kaasalainen and Ďurech, 2006). This underlines the fact that, because of systematic errors, any best-χ^2 optimized solution that relies only on photometry is likely to miss the details.

While the convex model yields the best overall agreement with the radar-based Golevka model (see the comparison in Figs. 3 and 4 in Kaasalainen et al., 2002a), the non-convex models portray much of the general sharpness and ruggedness of the body even though their details are not correct. The convex shape presents something of a softened error envelope within which numerous local shape variations are possible (as if the target were seen unfocussed), while the non-convex representations are samplings of those variations. Their details coincide neither with each other nor with those in the radar-based model, but they are useful as illustrations and for probing the potential shape options (cf. the non-convex examples in Kaasalainen et al., 2004).

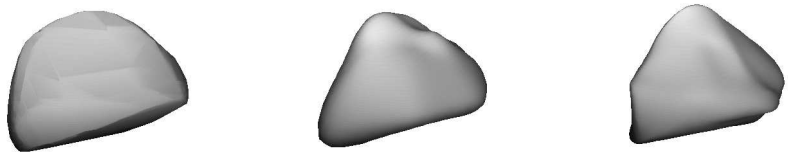

Figure 5.3: Asteroid (6489) Golevka reconstructed from disk-integrated photometry. From left to right: Convex, octantoid and subdivision surface.

5.2 One-dimensional projection operators

In the regime between disk-integrated and disk-resolved observations there are one-dimensional operators that project the plane-of-sky onto a line. Typical examples are the continuous-wave (CW) Doppler spectra that measure the distribution of the reflected power in frequency only (Fig. 5.4) , and the Fine Guidance Sensors (FGS) onboard the Hubble Space Telescope, measuring the brightness distribution along an instrument axis (Fig. 5.5). One-dimensional projections are seldom sufficient for actual shape reconstruction, but they may contain useful information about the object's size or indications about the bifurcated structure (Kaasalainen and Viikinkoski, 2012), and combined with other sources they facilitate shape inversion.

In both examples, the measurement can be written in the form

$$S(x) = \int I(\xi, \eta)\, P(x - \xi\cos\gamma - \eta\sin\gamma)\, \mathrm{d}\xi\, \mathrm{d}\eta, \tag{5.1}$$

where $I(\xi, \eta)$ is the plane-of-sky brightness (optical or radar) distribution of an object, P is the point-spread function of the instrument, and the angle γ corresponds to the rotation of the sensor in the image plane. In Kaasalainen and Viikinkoski (2012), the integral was evaluated using a Monte Carlo method: the projected model was sprinkled with uniformly distributed sampling points, and the integral was approximated as a sum over the visible and illuminated sampling points. Here we demonstrate how the Fourier transform method can be used to interpret the integral as a tomographic operator on the Fourier plane.

Taking the Fourier transform on both sides and using the projection-slice theorem (a slice of a 2-D FT along a line through the origin equals the 1-D FT of the projection of the original 2-D function onto a line in the same direction; see e.g. Bracewell (2003)), we get

$$\mathcal{S}(f) = \mathcal{I}(f\cos\gamma, -f\sin\gamma)\,\mathcal{P}(f), \tag{5.2}$$

where the calligraphic characters denote the Fourier transformed functions. Now it is obvious that $\mathcal{S}(f)$ is a slice of a Fourier transformed brightness distribution along a line through the origin, multiplied with the Fourier transform of the point-spread function. Moreover, this means that the same algorithm may be used to fit both FGS and adaptive optics data, and similarly both CW Doppler data and the range-Doppler images. In other words, we extract a one-dimensional Fourier transform from the 2-D model FT, and compare this with the 1-D FT formed from the data in the same way as in the full 2-D case.

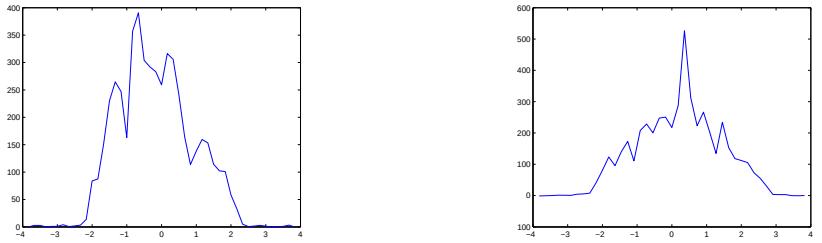

Figure 5.4: CW spectra of the asteroid ET_{70}. Vertical axis is the reflected power in units of the standard deviation and the horizontal axis is frequency in Hertz.

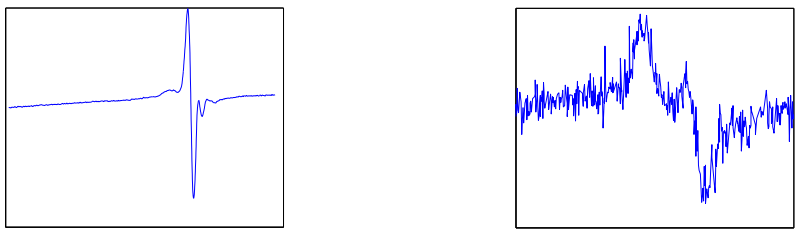

Figure 5.5: A typical PSF of the FGS instrument(left), and an observation of the asteroid Kleopatra with the FGS(right).

5.3 Adaptive optics

5.3.1 Image acquisition

An image of an unresolved star gives an approximation to the PSF of the telescope. In perfect conditions, the image formed by a point source is the Airy disk, and the system is then said to be diffraction limited. The first minimum of Airy pattern occurs approximately at the angular distance of $1.22\lambda/D$ radians, where λ is the wavelength of light and D the diameter of telescope. This is so called Rayleigh criterion for the minimum resolvable detail (Steward, 2012). In this case, the resolution is limited only by the diffraction of light.

In practice, this limit is attainable only from space-based telescopes; the resolution of Earth-based telescopes is limited by the atmosphere. The incoming wavefront from a point source is distorted by the atmospheric turbulence causing rapidly changing speckle patterns in the image plane. Long exposure imaging blurs the speckles into an image of size λ/r_0, where r_0 is so called Fried parameter. The Fried parameter models the typical size of moving cells of air caused the turbulence; each cell acts as an independent lens of diameter r_0. In effect, the highest attainable resolution is λ/r_0 even for telescopes with $D > r_0$. Usually, the value of Fried parameter varies around 10 cm for optical wavelengths. This corresponds to angular resolution of one arcsecond, making disk-resolved imaging of asteroids impossible. To quantify the deterioration of image quality, we can calculate the Strehl ratio: it is the ratio of peak intensity of the actual PSF to the peak of the diffraction limited Airy pattern. Typical, uncorrected Strehl ratio is the order of magnitude of 0.01.

Adaptive optics tries to correct the atmospheric distortion with a help of a computer-controlled deformable mirror. Using an unresolved reference star with close proximity to the asteroid, the degradation of the incoming wavefront can be analyzed, and the mirror is adjusted to counter the effect. This facilitates resolution approaching the diffraction limit of the telescope. The required

response time of the correction system is determined by the coherence time of the wavefront; it is proportional to r_0/v, where v is the average wind speed. At visible wavelengths, the coherence time of a few milliseconds is typical.

5.3.2 Deconvolution

Ideally, the adaptive optics system would be able to compensate for atmospheric distortions, and the remaining PSF would be the Airy pattern caused by diffraction. In practice, this is unattainable. The fitting errors, insufficient number of modifiable mirror elements, and finite response time of the optical system, result in an only partially corrected PSF. In the Fig. 5.6 a typical PSF is shown: the bright center spot is the corrected, diffraction-limited region, and the surrounding broad halo is the uncorrected part of the PSF. Usually the acquired adaptive optics images are deconvolved in order to decrease blurring. Since the deconvolution is an important problem, the literature is vast, see e.g. Jansson (2012). The deconvolution is a typical inverse problem; the system PSF is a low-pass filter attenuating high frequencies and thus the reconstruction must be carefully regularized to avoid the amplification of noise.

The ADAM algorithm uses a different approach. Instead of trying to deconvolve the data beforehand, the projected model convolved with the PSF P is fitted to the data:

$$\sum_j \left\| \mathcal{F}D(u_j, v_j) - \mathcal{F}P(u_j, v_j)\mathcal{F}M(u_j, v_j) \right\|^2 + \sum_i \lambda_i \gamma_i^2, \tag{5.3}$$

Where M is the projection of the model to the image plane corresponding the observation geometry, D the image, and (u_j, v_j) are the frequency points used for the fitting. The $\mathcal{F}$ is the two dimensional Fourier operator. The regularization terms γ_i, defined in the section 3.2, compensate for the amplification of high frequencies caused by the inversion process. This approach is simpler and more transparent than the usual separate deconvolution of data images. Moreover, potential uncertainties caused by the prior assumptions of deconvolution process and their effects to resulting images are hard to quantify.

Often, due to angular separation between the guide star and target, the actual PSF is not identical to the PSF of the reference star. The blind deconvolution problem where the PSF is only partially known is called myopic deconvolution. A popular algorithm for restoring extended objects is called MISTRAL (Hom et al., 2007; Mugnier et al., 2004). It estimates the image and the PSF, using a Bayesian approach, with a total variance prior preferring sharp edges and planar regions. In Fig. 5.6 is a typical raw image obtained from a telescope, and a MISTRAL deconvolved image of the same asteroid.

The current implementation of ADAM assumes that the PSF P is fixed. However, the procedure can be straightforwardly extended to handle myopic deconvolution: by adding a regularization term penalizing discrepancy between the current P and the initial PSF P', both the model and the PSF can be fitted concurrently. The PSF model may be either a discrete function defined on the frequency points, or a continuous function depending on few parameters, e.g. Drummond and Christou (2009).

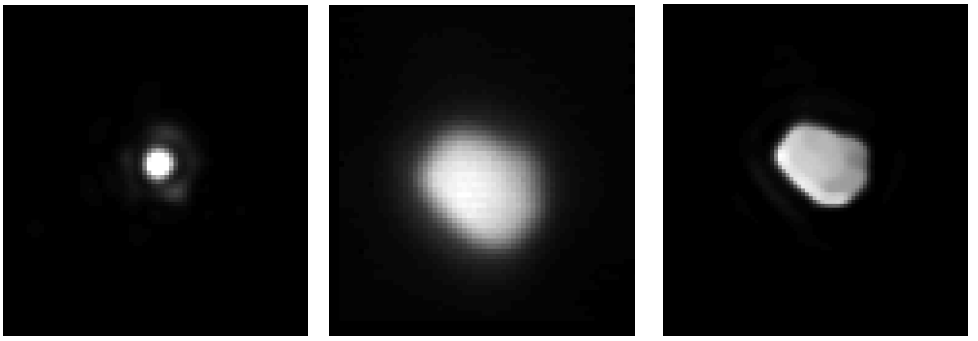

Figure 5.6: PSF of the instrument(left), observed raw image(middle), and deconvolved image(right).

5.4 Range-Doppler radar

With planetary radar observations, spatial resolution of the scale of ten meters is possible (Ostro et al., 2002, Arecibo and Goldstone radars). Unfortunately the power received by the radar is inversely proportional to the fourth power of distance, severely restricting the range of possible targets. In range-Doppler imaging the object is resolved in the range and in the frequency. A nonzero radial velocity of a point on the surface of the object causes a frequency shift in the reflected signal proportional to the velocity. Thus the frequency resolution of a radar image depends on the apparent spin vector of the asteroid. Letting D be the Doppler-shifted frequency and r the range, the projection mapping $p = (x, y, z) \rightarrow (r, D)$ is (Kaasalainen and Lamberg, 2006)

$$\begin{aligned} r &= (x\cos\varphi + y\sin\varphi)\sin\theta + z\cos\theta, \\ D &= \omega\sin\theta\,(x\sin\varphi - y\cos\varphi), \end{aligned} \tag{5.4}$$

where the radar direction in a coordinate system fixed to the asteroid (the z-axis aligned with the rotation axis) is (θ, φ), and the rotation rate of the asteroid is ω.

In this mapping, the range-Doppler radar image brightness L may be written as an integral over the asteroid surface S as

$$L(r, D) = \iint_S h_r\left[r - r(p)\right]\, h_D\left[D - D(p)\right]\, B(p)\, I(p)\, \mathrm{d}S, \tag{5.5}$$

where h_D and h_r are the point-spread functions of the radar system, corresponding to the Doppler-shifted frequency D and the range r, respectively. Here I is the visibility function, which is unity if the point is visible to the radar and zero otherwise. This form is similarly defined for all generalized projections (Kaasalainen and Lamberg, 2006). The mapping $p \rightarrow (r, D)$ is unique, but its inverse is many-to-one, so the inherent information content of a range-Doppler image is considerably smaller than that of an optical image of similar resolution. Thus, while the nominal resolution provided by radar may be unmatched by any other instrument, the drawback of radar imaging is the difficulty of the interpretation of the images. The many-to-one mapping property and the depth vs. width plane makes visual image interpretation tricky; ridges and craters visible in the radar image are not necessarily physical features, but could also be artefacts due to the peculiar way the image is formed. The radar scattering function is given by B, which is usually a simple cosine law

$$B(p) = C\left[\mu(p)\right]^n, \tag{5.6}$$

where μ is the cosine of the angle between the surface normal and the radar direction. The constants C and n measure the surface reflectivity and the specularity of scattering, respectively. The validity

of Eq. (5.6) for modelling the microwave scattering from the asteroid's surface is a rather complex problem. While the cosine law is quite simplified, it should be noted that as the reflected wave is formed in a complicated manner by the surface material whose properties and roughness are usually unknown, fully realistic modelling of the reflected wave is not computationally feasible. However, as in the other disk-resolved cases, most of the information is contained in the boundary contours and is thus independent of the scattering model used.

Assuming the asteroid is modelled as a polyhedron with triangular facets $\mathcal{T}$, the integral (5.5) may calculated separately for each facet, after projecting each triangle T_i as a triangle $\mathcal{P}T_i$ on the range-Doppler plane

$$L(r, D) = \sum_{T_i \in \mathcal{T}} B_i I_i \int_{\mathcal{P}T_i} h_r(r - r')\, h_D(D - D')\, \mathrm{d}r'\, \mathrm{d}D', \tag{5.7}$$

where we have assumed that the visibility I and the scattering law B are constant within a triangle.

Taking the Fourier transform on both sides, applying the convolution theorem, and writing $\mathcal{T}_i(u, v)$ for the sum over the edges of a Fourier transformed triangle as in Sect. 4.3, we obtain

$$\mathcal{L}(u, v) = \sum_{T_i \in \mathcal{T}} B_i\, I_i\, H_r(u)\, H_D(v)\, \mathcal{T}_i(u, v), \tag{5.8}$$

where $H_r(u)$ and $H_D(v)$ are the Fourier transforms of h_r and h_D, respectively.

Radar plots are seldom correctly aligned in some reference frame due to the errors in the centre of mass prediction, so the actual position of a radar image with respect to the two-dimensional projection of the model must be determined during the optimization. The task of image alignment is further complicated by the peculiar asymmetric structure of radar images, especially the bright leading edge, other possible ridges of strong reflectivity, and the fading farthest-range pixels. If the alignment information is unknown, it is usually a good idea to fit the image offsets to a fixed shape first, obtaining better initial positions that can be used in the shape optimization.

As a first example, we consider simulated radar images to demonstrate the feasibility of reconstruction.

In Fig. 5.7 simulated radar images are shown, obtained from the model in Fig. 5.8 (left) with added Gaussian blurring and noise. Our reconstructed model uses 108 shape parameters, and for each radar image, the optimal offset on the plane and the scaling parameter are also determined during the optimization process. The goal here was to produce an intermediate-resolution model rather than a high-resolution one. In principle, the latter could be achieved by adjusting the individual vertices of the model after determining the function series, but usually the noise level sets limits for this.

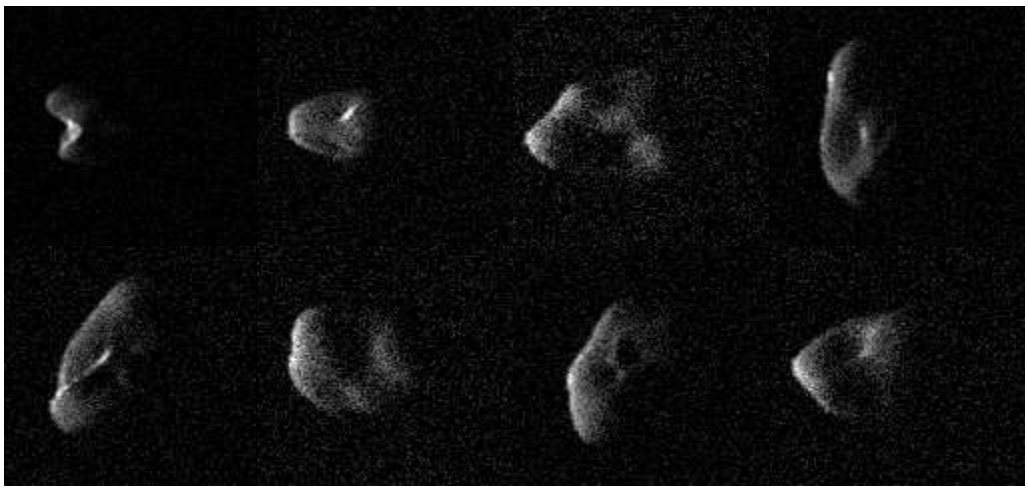

Figure 5.7: Simulated radar images. The range r increases from left to right, and the Doppler frequency D is measured vertically. The nearest boundary $\rho(D)$ is the leftmost boundary of each image.

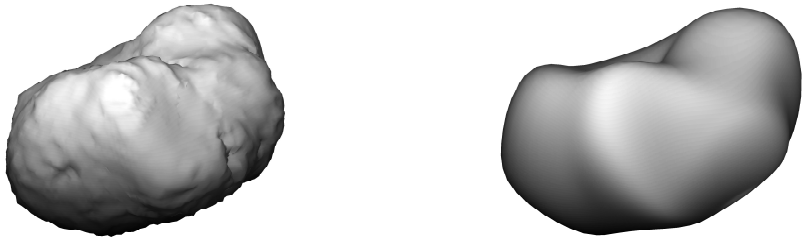

Figure 5.8: Original model (left) and the reconstructed model (right) from simulated radar images(Fig. 5.7).

5.5 Thermal modelling of asteroids

The reconstruction from disk resolved thermal infrared images is conceptually almost identical to reconstruction from the adaptive optics images at optical wavelengths. The only notable difference occurs at the modelling of observed radiation, as the detected thermal flux originates from the heated asteroid surface and subsurface layers, in contrary to the optical case, where the reflected solar radiation dominates. This necessitates the modelling of the thermal conduction occurring in the subsurface layers of the asteroid.

Thermal infrared radiation from an asteroid is a complicated process depending, for example, on heliocentric distance, rotation period and surface properties. There are several models with varying complexity, e.g. Delbo (2004); Mueller (2007). Advanced thermophysical models for asteroids include parameters to model, e.g., the macroscopic surface roughness and multiple reflections. However, from the viewpoint of shape reconstruction, these effects are of lesser importance compared to the overall shape. In the following, we consider two different methods for solving the heat diffusion equation: the finite difference(FD) solution and the FFT method. Calculating the heat flux of an polyhedral model consists of solving the heat diffusion equation numerically for each facet and for each time step. Additional finite difference steps are required

for determining the partial derivatives of heat flux with respect to the shape parameters. For even moderately-sized models, with the shadowing and the diurnal solar radiation variation taken into account, it can be prohibitively expensive computationally.

An elegant alternative approach to the finite difference-method is the Fourier-series method (Bertotti et al., 2003; Nesvorný and Vokrouhlický, 2008) briefly described below in view of our application. As the fast Fourier transform is computationally cheap, the Fourier-series approximation is much faster than the finite-difference method for solving the diffusion equation. The downside is that the approximation originally pertains to moderate heat variations, and the mutual heating of facets must be ignored. However, even in this case the Fourier-series approximation will still provide good initial values for the finite difference method decreasing the computation time.

From the point of view of the inverse problem, the Fourier-series method, though an approximation, is nevertheless quite adequate for describing the observed radiative flux (thermal brightness) on the object's surface. This is because, again, the bulk of the information comes from the boundary of the target (a heated surface patch vs. cold background). Just as in the adaptive optics case, the accuracy of the model of the interior intensity distribution is not crucial.

5.5.1 The heat diffusion equation

Both diurnal and seasonal variations in solar insolation will cause fluctuations in the surface temperature. As the orbital period is considerably longer than the sidereal rotation period, seasonal thermal variations may be ignored. The heat penetration depth into subsurface is characterized by thermal skin depth (with density ρ, heat conductivity K, specific heat capacity c_p and sidereal rotation rate ω):

$$L_T = \sqrt{\frac{K}{\omega \rho c_p}}.$$

The amplitude of temperature variation is attenuated by factor of e for each depth L_T. For typical asteroids, the thermal skin depth varies from millimeters to a few centimeters. As the facets in the polyhedral mesh of the model are usually much larger than the diurnal thermal skin depth, it is reasonable to assume that heat is conducted only in the direction of the facet normal. Hence it is enough to solve the one-dimensional heat diffusion equation with a radiation boundary condition for each facet, with shadowing and mutual heating between facets taken into account.

Assuming that the heat flows only in the direction of the local surface normal, the heat diffusion equation (with temperature T) is given by

$$\rho c_p \frac{\partial T}{\partial t} = K \frac{\partial^2 T}{\partial \xi^2},$$

where the vertical direction ξ in the surface material is aligned with the direction of the surface normal. Ignoring both multiple scattered and reabsorbed thermal radiation, the radiation boundary condition may be written in a simple form

$$K \left(\frac{\partial T}{\partial \xi} \right)_{\xi=0} + \epsilon \sigma T^4_{\xi=0} = (1 - A) F_S(t),$$

where $F_S(t)$ is the solar insolation. As the heat penetration depth is only a few centimeters, there is a depth d after which heat variation is negligible. Thus the second boundary condition follows:

$$K \left(\frac{\partial T}{\partial \xi} \right)_{\xi=-d} = 0.$$

5.5.2 Diurnal cycle and Fourier series

We present here the main points of the Fourier-series thermal approach. We define the insolation factor $\mathrm{ins}(\mu_0, p)$ for a point p on the surface Nesvorný and Vokrouhlický (2008) as

$$\mathrm{ins}(\mu_0, p) = \begin{cases} \mu_0, & p \text{ is illuminated,} \\ 0, & \text{otherwise.} \end{cases}$$

This is obviously a cyclic function of ϕ, the rotation angle of the asteroid around its axis (when the asteroid is effectively stationary during one rotation; i.e., its rotation period is much smaller than the orbital one), so it can be expanded as a Fourier series:

$$\mathrm{ins}(\mu_0, p) = \sum_n d_n \, e^{in\phi}.$$

For a convex body, the function $\mathrm{ins}(\mu_0, p)$ is continuous. If the minimum and maximum limits of ϕ for $\mu_0 \geq 0$ are, respectively, ϕ_{rise} and ϕ_{set} for a point p, we have

$$d_n(p) = \frac{1}{2\pi} \int \mathrm{ins}(\mu_0, p) \, e^{-\imath n\phi} \, d\phi = \frac{1}{2\pi} \int_{\phi_{\mathrm{rise}}(p)}^{\phi_{\mathrm{set}}(p)} \mu_0(p, \phi) \, e^{-\imath n\phi} \, d\phi.$$

The coefficients $d_n(p)$ can be readily computed analytically to any order n.

For a nonconvex body, we check the interval $[\phi_{\mathrm{rise}}, \phi_{\mathrm{set}}]$ for facets rising above the local horizon and blocking the Sun at some ϕ (dividing the interval into N epochs). Then we write the Fourier integral as above to obtain $d_n(p)$, when the integrand is zero between shadow epochs ϕ_{in} and ϕ_{out} (this creates derivatives w.r.t. shape parameters). Since the integration limits ϕ_{in} and ϕ_{out} are approximate, one can just as well compute the integral by taking the FFT of the values of $\mathrm{ins}(\mu_0, p)$ of 2^M equidistant epochs distributed inside $[0, 2\pi]$; this gives the Fourier coefficients up to order 2^{M-1}. The derivatives of d_n w.r.t. parameters can also be computed simply by taking the FFT of the derivatives of $\mathrm{ins}(\mu_0, p)$. In fact, one can use FFT for convex bodies as well for an approximation. Now $\mathrm{ins}(\mu_0, p)$ is discontinuous for some p, so the Fourier representation is more approximative than in the convex case.

5.5.3 FFT solution to the heat diffusion equation

The heat diffusion equation with suitable boundary conditions can be solved analytically by assuming that the temperature variation ΔT is small compared to the mean temperature T_0. Then we can linearize equations and solve for ΔT as a Fourier series (Bertotti et al., 2003; Nesvorný and Vokrouhlický, 2008). We can write $F_S(t) = F_0 \, \mathrm{ins}(\mu_0(t), p)$, where F_0 is the solar flux at the asteroid. We define damping factors Ψ_n and phase lags $\Delta\phi_n$ by

$$\Psi_n = (1 + 2\Theta_n + 2\Theta_n^2)^{-\frac{1}{2}}, \quad \Delta\phi_n = \mathrm{sgn}(n) \arctan \frac{\Theta_n}{\Theta_n + 1}, \tag{5.9}$$

where

$$\Theta_n = \frac{\sqrt{\rho c_p}}{4\varepsilon\sigma T_0^3} \sqrt{\frac{1}{2}|n| \, K \, \omega}, \quad T_0^4 = (1 - A) F_0 d_0 / \varepsilon\sigma,$$

and ω is the rotation rate of the asteroid, ε the material emissivity at thermal wavelengths, A the albedo (lightness, $0 \leq A \leq 1$, of the surface material), and σ is the Stefan-Boltzmann constant. Then the radiated IR flux at a point p_i (the centroid of facet i) per surface area is

$$B_i = \varepsilon\sigma T(t)^4|_{\xi=0} \simeq (1 - A) F_0 \sum_n \Psi_n \, d_n(p_i, t) \, e^{i[n\omega(t - t_0) - \Delta\phi_n]}. \tag{5.10}$$

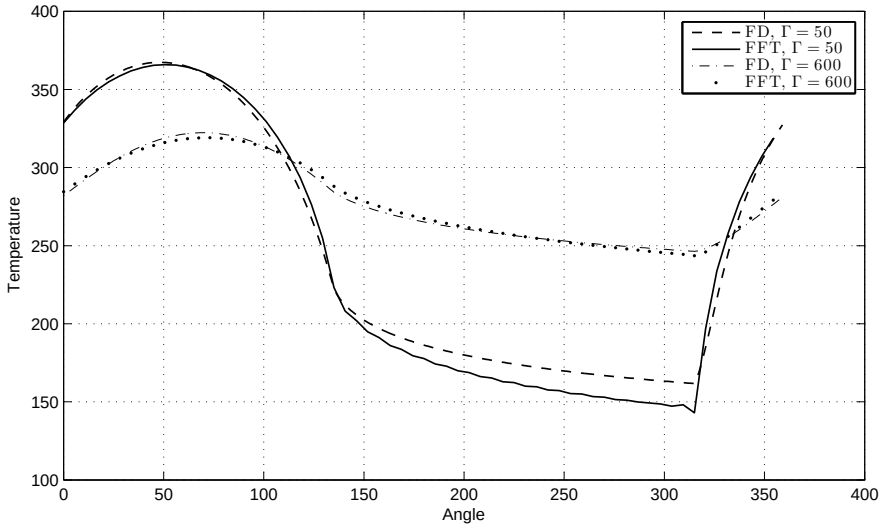

Figure 5.9: Comparison of two solutions of the diffusion equation for two different values of thermal inertia. Vertical axis is the surface temperature in Kelvins and horizontal axis is the angle between the surface normal and the direction of the sun.

The assumption $\Delta T/T \ll 1$ does not always hold. This is dependent on the thermal inertia Γ, which is defined as

$$\Gamma = \sqrt{K\rho c_p}.$$

Thermal inertia measures how resistant the surface is to diurnal temperature changes; an object with a high thermal inertia has smaller diurnal temperature variations than an object with relatively small thermal inertia. It follows that for objects of low thermal inertia $\Delta T/T \ll 1$ no longer necessarily holds, and the FFT solution deviates from the numerical finite-difference solution of the diffusion equation (Delbo, 2004). This is illustrated in Fig. 5.9. However, in our simulations this discrepancy between the solutions has an indiscernible effect on the final shape solution. The shapes of the thermal curves are essentially same for the two methods, and the largest temperature differences do not matter in the inversion. Even if the detail present in many radar images is unattainable by the thermal infrared observations, a thermal map of an asteroid surface is enough for shape reconstruction, as we demonstrate here.

To generate the simulated data, we considered a hypothetical asteroid at the heliocentric distance 1.5 AU, with a thermal inertia of 100 $Jm^{-2}Ks^{-\frac{1}{2}}$ and the albedo 0.1. The pixel size of the instrument is assumed to be 10 milliarcseconds which, taking into account the distance of the target from the Earth, corresponds to approximately 10 kilometers per pixel. The noisy plane-of-sky projections of observed thermal flux of the model asteroid are illustrated in Fig. 5.10. The actual data are the samples of the Fourier transforms of these projections. To avoid 'inverse crime', the data were generated with the finite difference method, and the FFT method was used in the inversion. The original model and the reconstructed shape parametrized by 108 parameters are shown in Fig. 5.11.

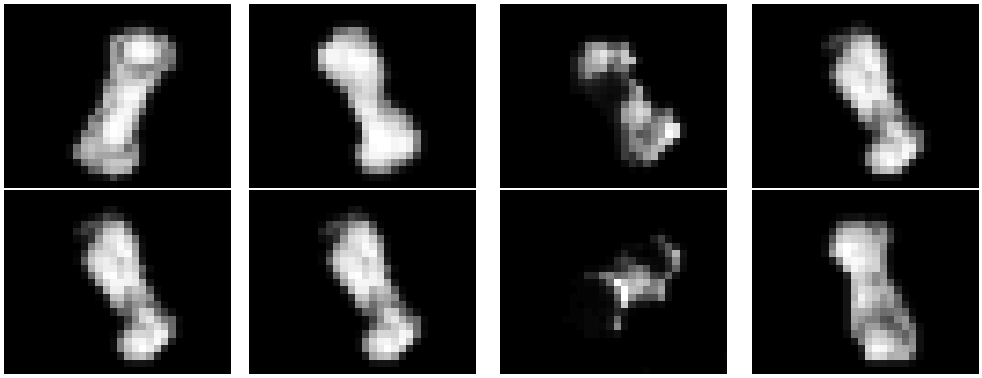

Figure 5.10: Simulated thermal infrared flux images of an asteroid.

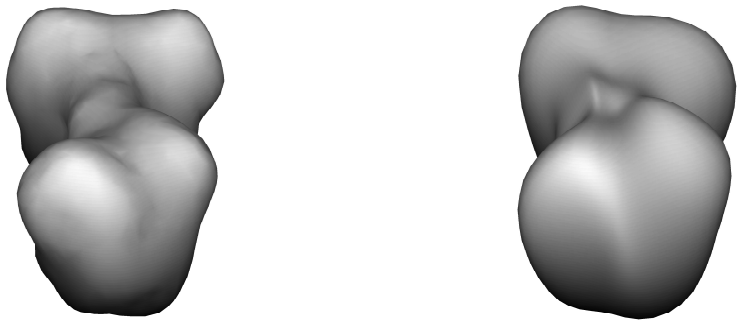

Figure 5.11: Original model (left) and the shape reconstructed from the thermal images shown in the previous figure.

5.6 Interferometry

The interferometric imaging method differs radically from a typical telescope; instead of observing the sky brightness directly, the interferometer samples the Fourier transform of sky brightness. Each antenna pair of the interferometric array determines one sample on the Fourier plane. The maximum separation between antennas determines the maximum attainable resolution.

The interferometer currently most relevant to asteroid shape studies is the Atacama Large Millimeter Array (ALMA) in the Chilean desert. In its full configuration, the interferometer will be capable of observing at the resolution of a few milliarcseconds at the wavelength of 0.3 mm, corresponding to the separation of 16 km between antennas.

Given the brightness distribution $I(\xi, \eta)$ on the plane-of-sky, the visibility function is defined as the integral

$$V(u, v) = \iint I(\xi, \eta)\, e^{-2\pi\imath(u\xi+v\eta)}\, \mathrm{d}\xi\, \mathrm{d}\eta, \tag{5.11}$$

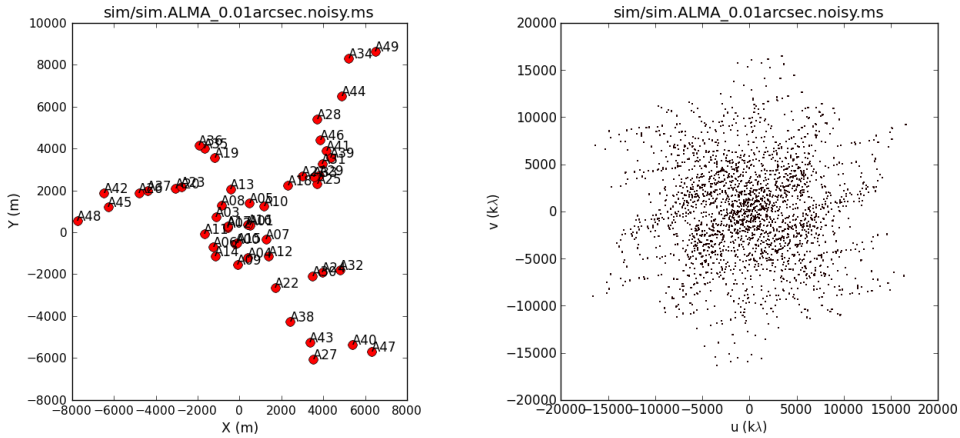

Figure 5.12: The antenna locations of ALMA (left) and corresponding uv-plane visibilities (right). Images were generated with the CASA software package.

which is a two-dimensional Fourier transform of the brightness distribution. Each antenna pair, corresponding to the projected baseline on the plane-of-sky, samples the visibility function. When the visibility function is sampled on a sufficiently dense set, the Fourier transform can be inverted to obtain the brightness distribution $I(\xi, \eta)$. Since the function $V(u, v)$ is measured only at a finite number of points, the observed visibility function is

$$\tilde{V}(u, v) = F(u, v)\, V(u, v), \tag{5.12}$$

where $F(u, v)$ is a sampling function corresponding to the sampled points on the (u, v)-plane. Thus the obtained brightness distribution is actually

$$\tilde{I}(\xi, \eta) = f(\xi, \eta) \star I(\xi, \eta), \tag{5.13}$$

i.e., a convolution of the true brightness distribution with the inverse Fourier transform $f(\xi, \eta)$ of the sampling function. Deducing the true brightness distribution I from the partially measured brightness $\tilde{I}$ is an inverse problem and there are several iterative algorithms to infer I from $\tilde{I}$, see, e.g. Labeyrie et al. (2006).

While the images obtained from the interferometer are informative, the great advantage with ADAM is that the algorithm works directly with the values of the visibility function obtained from the instrument. This approach has several distinct advantages:

- Sparse data may be used (e.g. interferometry with a few baselines)
- The distribution of antennas does not cause systematic artefacts, since the Fourier transform is not inverted
- Possible artefacts caused by the deconvolution process are avoided
- The dependence between different observations is taken automatically into account

To obtain the luminosity values for the model surface (i.e. the brightness factor B_i for each facet) in the infrared regime of ALMA, we can use the Fourier-series approximation of Nesvorný and Vokrouhlický (2008) as discussed in the section 5.5. The fast analytical computations are then

efficient in the optimization. A simple thermophysical model is sufficient for shape reconstruction, as the most relevant information is contained in the boundary data, which are quite robust with respect to our thermal model. This is in contrast to the disk-integrated thermal data that are more sensitive to both the surface properties and the thermal model.

For thermal infrared imaging, ALMA facilitates asteroid observations at resolution levels previously attained only by range-Doppler radar. To explore the possibilities of ALMA for shape modelling, we use the Common Astronomy Software Applications (CASA) package developed by National Radio Astronomical Observatory (NRAO) to simulate observations.

Consider a hypothetical asteroid with geocentric and heliocentric distances of 1.5 and 1 AU, respectively. The thermal flux is observed at the 350 GHz band, a frequency located in an atmospheric window. There are 11 observation runs, each observation lasting 50 s with 10-second integration time. We choose an antenna configuration providing approximate resolution of 10 mas, a resolution which is well within the capabilities of ALMA. The antenna configuration and the corresponding uv-plane sampling pattern are shown in Fig. 5.12. The uncorrupted plane-of-sky images, with a resolution of five milliarcseconds, are displayed in the column on the left in Fig. 5.13. We use the CASA software to add realistic atmospheric noise to the observations. The resulting dirty images, which are obtained by assuming that the unsampled frequencies are zero, are shown in the middle column. These images are provided for illustration purposes only, since ADAM uses the *uv*-plane samples directly.

To test the ADAM reconstruction method, we use a low-resolution octantoid representation with 75 shape parameters. We also fit a scaling term, common to all observations. Usually it is a good idea to use scaling specific to each observation, but in this case we know that all the simulated observations are done in similar conditions, so the common scaling term is justified. The reconstructed shape is displayed in the right column in Fig. 5.13, with the same observation geometries as for the model images. The small-scale detail is lost, which is to be expected because of the added atmospheric noise and coarse instrument resolution. However, the biloped shape is well recovered despite the noisy data (note that we used ALMA data only). The computation time for this reconstruction was a few minutes. For real observations, complementary data are often provided by other observation methods e.g. disk-integrated photometric data are almost always available.

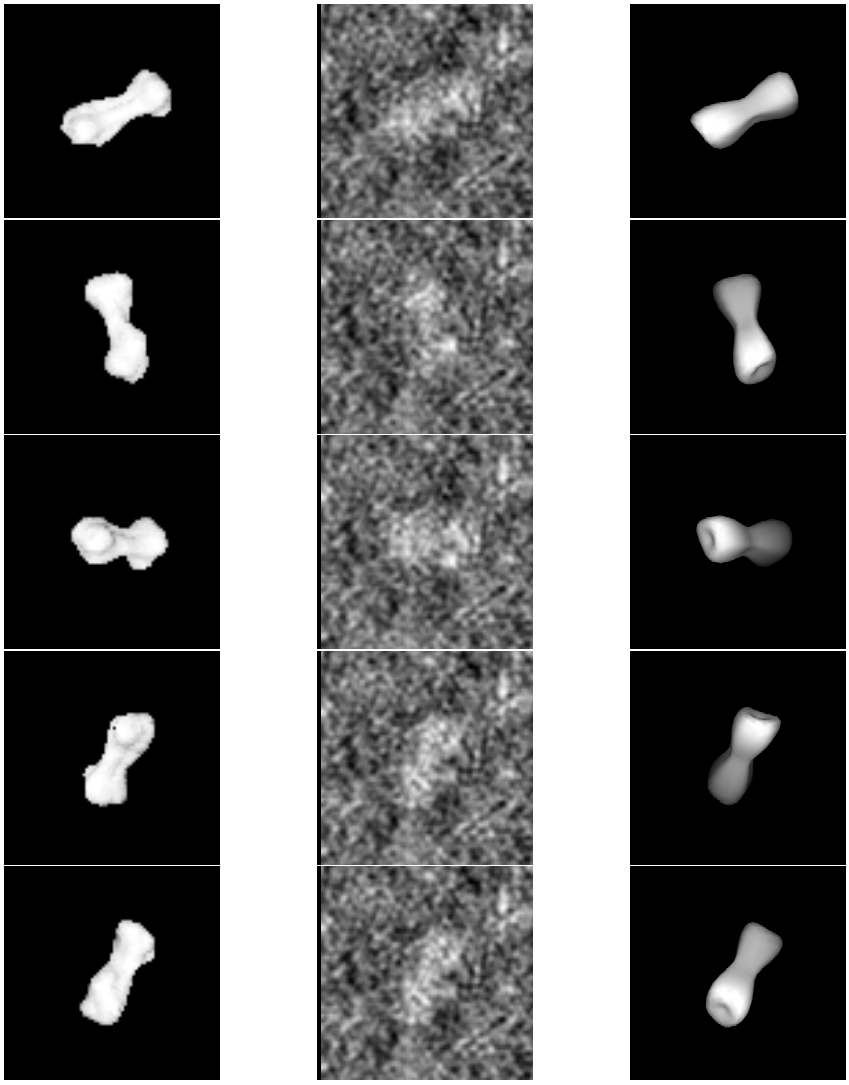

Figure 5.13: Simulated, uncorrupted images with 5 mas pixel size (left column), observed dirty images generated with CASA (middle) and the reconstructed low-resolution shape model (right). Note that the middle-column images are not used in inversion; we use the direct FT data instead. The images are what would be seen if the raw data were deconvolved for viewing purposes as is usually done for ALMA targets. The test shape model is from Ostro et al. (2000).

6 Asteroid shape reconstruction from astronomical observations

In this final chapter, we demonstrate the applicability of reconstruction methods developed in the previous chapters. We reconstruct shape models for asteroids observed with range-Doppler radar, adaptive optics, disk-integrated photometry and thermal infrared interferometry.

6.1 Shape of Asteroid 41 Daphne from adaptive optics images

We consider the large main-belt asteroid 41 Daphne. We use 19 near-infrared adaptive optics images obtained with the Very Large Telescope array at ESO and with the Keck II telescope. The pixel size is approximately 0.01 arcseconds. This corresponds to $7-12$ kilometers per pixel, as the geocentric distance varies between images. Each image is transformed to the frequency plane and sampled on a rectangular grid consisting of 8191 points. In addition, we include 37 lightcurves, which mostly refine the spin state solution. Interestingly enough, they have no discernible effect on the actual shape solution as the available AO images seem to constrain the shape adequately. The solution is similar to the one in Kaasalainen (2011) obtained with image boundaries. The adequacy of AO data can also be seen in the curve in Kaasalainen (2011) depicting the lightcurve fit as the weight of AO data is increased: the lightcurve fit does not decrease much along the curve.

We use both octantoids and subdivision surfaces for reconstruction. Our octantoid model consists of a triangular mesh with 1568 facets, with vertex locations defined by 243 shape parameters. The highest degree of spherical harmonics in the reconstruction is nine. The subdivision model uses 306 shape parameters. In addition to the shape parameters and the direction of the rotation axis, we also determined optimal offset parameters for each image, since the object's location on the image plane is unknown. The light-scattering model used in the reconstruction is not important since most of the information is on the boundaries. We chose the standard combination of the Lommel-Seeliger and Lambert laws (Kaasalainen et al., 2001):

$$B_i = C\,\mu_0^{(i)}\left(\frac{1}{\mu^{(i)}+\mu_0^{(i)}}+0.1\right),$$

where C is a free constant for each image for adjusting the intensity level of the model to match that of the data. More complicated scattering models such as Hapke can be used, but this has no effect on the result as the interiors of the object are not reliable in the images in any case. The reconstructed models are depicted in the Fig. 6.1. Both octantoid and subdivision models are very similar, indicating that the prominent features present in the models are indeed due to the data and not artifacts caused by the shape representation. In Fig. 6.2 we show some of the adaptive optics images and the projections of the reconstructed models. It is interesting to note that the

Table 6.1: Size and spin parameters of the sample model variations of asteroid Daphne. D is the volume-equivalent diameter. The convex model is from Kaasalainen et al. (2002b).

	Subd.	Oct.	Convex+AO
β	-32	-30	-32
λ	202	201	198
x(km)	233	233	236
y(km)	193	194	191
z(km)	166	156	164
D(km)	186	183	187

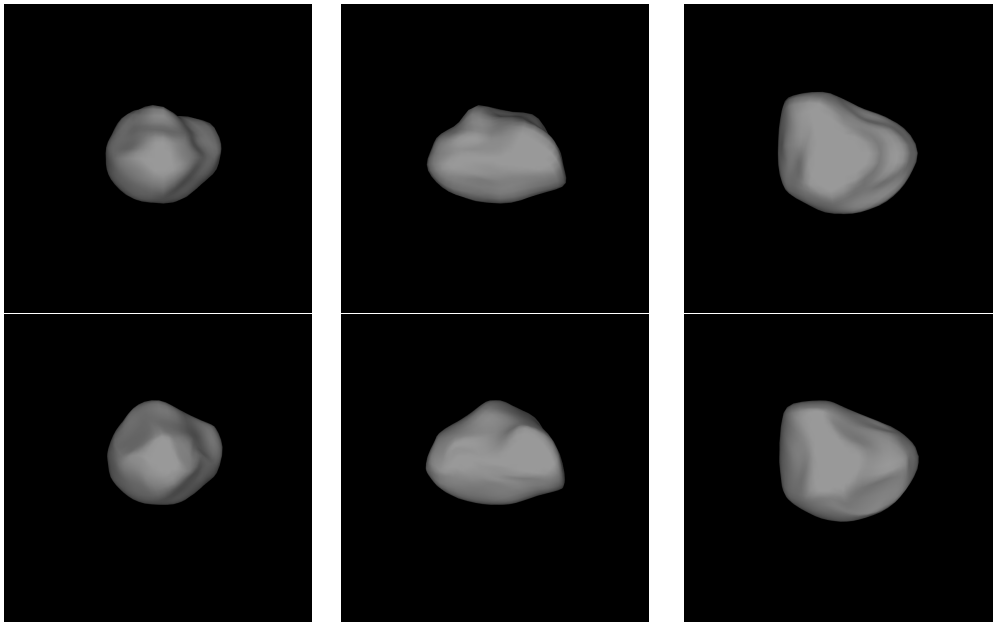

Figure 6.1: Reconstructed octantoid and subdivision models. Viewing directions are from positive x-,y-, and z-axes.

non-convex details visible in the AO images (Fig. 6.2) are also apparent in the reconstructed model, so the result could indeed be seen as a form of image processing as well.

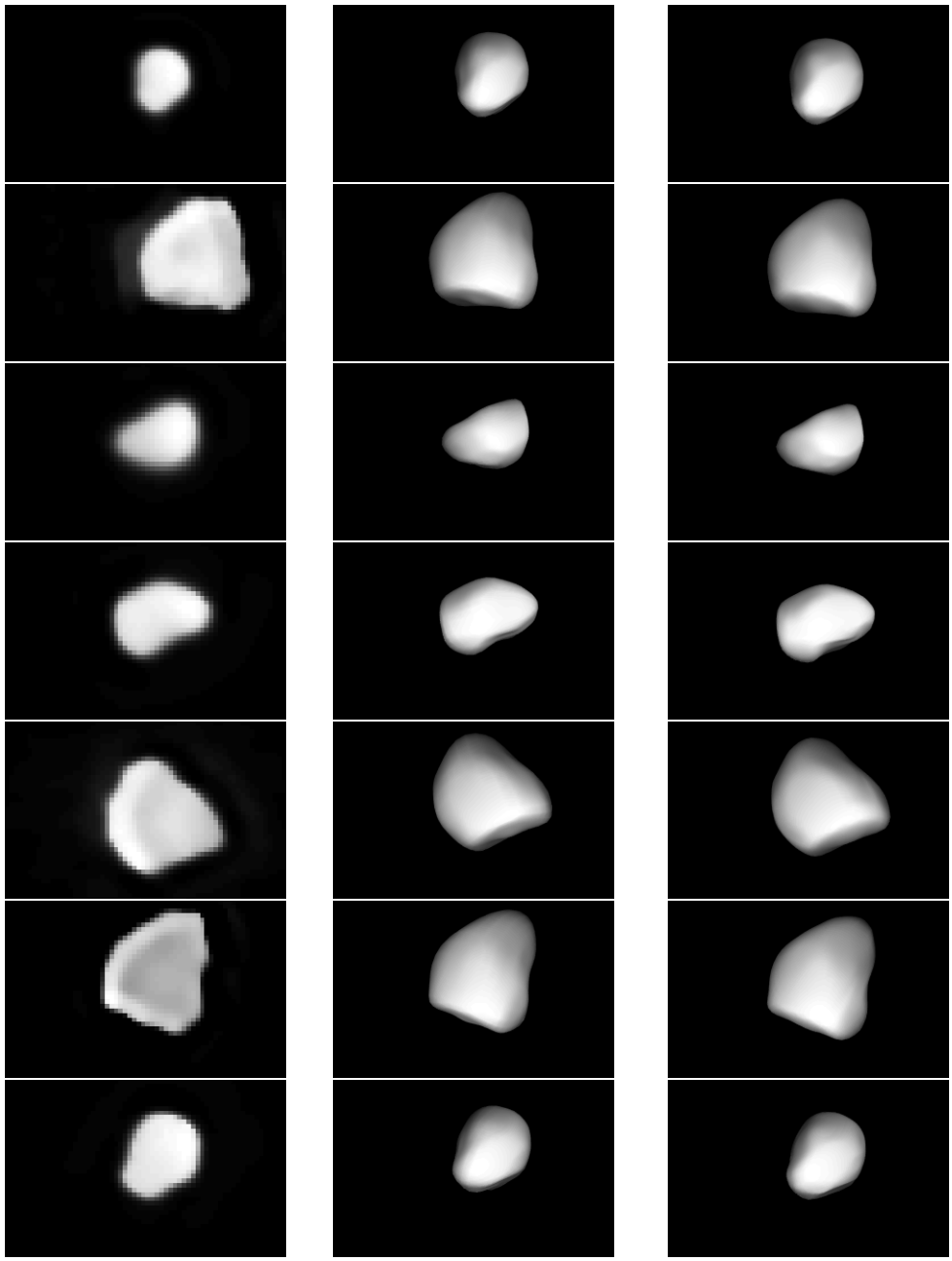

Figure 6.2: Examples of the adaptive optics images(left column) of the asteroid Daphne, and the corresponding model (middle:octantoid, right:subdivision) projections.

6.2 Range-Doppler radar imaging of the asteroid 2000 ET70

To demonstrate the reconstruction method, we make a ADAM model of the near-Earth asteroid 2000 ET_{70}. Our goal is to get a first look at an initial model. The asteroid was observed during February 2012 at Arecibo and Goldstone observatories using 2380 and 8560 MHz range-Doppler radars (Naidu et al., 2013). The images obtained from Arecibo have a resolution of 15 m in range and 0.075 Hz in frequency. Goldstone images have a somewhat lower resolution, 15 to 75 m and 1 Hz, respectively. Our goal is to produce medium-scale detail in the reconstructed shape, so a typical model choice is an octantoid with $l_{\max} \sim 10$ and around 1500 facets. Our example is "first-result oriented" on purpose, so we assume no information about the instrument-specific distortions, or more importantly, knowledge about the point-spread functions determined by the instrument and the processing routines of the radar signal. Thus the point-spread function used in the shape reconstruction is simply the two-dimensional delta function.

For each data image, we fit, in addition to the shape parameters, the offset with respect to the model centre of mass and the reflectivity term in Eq. (5.6). The reconstructed middle-resolution shape is shown in Fig. 6.3 and the model fit to the data in Fig. 6.4. The shape model fits the boundary contours of the radar images satisfactorily, but there are some differences in the interior details. This is a consequence of the parametrization and facet size chosen for reconstruction. The interior could be reproduced in greater detail by choosing a different parametrization, for example locally adaptive subdivision surfaces, or by refining the positions of individual vertices. The model dimensions, shape features, and spin parameters agree with those published by Naidu et al. (2013) (the spin parameters are identical except for a 2° difference in the pole latitude, well within error limits).

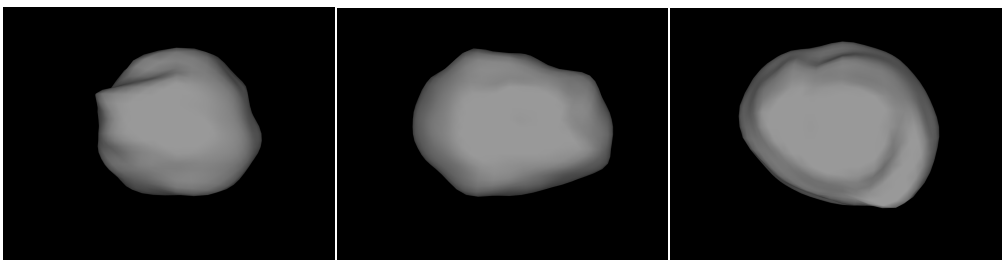

Figure 6.3: Mid-resolution shape model of the asteroid 2000 ET_{70} reconstructed from radar images. Viewing directions are from the positive x, y, and z axes, respectively.

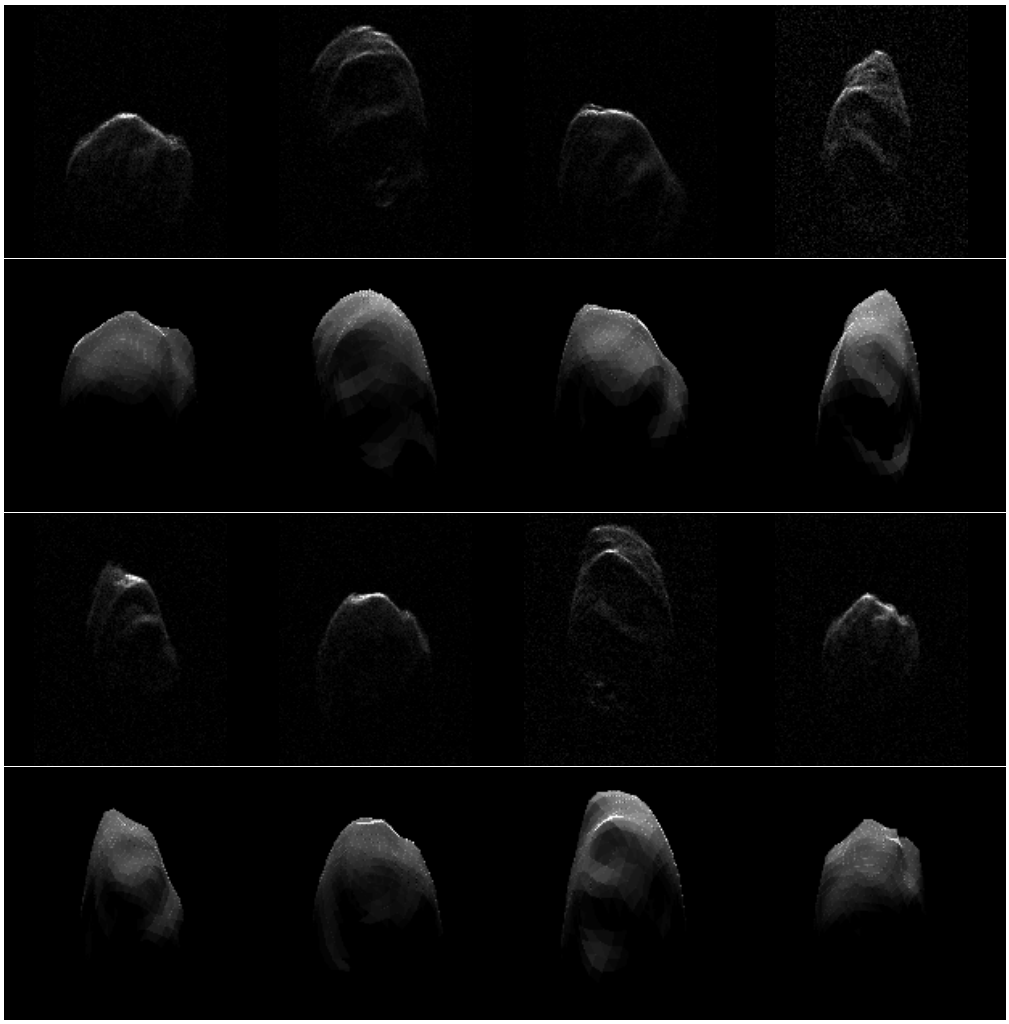

Figure 6.4: Examples of range-Doppler images of the asteroid 2000 ET_{70} from Arecibo Observatory (rows 1 and 3) and corresponding projections of the mid-resolution model (rows 2 and 4). The contrast scale of the model image is somewhat modified to reveal inner image features.

6.3 Shape of asteroid 3 Juno from thermal infrared interferometry

We use recently released Atacama Large Millimeter Array (ALMA) science verification data and several lightcurves to model the 3-D shape and spin axis direction of the large main belt asteroid Juno. Moreover, to examine the reliability of the thermal model, we also reconstruct an independent shape model using adaptive optics images from VLT and Keck.

Juno was observed with ALMA on 2014 Oct 19 using between 27 and 33 antennas, providing projected baselines between 26 m and 13 km. At the observed frequencies of 224, 226, 240, and 242 GHz, this corresponds to angular resolutions as high as 0.021″, or about 30 km projected at the distance of Juno. A total of 10 different epochs spread over 4.4 hours, corresponding to about 60% of its rotation period, were acquired, each with several hundreds of thousands points in the visibility function plane. As stated by ALMA Partnership et al. (2015), each epoch on Juno lasted for 18 min, during which Juno rotated 15°. The smearing effect is however limited to about 21 mas.

As described in the previous chapter, the ALMA data are samples of the Fourier transform (FT) of sky brightness. Unlike most other ALMA users, we can directly use the raw FT data for reconstruction. The "clean" ALMA images obtained by various deconvolution and self-calibration processes inevitably lose and distort some of the original information.

In the Fig. 6.5 typical "dirty" images are depicted. Each image is obtained from the visibility data by setting the unobserved frequencies to zero and inverting the Fourier transform. According to the section 5.6, they correspond to the plane-of-sky projection convolved with the inverse Fourier transform of the frequency plane sampling pattern.

In 2001 and 2010, Juno was observed with the first generation AO cameras NIRC2 (van Dam et al., 2004; Wizinowich et al., 2000) on the W. M. Keck II telescope and NACO (Lenzen et al., 2003; Rousset et al., 2003) on the ESO VLT, respectively. The angular resolution of these data is of 0.045 and 0.055″, respectively.

We also present here data we obtained during the science verification phase of the recently commissioned second-generation SPHERE AO system, mounted at the VLT (Beuzit et al., 2008). SPHERE is an instrument designed for exoplanet detection and characterization by high-angular and high-contrast imaging and spectro-imaging. The AO module (Fusco et al., 2006) was therefore designed to provide extremely high fidelity correction, but limited to very bright target (R ~ 11). We used the classical imaging mode of SPHERE (IRDIS, Dohlen et al., 2008) to image the apparent disk of Juno. The different data sets and observation times are summarized in Table 6.2.

Obs. time	Instrument	Δ	Phase	Asp.	Fig.
2001-12-26T15	NIRC2	1.59	-120	−-30	6.6a
2010-12-13T07	NACO	2.41	-23	−-14	6.6b
2010-12-13T08	NACO	2.41	-96	−-14	6.6c
2014-12-09T07	SPHERE	1.52	-158	−-36	6.6d
2015-01-30T06	SPHERE	1.33	-125	−-41	6.6e
2015-01-30T08	SPHERE	1.33	90	−-41	6.6f
2015-01-31T05	SPHERE	1.34	138	−-41	6.6g

Table 6.2: Adaptive optics observations used for the reconstruction. Distance in AU is given by Δ, and the rotation phase and the aspect angle (wrt. the asteroid's equator) are based on the adopted full-data model.

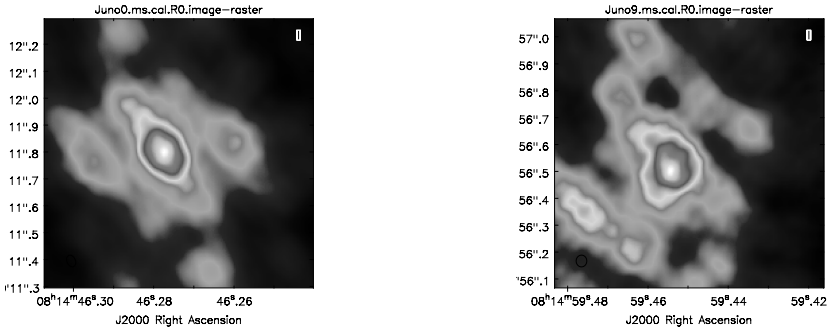

Figure 6.5: Dirty images obtained by directly inverting the visibility data. Images created with CASA (http://casa.nrao.edu).

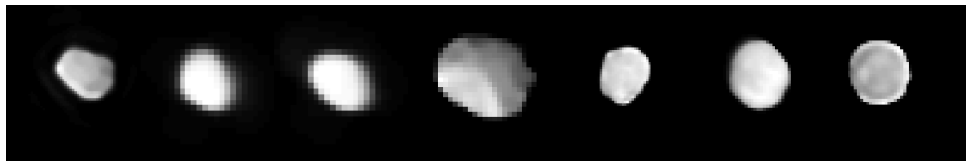

(a) **(b)** **(c)** **(d)** **(e)** **(f)** **(g)**

Figure 6.6: Adaptive optics images used for reconstruction. See table 6.2 for description.

We used the thermal model described in the previous chapter to construct a shape model of the asteroid Juno. The views corresponding to the deconvolved data images are shown in the Fig. 6.7, and the shape model in Fig. 6.8. It is interesting to compare the model obtained from thermal data and lightcurves to the independent shape model reconstructed from adaptive optics and lightcurves (Fig. 6.8, bottom row). It is evident that both models look similar, and although the adaptive optics model has more detail, it does not fit the thermal data better than the model reconstructed from the thermal data. This lends credibility to the thermal reconstruction procedure.

Finally, we examine the effect of self-calibration on the quality of shape reconstruction. During self-calibration, the antenna phase errors causing deteriorated image quality are corrected iteratively, alternating between the frequency and the image domain (ALMA Partnership et al., 2015). In Fig. 6.9 we show the shape model reconstructed from the self-calibrated, deconvolved images instead of the raw data. Comparing this to the model in Fig. 6.8, it is evident that, at least for this level of resolution, self-calibration does not reveal any additional detail. The best way to facilitate full high resolution in shape reconstruction from future full-baseline ALMA data is to leave the antenna gains to be free parameters (Hezaveh et al., 2013), so that the optimization of the shape, spin, and the antenna parameters is done simultaneously. This prevents the introduction of potentially spurious information into the shape solution.

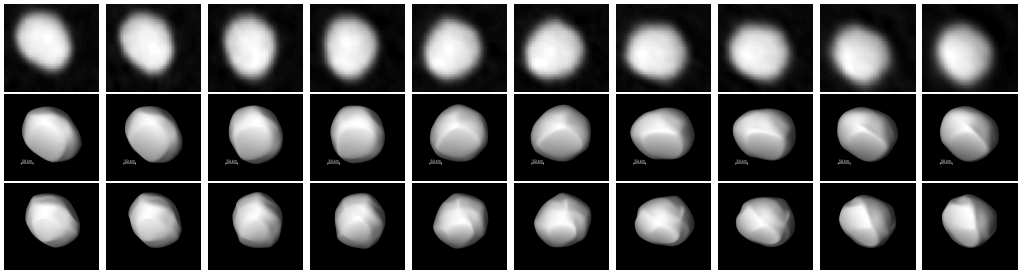

Figure 6.7: Deconvolved ALMA images (top), thermal model with the corresponding view geometries (middle), and the adaptive optics model (bottom).

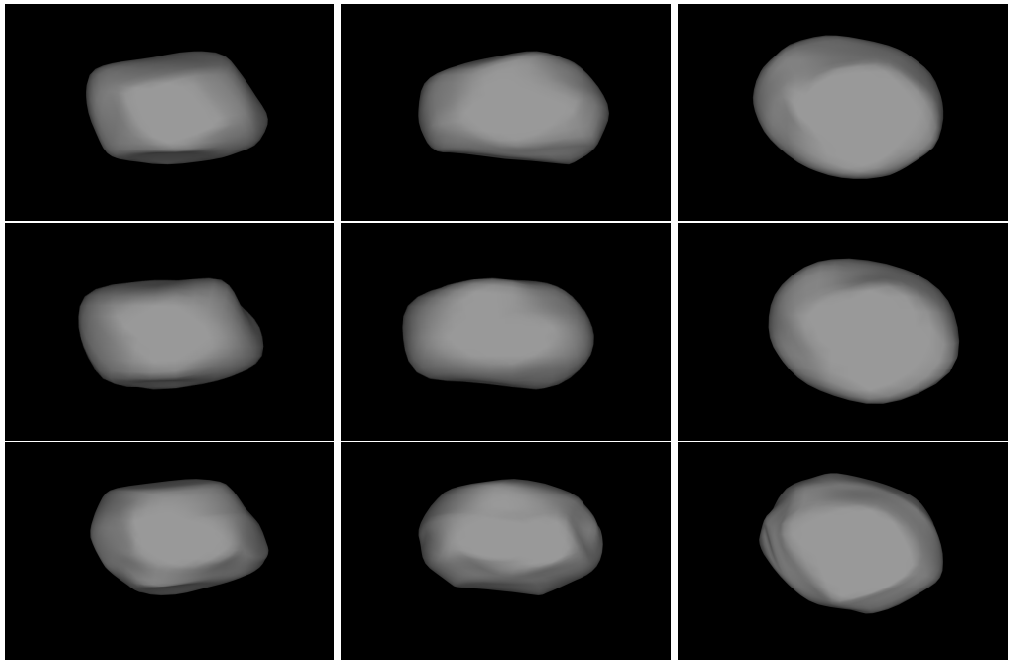

Figure 6.8: Shape models of Juno reconstructed from ALMA data (top:subdivision, middle:octantoid), and from adaptive optics images (bottom). Similarity of models is evident.

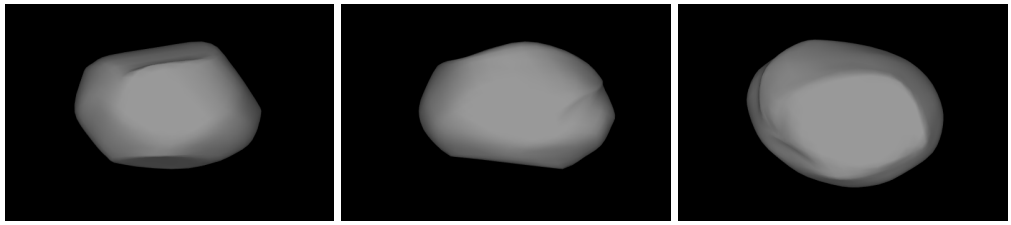

Figure 6.9: The model reconstructed from the deconvolved ALMA images and photometry.

7 Conclusions

In this thesis, we have developed methods for recovering the shape of an object from generalized projections and have successfully applied these results to the shape reconstruction of asteroids, and we have published a general shape reconstruction method that can combine any observational data obtained from different instruments into a coherent shape solution. In addition to shape modeling, this procedure is also useful for observation planning and what-if analysis: we can determine instruments and observational geometries that are likely to reveal additional information on the asteroid. This allows us avoid to redundant and overlapping observations: for example, the asteroid Juno was observed with both SPHERE and ALMA instruments, resulting in data sets with almost identical observational geometries. While the overlapping data sets proved to be useful for evaluating the ALMA-based shape reconstruction method, it should be noted that the northern hemisphere of Juno still remains relatively unobserved.

While the recovery of the object's shape is important, equal importance should be given to the reliability estimation of reconstruction. Most approaches suffer from problems relating to the uniqueness of solution. As we demonstrated in the case of lightcurves, it is easy to discover features that are not supported by the data. The problem is even more subtle when the projection mapping is many-to-one as in, e.g., HST/FGS or the range-Doppler radar. In these cases, reliable shape reconstruction requires either data with good coverage and extensive observation geometries or additional data with a different projection mapping to resolve uncertainties. In this thesis we have advocated the use of different shape representations to gauge the variability of shapes fitting the data. However, this is only the first step. For instance, realistic scattering cannot be fully modeled with the scattering laws currently in use; thus only the features that remain relatively invariant as the scattering model is varied should be considered relevant.

A related problem is the use of heavily processed data. While processed images are useful for visual inspection, they are mostly hindrances when used for shape reconstruction as they are potentially biased by prior assumptions. An example of this is the self-calibration procedure for interferometric data: after the calibration step, remaining antenna phase errors are corrected by an iterative procedure directed by visual cues. Same problems pertain to other disk-resolved data: the adaptive optics images are corrupted by atmospheric disturbances and recovering the projection contour by deconvolution and boundary extraction can introduce spurious information into solution. Often it is impossible to determine from a single frame whether a non-convexity in the image boundary is due to shading effects or if there is an actual concavity on the asteroid's surface. With the boundary contour fitting the choice that removes fuzzy-pixel information must be made beforehand; the ADAM method allows relegating the choice to the optimization routine. The contrast is evident in the case of Juno: in the deconvoluted adaptive optics images there is an obvious protrusion visible, but according to the ADAM-constructed model, it is caused mostly by a sloping surface instead of a concavity. This is why we have advocated the use of raw data in shape reconstruction; the calibration and correction terms should be determined simultaneously with shape parameters to avoid introducing systematic errors.

In the wake of new instruments, the importance of multi-data inversion will increase in the future. The competition for telescope time between potential targets will result in observations with restricted observation geometries, requiring a combination of a widely different data sets if a detailed model is desired. However, the methods alone are not sufficient if there are no data available. The importance of data sharing cannot be exaggerated. While the DAMIT database and the Keck and ESO data archives are encouraging examples, there are still important instruments whose observations are not made available to the public. Too often the data are simply forgotten after the publication of results in a scientific article, instead of making them available to the scientific community to whom the data could be useful. With the multi-data inversion routine and the maximum compatibility estimate procedure, even data of lesser quality are important when combined with new observations. To promote openness, we have published a software package implementing all the methods described in this thesis, and we are planning to update and expand it in the future.

Appendix

Coordinate frames and rotations

Three different coordinates systems are used in ADAM: the asteroid-centric coordinate frame (object frame) with coordinate axes fixed to the asteroid, the asteroid-centric inertial frame (world frame), and the camera frame. The object and world frames are independent of data sources, and the camera frame corresponds to the device-dependent part and is determined by the instrument orientation geometry. In this section, we consider these frames and transformations between them in detail.

Orientation of the asteroid in the world frame is determined by three angles (and time t): ecliptic latitude $\beta \in [0, \pi]$, ecliptic longitude $\lambda \in [0, 2\pi]$, and the rotation rate w. The transformation matrix from the object frame to the world frame is

$$R_z(\lambda)R_y(\beta)R_z(w \cdot t),$$

where

$$R_z(\theta) = \begin{pmatrix} \cos\theta & -\sin\theta & 0 \\ \sin\theta & \cos\theta & 0 \\ 0 & 0 & 1 \end{pmatrix} \text{ and } R_y(\theta) = \begin{pmatrix} \cos\theta & 0 & \sin\theta \\ 0 & 1 & 0 \\ -\sin\theta & 0 & \cos\theta \end{pmatrix}$$

are the standard rotation matrices with respect to z- and y-axes, respectively.

The camera frame is determined by the observation method and by the coordinate system used. Conversion from the world frame to the camera frame is determined by two unit vectors: camera direction $\mathbf{E}$ as seen from the world frame (camera look direction is $-\mathbf{E}$), and camera up direction $\mathbf{V}$ which determines how camera is rotated with respect to the world frame. This is useful is in the case observations are in the equatorial coordinates. The camera frame conversion matrix R_C maps the observable quantities to the first two coordinates, and the third coordinate axis is chosen to complete the coordinate system.

In the case of adaptive optics and other optical images, we choose a new coordinate system with axes X, Y, and Z, where

$$\begin{aligned} Z &= -\mathbf{E} \\ X &= \frac{\mathbf{V} \times Z}{\|\mathbf{V} \times Z\|} \\ Y &= Z \times X. \end{aligned}$$

The coordinate system for the range-Doppler radar is slightly more complicated, since the observables are the line-of-sight velocity, which corresponds to the Doppler shift reflected signal,

and the range between the radar and the object. Again, we choose a new coordinate system with axes X, Y and Z

$$\begin{aligned} X &= \mathbf{E} \\ Y &= \frac{\mathbf{E} \times \mathbf{w}}{\|\mathbf{E} \times \mathbf{w}\|} \\ Z &= X \times Y, \end{aligned}$$

where $\mathbf{w}$ the angular velocity vector of the asteroid in the world frame. To convert the coordinates to the actual quantities observed by the range-Doppler radar, the first coordinate should by multiplied by $-\frac{2}{c}$, which converts the relative distance from the plane determined by the $\mathbf{E}$ to the relative signal delay between the plane and a point on a surface. The second coordinate multiplied with $\frac{2f_0}{c}|\mathbf{E} \times \mathbf{w}|$ is the (non-relativistic) frequency shift due to the Doppler effect. Here c is the speed of light and f_0 is the frequency of the radar signal. In both cases, the conversion matrix R_C from the world frame to the camera frame is

$$R_C = \begin{pmatrix} X \\ Y \\ Z \end{pmatrix}.$$

Thus the conversion matrix from the object frame to the two-dimensional image plane is

$$P \cdot R_C \cdot R_z(\lambda) \cdot R_y(\beta) \cdot R_z(w \cdot t),$$

where P is the projection matrix discarding the third coordinate.

Reconstruction from boundary contours

A straightforward way of recovering shape from pixel fields is using only the boundary contour of the image. Moreover, the boundary contour is also independent of chosen scattering law, making the inversion process robust. Shape reconstruction from boundary contours has been used before in, e.g., KOALA (Carry et al., 2012). The algorithm described here is an extension to more general, non-starlike shapes.

A procedure for constructing the outer shadow and limb boundary of the projection of a polyhedron was outlined in Kaasalainen (2011). However, for a general non-starlike object, the construction is too time-consuming and complex to be used in an inversion process. Instead, we construct an approximate boundary $\partial\mathcal{B}(\omega_0, \omega)$ of the object $\mathcal{B}$ by using a two-step algorithm:

1. Construct the set $\mathcal{E}$ of those edges that are shared by a facet in $\mathcal{A}_+(\omega_0, \omega)$ and one not in it. The actual outer projection boundary (profile contour) of the object is not necessarily well approximated by the projection of this set of line segments, since $\mathcal{E}$ will usually also contain edges that are caused by other concavities and shadows, but are not part of the true outer boundary.

2. Project the edges found in step 1 onto the plane defined by the viewing direction ω. With line sweeping, remove those edges from the set that are contained between edges in both horizontal and vertical directions in the projection plane. This set of two-dimensional line segments is denoted by $\partial\mathcal{B}$.

We define the distance $d(e, P_0)$ between a point P_0 and a line segment e with end points P_1 and P_2 as follows. Let $d_1(e, P_0)$ be the perpendicular distance of the point P_0 from the line defined by P_1 and P_2 if its projection is inside the line segment, and $d_2(e, P_0)$ be the smaller one of the distances (P_0, P_1) and (P_0, P_2). Then we may set

$$d(e, P_0) = \min\{d_1(e, P_0), d_2(e, P_0)\}. \tag{1}$$

Now a goodness-of-fit measure between the model boundary $\partial\mathcal{B}$ and a set $\varkappa$ of the observed profile contour points $\varkappa_i$ can be defined as follows:

$$\chi^2_{\mathrm{pc}} = \sum_{e\in\partial\mathcal{B}} \min_i d(e, \varkappa_i) + \sum_i \min_{e\in\partial\mathcal{B}} d(e, \varkappa_i). \tag{2}$$

We usually assume that the displacement of the model profile contour with respect to the observed contour in the viewing plane is unknown. The optimal offset parameters must then be determined during the inversion algorithm as in Kaasalainen (2011).

Partial derivatives with respect to the shape parameters

In this appendix we consider in detail how to calculate derivatives with respect to the shape parameters. Since the Fourier transform of projected polyhedron is the weighted sum of projected facets, it is enough to consider the contribution of one facet.

We will calculate the derivatives with respect to vertex coordinates, since the Fourier transform of the projection depends on parametrization only through vertex coordinates. Derivatives with respect to parameters can then be obtained using the chain rule. Let (x_i, y_i, z_i), $i = 1, 2, 3$ be the coordinates of the vertices forming the facet and (a_i, b_i) projected coordinates obtained from the original coordinates using a projection matrix M. As previously explained, the contribution of a visible and illuminated facet to frequency point $(u, v) \neq (0, 0)$ can be calculated using the Green's theorem as follows:

$$\mathcal{F}(u,v) = e^{2\pi\imath(o_x u + o_y v)} B \left(\mathcal{I}_{12}(u,v) + \mathcal{I}_{23}(u,v) + \mathcal{I}_{31}(u,v) \right),$$

where

$$\mathcal{I}_{ij}(u,v) = \begin{cases} -\frac{\imath\left((b_i - b_j)v + (a_i - a_j)v\right)}{2\pi(u^2+v^2)} e^{-2\pi\imath(a_j u + b_j v)} \text{ if } (a_i - a_j)u + (b_i - b_j)v = 0 \\ \frac{1}{4\pi^2(u^2+v^2)} \frac{(b_i - b_j)u - (a_i - a_j)v}{(a_i - a_j)u + (b_i - b_j)v} (e^{-2\pi\imath(a_i u + b_i v)} - e^{-2\pi\imath(a_j u + b_j v)}). \end{cases}$$

The offset term (o_x, o_y) corresponds to the offset between the projected model and the data image, and it is usually determined during the optimization process. In what follows, we ignore the offset term. The brightness factor B depends on vertex coordinates through the facet normal $\mathbf{n}$. In the case $(u, v) = (0, 0)$, the value of $\mathcal{F}(u, v)$ is the total brightness of the projected facet. Derivatives of $\mathcal{I}_{ij}$ with respect to the projected vertex coordinates are straightforward to calculate. We consider only the case $(a_i - a_j)u + (b_i - b_j)v \neq 0$. We write

$$G = e^{-2\pi\imath(a_i u + b_i v)} - e^{-2\pi\imath(a_j u + b_j v)} \text{ and } H = \frac{1}{4\pi^2(u^2+v^2)} \frac{(b_i - b_j)u - (a_i - a_j)v}{(a_i - a_j)u + (b_i - b_j)v}.$$

Now the partial derivative of $\mathcal{I}_{ij}$ with respect to a projected vertex coordinate x may be written as

$$\frac{\partial \mathcal{I}_{ij}}{\partial x} = \frac{\partial H}{\partial x} G + H \frac{\partial G}{\partial x},$$

where

$$\begin{aligned}
\frac{\partial H}{\partial a_i} &= \frac{1}{4\pi^2} \frac{b_j - b_i}{((a_i - a_j)u + (b_i - b_j)v)^2} \\
\frac{\partial H}{\partial a_j} &= \frac{1}{4\pi^2} \frac{b_i - b_j}{((a_i - a_j)u + (b_i - b_j)v)^2} \\
\frac{\partial H}{\partial b_i} &= \frac{1}{4\pi^2} \frac{a_i - a_j}{((a_i - a_j)u + (b_i - b_j)v)^2} \\
\frac{\partial H}{\partial b_i} &= \frac{1}{4\pi^2} \frac{a_j - a_i}{((a_i - a_j)u + (b_i - b_j)v)^2} \\
\frac{\partial G}{\partial a_i} &= -2\pi\imath u e^{-2\pi\imath(a_i u + b_i v)} \\
\frac{\partial G}{\partial a_j} &= 2\pi\imath u e^{-2\pi\imath(a_j u + b_j v)} \\
\frac{\partial G}{\partial b_i} &= -2\pi\imath v e^{-2\pi\imath(a_i u + b_i v)} \\
\frac{\partial G}{\partial b_j} &= 2\pi\imath v e^{-2\pi\imath(a_j u + b_j v)}
\end{aligned}$$

Using the same notation as in 7, the 3×2 projection matrix can be written in the form

$$M = P \cdot R_C \cdot R_z(\lambda) \cdot R_y(\beta) \cdot R_z(w \cdot t),$$

where β is the ecliptic latitude, λ is the ecliptic longitude, and w is the rotation rate. The matrix M does not depend on the vertex coordinates, so we may write

$$\begin{aligned}
\frac{\partial a_i}{\partial x_i} &= M_{11} & \frac{\partial a_i}{\partial y_i} &= M_{12} & \frac{\partial a_i}{\partial z_i} &= M_{13} \\
\frac{\partial b_i}{\partial b_i} &= M_{21} & \frac{\partial b_i}{\partial y_i} &= M_{22} & \frac{\partial b_i}{\partial z_i} &= M_{23}
\end{aligned}$$

The partial derivative of I_{ij} with respect a vertex coordinate x can be written as

$$\frac{\partial I_{ij}}{\partial x} = \frac{\partial I_{ij}}{\partial a_i}\frac{\partial a_i}{\partial x} + \frac{\partial I_{ij}}{\partial b_i}\frac{\partial b_i}{\partial x} + \frac{\partial I_{ij}}{\partial a_j}\frac{\partial a_j}{\partial x} + \frac{\partial I_{ij}}{\partial b_j}\frac{\partial b_j}{\partial x}.$$

Finally

$$\frac{\partial \mathcal{F}}{\partial x}(u, v) = \frac{\partial B}{\partial x}(I_{12} + I_{23} + I_{31}) + B\left(\frac{\partial I_{12}}{\partial x} + \frac{\partial I_{23}}{\partial x} + \frac{\partial I_{21}}{\partial x}\right).$$

For adaptive optics and range-Doppler radar, B and its partial derivatives are straightforward to calculate, because it depends only on the facet normal and the viewing geometry. In the case of thermal infrared, it is more complicated as the surface temperature depends on the past values of solar insolation.

In the following we use the same notation as in the section 5.5. The insolation factor $\mathrm{ins}(\phi, p)$ is a periodic function of the rotation angle ϕ with the period 2π. For each facet p with the unit normal n and illumination direction E_0, we may write

$$\mathrm{ins}(\phi, p) = \max\left(\mathrm{n} \cdot R\left(\frac{w}{\phi}\right)^T E_0, 0\right)$$

where $R(t) = R_z(\lambda) \cdot R_y(\beta) \cdot R_z(wt)$. The function $\mathrm{ins}(\phi_i, p)$ may be expanded into Fourier series (approximately)

$$\mathrm{ins}(\phi, p) = \sum d_n e^{in\phi}.$$

The coefficients d_n can be calculated using the FFT: function $\mathrm{ins}(\phi, p)$ is uniformly sampled at N points ϕ_i, and N-point sequence (e_n) is obtained with the FFT. The Fourier series coefficient d_n is just e_n/N. We are only interested in coefficients d_n, $n = 0, \ldots, \frac{N}{2} - 1$, since $\mathrm{ins}(\phi, p)$ is a real-valued function.

We need to calculate the partial derivatives of d_n with respect to the vertex coordinates and rotation angles. These partial derivatives may be approximated by expanding

$$\frac{\partial\,\mathrm{ins}}{\partial x}(\phi, p) = \begin{cases} 0 & \text{if not illuminated} \\ \frac{\partial \mathbf{n}}{\partial x} \cdot R^T(\frac{w}{\phi})E_0 & \text{if x is a vertex coordinate} \\ \mathbf{n} \cdot \frac{\partial R^T}{\partial x}(\frac{w}{\phi})E_0 & \text{if x is } \beta \text{ or } \lambda \end{cases}$$

into Fourier series with coefficients c_n. We will use approximations $\frac{\partial d_n}{\partial x} = c_n$ and $\frac{\partial d_n}{\partial w} = 0$. Now

$$\frac{\partial T_0}{\partial d_0} = \frac{1}{4}\left(\frac{(1-A)F_0}{\epsilon\sigma}\right)^{\frac{1}{4}} d_0^{-\frac{3}{4}},$$

$$\frac{\partial \Theta_n}{\partial T0} = T_0^{-4}\frac{-3\Gamma}{4\epsilon\sigma}\sqrt{\frac{nw}{172800}},$$

$$\frac{\partial \Psi_n}{\partial \Theta_n} = -(1 + 2\Theta_n + 2\Theta_n^2)^{-\frac{3}{2}}(1 + 2\Theta_n),$$

$$\frac{\partial \Delta\phi_n}{\partial \Theta_n} = \frac{1}{(\Theta_n + 1)^2 + \Theta_n^2}.$$

Using the chain rule, we get

$$\frac{\partial \Psi_n}{\partial x} = \frac{\partial \Psi_n}{\partial \Theta_n}\frac{\partial \Theta_n}{\partial T_0}\frac{\partial T_0}{\partial d_0}\frac{\partial d_0}{\partial x}$$

and

$$\frac{\partial \Delta\phi_n}{\partial x} = \frac{\partial \Delta\phi_n}{\partial \Theta_n}\frac{\partial \Theta_n}{\partial T_0}\frac{\partial T_0}{\partial d_0}\frac{\partial d_0}{\partial x}.$$

Finally, the partial derivative of the sum (5.10) with respect to the vertex coordinates or the angles λ and β can be written as

$$\begin{aligned}\frac{\partial T^4}{\partial x} =& \frac{(1-A)F_0}{\epsilon\sigma}\Bigg(\Psi_0\frac{\partial d_0}{\partial x} + d_0\frac{\partial \Psi_0}{\partial x} \\ &+ 2\Re\left(\sum_{n=1}^{n=\frac{N}{2}-1}\left(\frac{\partial \Psi_n}{\partial x}d_n + \Psi_n\frac{\partial d_n}{\partial x} - \Psi_n d_n \imath\frac{\partial \Delta\phi_n}{\partial x}\right)e^{\imath(nwt-\Delta\phi_n)}\right)\Bigg).\end{aligned}$$

The partial derivative with respect to w can be calculated similarly.

Bibliography

Alliez, P. and Lévy, B., *Polygon mesh processing*. CRC Press, 2010.

ALMA Partnership, Hunter, T. R., Kneissl, R., Moullet, A., Brogan, C. L., Fomalont, E. B., Vlahakis, C., Asaki, Y., Barkats, D., Dent, W. R. F., Hills, R., Hirota, A., Hodge, J. A., Impellizzeri, C. M. V., Liuzzo, E., Lucas, R., Marcelino, N., Matsushita, S., Nakanishi, K., Perez, L. M., Phillips, N., Richards, A. M. S., Toledo, I., Aladro, R., Broguiere, D., Cortes, J. R., Cortes, P. C., Dhawan, V., Espada, D., Galarza, F., Garcia-Appadoo, D., Guzman-Ramirez, L., Hales, A. S., Humphreys, E. M., Jung, T., Kameno, S., Laing, R. A., Leon, S., Marconi, G., Nikolic, B., Nyman, L.-A., Radiszcz, M., Remijan, A., Rodon, J. A., Sawada, T., Takahashi, S., Tilanus, R. P. J., Vila Vilaro, B., Watson, L. C., Wiklind, T., de Gregorio, I., Di Francesco, J., Mangum, J., Francke, H., Gallardo, J., Garcia, J., Gonzalez, S., Hill, T., Kaminski, T., Kurono, Y., Lopez, C., Morales, F., Plarre, K., Randall, S., van kempen, T., Videla, L., Villard, E., Andreani, P., Hibbard, J. E., and Tatematsu, K., "ALMA Observations of Asteroid 3 Juno at 60 Kilometer Resolution," *ArXiv e-prints*, Mar. 2015.

Bertotti, B., Farinella, P., and Vokrouhlickỳ, D., *Physics of the Solar System: Dynamics and Evolution, Space Physics, and Spacetime Structure*, ser. Astrophysics and space science library. Kluwer Academic Publishers, 2003. [Online]. Available: http://books.google.fi/books?id=i-YvHNPEqAIC

Beuzit, J.-L., Feldt, M., Dohlen, K., Mouillet, D., Puget, P., Wildi, F., Abe, L., Antichi, J., Baruffolo, A., Baudoz, P., Boccaletti, A., Carbillet, M., Charton, J., Claudi, R., Downing, M., Fabron, C., Feautrier, P., Fedrigo, E., Fusco, T., Gach, J.-L., Gratton, R., Henning, T., Hubin, N., Joos, F., Kasper, M., Langlois, M., Lenzen, R., Moutou, C., Pavlov, A., Petit, C., Pragt, J., Rabou, P., Rigal, F., Roelfsema, R., Rousset, G., Saisse, M., Schmid, H.-M., Stadler, E., Thalmann, C., Turatto, M., Udry, S., Vakili, F., and Waters, R., "Sphere: a 'planet finder' instrument for the vlt," *Proc. SPIE*, vol. 7014, pp. 701 418–701 418–12, 2008.

Bracewell, R., *Fourier analysis and imaging*. Springer, 2003.

Carry, B., Kaasalainen, M., Merline, W. J., Müller, T. G., Jorda, L., Drummond, J. D., Berthier, J., O'Rourke, L., Ďurech, J., Küppers, M., Conrad, A., Tamblyn, P., Dumas, C., Sierks, H., and Osiris Team, "Shape modeling technique koala validated by esa rosetta at (21) lutetia," *Planetary and Space Science*, vol. 66, pp. 200–212, Jun. 2012.

Carry, B., Dumas, C., Kaasalainen, M., Berthier, J., Merline, W. J., Erard, S., Conrad, A., Drummond, J. D., Hestroffer, D., Fulchignoni, M., and Fusco, T., "Physical properties of (2) pallas," *Icarus*, vol. 205, no. 2, pp. 460 – 472, 2010. [Online]. Available: http://www.sciencedirect.com/science/article/pii/S0019103509003467

Delbo, M., "The nature of near-earth asteroids from the study of their thermal infrared emission," Ph.D. dissertation, Freie Universitat Berlin, 2004.

Dobrovolskis, A. R., "Inertia of any polyhedron," *Icarus*, vol. 124, no. 2, pp. 698 – 704, 1996.

Dohlen, K., Langlois, M., Saisse, M., Hill, L., Origne, A., Jacquet, M., Fabron, C., Blanc, J.-C., Llored, M., Carle, M., Moutou, C., Vigan, A., Boccaletti, A., Carbillet, M., Mouillet, D., and Beuzit, J.-L., "The infra-red dual imaging and spectrograph for SPHERE: design and performance," in *Society of Photo-Optical Instrumentation Engineers (SPIE) Conference Series*, ser. Society of Photo-Optical Instrumentation Engineers (SPIE) Conference Series, vol. 7014, Jul. 2008, p. 3.

Drummond, J. and Christou, J., "The Adaptive Optics Point Spread Function from Keck and Gemini," in *Advanced Maui Optical and Space Surveillance Technologies Conference*, 2009, p. 65.

Ďurech, J. and Kaasalainen, M., "Photometric signatures of highly nonconvex and binary asteroids," *Astronomy and Astrophysics*, vol. 404, pp. 709–714, 2003.

Ďurech, J., Vokrouhlický, D., Baransky, A. R., Breiter, S., Burkhonov, O. A., Cooney, W., Fuller, V., Gaftonyuk, N. M., Gross, J., Inasaridze, R. Y., Kaasalainen, M., Krugly, Y. N., Kvaratshelia, O. I., Litvinenko, E. A., Macomber, B., Marchis, F., Molotov, I. E., Oey, J., Polishook, D., Pollock, J., Pravec, P., Sárneczky, K., Shevchenko, V. G., Slyusarev, I., Stephens, R., Szabó, G., Terrell, D., Vachier, F., Vanderplate, Z., Viikinkoski, M., and Warner, B. D., "Analysis of the rotation period of asteroids (1865) Cerberus, (2100) Ra-Shalom, and (3103) Eger - search for the YORP effect," *Astronomy & Astrophysics*, vol. 547, p. A10, Nov. 2012.

Ďurech, J., Carry, B., Delbo, M., Kaasalainen, M., and Viikinkoski, M., "Asteroid Models from Multiple Data Sources," *Asteroids IV*, 2015.

Ďurech, J., Kaasalainen, M., Herald, D., Dunham, D., Timerson, B., Hanuš, J., Frappa, E., Talbot, J., Hayamizu, T., Warner, B. D., Pilcher, F., and Galád, A., "Combining asteroid models derived by lightcurve inversion with asteroidal occultation silhouettes," *Icarus*, vol. 214, no. 2, pp. 652 – 670, 2011. [Online]. Available: http://www.sciencedirect.com/science/article/pii/S0019103511001072

Favaro, P. and Soatto, S., *3-d shape estimation and image restoration: Exploiting defocus and motion-blur*. Springer Science & Business Media, 2007.

Fusco, T., Rousset, G., Sauvage, J.-F., Petit, C., Beuzit, J.-L., Dohlen, K., Mouillet, D., Charton, J., Nicolle, M., Kasper, M., Baudoz, P., and Puget, P., "High-order adaptive optics requirements for direct detection of extrasolar planets: Application to the SPHERE instrument," *Optics Express*, vol. 14, p. 7515, 2006.

Gardner, R., *Geometric Tomography*, ser. Encyclopedia of Mathematics and its Applications. Cambridge University Press, 2006, no. v. 13.

Hapke, B., "Bidirectional reflectance spectroscopy: 1. theory," *Journal of Geophysical Research: Solid Earth*, vol. 86, no. B4, pp. 3039–3054, 1981. [Online]. Available: http://dx.doi.org/10.1029/JB086iB04p03039

Hezaveh, Y. D., Marrone, D. P., Fassnacht, C. D., Spilker, J. S., Vieira, J. D., Aguirre, J. E., Aird, K. A., Aravena, M., Ashby, M. L. N., Bayliss, M., Benson, B. A., Bleem, L. E., Bothwell, M., Brodwin, M., Carlstrom, J. E., Chang, C. L., Chapman, S. C., Crawford, T. M., Crites, A. T., Breuck, C. D., de Haan, T., Dobbs, M. A., Fomalont, E. B., George, E. M., Gladders, M. D., Gonzalez, A. H., Greve, T. R., Halverson, N. W., High, F. W., Holder, G. P., Holzapfel, W. L., Hoover, S., Hrubes, J. D., Husband, K., Hunter, T. R., Keisler, R., Lee, A. T., Leitch,

E. M., Lueker, M., Luong-Van, D., Malkan, M., McIntyre, V., McMahon, J. J., Mehl, J., Menten, K. M., Meyer, S. S., Mocanu, L. M., Murphy, E. J., Natoli, T., Padin, S., Plagge, T., Reichardt, C. L., Rest, A., Ruel, J., Ruhl, J. E., Sharon, K., Schaffer, K. K., Shaw, L., Shirokoff, E., Stalder, B., Staniszewski, Z., Stark, A. A., Story, K., Vanderlinde, K., Weiß, A., Welikala, N., and Williamson, R., "Alma observations of spt-discovered, strongly lensed, dusty, star-forming galaxies," *The Astrophysical Journal*, vol. 767, no. 2, p. 132, 2013. [Online]. Available: http://stacks.iop.org/0004-637X/767/i=2/a=132

Hom, E. F. Y., Marchis, F., Lee, T. K., Haase, S., Agard, D. A., and Sedat, J. W., "Aida: an adaptive image deconvolution algorithm with application to multi-frame and three-dimensional data," *J. Opt. Soc. Am. A*, vol. 24, no. 6, pp. 1580–1600, Jun 2007. [Online]. Available: http://josaa.osa.org/abstract.cfm?URI=josaa-24-6-1580

Jansson, P., *Deconvolution of Images and Spectra*, ser. Dover Books on Engineering Series. Dover Publications, 2012. [Online]. Available: https://books.google.fi/books?id=LQr8aHaMs08C

Kaasalainen, M. and Torppa, J., "Optimization methods for asteroid lightcurve inversion: I. shape determination," *Icarus*, vol. 153, no. 1, pp. 24 – 36, 2001. [Online]. Available: http://www.sciencedirect.com/science/article/pii/S0019103501966734

Kaasalainen, M. and Viikinkoski, M., "Shape reconstruction of irregular bodies with multiple complementary data sources." *Astronomy & Astrophysics*, vol. 543, no. A97, 2012. [Online]. Available: http://www.aanda.org/articles/aa/abs/2012/07/aa19267-12/aa19267-12.html

Kaasalainen, M., Torppa, J., and Muinonen, K., "Optimization methods for asteroid lightcurve inversion: Ii. the complete inverse problem," *Icarus*, vol. 153, no. 1, pp. 37 – 51, 2001. [Online]. Available: http://www.sciencedirect.com/science/article/pii/S0019103501966746

Kaasalainen, M., Mottola, S., and Fulchignoni, M., "Asteroid Models from Disk-integrated Data," *Asteroids III*, pp. 139–150, 2002.

Kaasalainen, M., Torppa, J., and Piironen, J., "Binary structures among large asteroids," *Astronomy and Astrophysics*, vol. 383, pp. L19–L22, Mar. 2002.

Kaasalainen, M., "Multimodal inverse problems: Maximum compatibility estimate and shape reconstruction," *Inverse Problems and Imaging*, vol. 5, no. 1, pp. 37–57, 2011.

Kaasalainen, M. and Ďurech, J., "Inverse problems of neo photometry: Imaging the neo population," *Proceedings of the International Astronomical Union*, vol. 2, no. S236, pp. 151–166, 2006.

Kaasalainen, M. and Lamberg, L., "Inverse problems of generalized projection operators," *Inverse Problems*, vol. 22, no. 3, p. 749, 2006.

Kaasalainen, M., Pravec, P., Krugly, Y. N., Šarounová, L., Torppa, J., Virtanen, J., Kaasalainen, S., Erikson, A., Nathues, A., Ďurech, J. *et al.*, "Photometry and models of eight near-earth asteroids," *Icarus*, vol. 167, no. 1, pp. 178–196, 2004.

Kobbelt, L., "$\sqrt{3}$-subdivision," in *Proceedings of the 27th annual conference on Computer graphics and interactive techniques*. ACM Press/Addison-Wesley Publishing Co., 2000, pp. 103–112.

Labeyrie, A., Lipson, S. G., and Nisenson, P., *An introduction to optical stellar interferometry*. Cambridge University Press, 2006.

Lenzen, R., Hartung, M., Brandner, W., Finger, G., Hubin, N. N., Lacombe, F., Lagrange, A.-M., Lehnert, M. D., Moorwood, A. F. M., and Mouillet, D., "NAOS-CONICA first on sky results in a variety of observing modes," in *Society of Photo-Optical Instrumentation Engineers (SPIE) Conference Series*, ser. Society of Photo-Optical Instrumentation Engineers (SPIE) Conference Series, Iye, M. and Moorwood, A. F. M., Eds., vol. 4841, 2003, pp. 944–952.

Loop, C., "Smooth subdivision surfaces based on triangles," Master's thesis, University of Utah, 1987.

Mueller, M., "Surface properties of asteroids from mid-infrared observations and thermophysical modeling," Ph.D. dissertation, Freie Universitaet Berlin, 2007.

Mugnier, L. M., Fusco, T., and Conan, J.-M., "Mistral: a myopic edge-preserving image restoration method, with application to astronomical adaptive-optics-corrected long-exposure images," *J. Opt. Soc. Am. A*, vol. 21, no. 10, pp. 1841–1854, Oct 2004. [Online]. Available: http://josaa.osa.org/abstract.cfm?URI=josaa-21-10-1841

Naidu, S. P., Margot, J.-L., Busch, M. W., Taylor, P. A., Nolan, M. C., Brozovic, M., Benner, L. A., Giorgini, J. D., and Magri, C., "Radar imaging and physical characterization of near-earth asteroid (162421) 2000 et70," *Icarus*, vol. 226, no. 1, pp. 323–335, 2013.

Nesvorný, D. and Vokrouhlický, D., "Analytic Theory for the Yarkovsky-O Effect on Obliquity," *The Astronomical Journal*, vol. 136, pp. 291–299, Jul. 2008.

Nolan, M., Bramson, A., and Magri, C., "Radar scattering functions using itokawa as ground truth," in *Asteroids, Comets and Meteors in Helsinki*, 2014.

Osher, S. and Fedkiw, R., *Level set methods and dynamic implicit surfaces*. Springer Science & Business Media, 2006, vol. 153.

Ostro, S. J., Scott, R., Hudson, Nolan, M. C., Margot, J.-L., Scheeres, D. J., Campbell, D. B., Magri, C., Giorgini, J. D., and Yeomans, D. K., "Radar observations of asteroid 216 kleopatra," *Science*, vol. 288, no. 5467, pp. 836–839, 2000.

Ostro, S. J., Hudson, R. S., Benner, L. A., Giorgini, J. D., Magri, C., Margot, J.-L., and Nolan, M. C., "Asteroid radar astronomy," *Asteroids III. Univ. of Arizona Press, Tucson*, pp. 151–168, 2002.

Ostro, S. J., Benner, L. A. M., Magri, C., Giorgini, J. D., Rose, R., Jurgens, R. F., Yeomans, D. K., Hine, A. A., Nolan, M. C., Scheeres, D. J., Broschart, S. B., Kaasalainen, M., and Margot, J.-L., "Radar observations of itokawa in 2004 and improved shape estimation," *Meteoritics & Planetary Science*, vol. 40, no. 11, pp. 1563–1574, 2005. [Online]. Available: http://dx.doi.org/10.1111/j.1945-5100.2005.tb00131.x

Pravec, P. and Harris, A. W., "Asteroid rotations," *Asteroids III*, vol. 113, 2002.

Riley, K., Hobson, M., and Bence, S., *Mathematical Methods for Physics and Engineering: A Comprehensive Guide*. Cambridge University Press, 2006.

Rousset, G., Lacombe, F., Puget, P., Hubin, N. N., Gendron, E., Fusco, T., Arsenault, R., Charton, J., Feautrier, P., Gigan, P., Kern, P. Y., Lagrange, A.-M., Madec, P.-Y., Mouillet, D., Rabaud, D., Rabou, P., Stadler, E., and Zins, G., "NAOS, the first AO system of the VLT: on-sky performance," in *Society of Photo-Optical Instrumentation Engineers (SPIE) Conference Series*, ser. Society of Photo-Optical Instrumentation Engineers (SPIE) Conference Series, Wizinowich, P. L. and Bonaccini, D., Eds., vol. 4839, 2003, pp. 140–149.

Steward, E., *Fourier Optics: An Introduction (Second Edition)*, ser. Dover Books on Physics Series. Dover Publications, Incorporated, 2012. [Online]. Available: https://books.google.fi/books?id=0GCyu--TK3cC

van Dam, M. A., Le Mignant, D., and Macintosh, B. A., "Performance of the Keck Observatory Adaptive-Optics System," *Applied Optics*, vol. 43, pp. 5458–5467, 2004.

Viikinkoski, M., "Adam software," 2015. [Online]. Available: https://github.com/matvii/adam-asteroid

Werner, R. A., "The gravitational potential of a homogeneous polyhedron or don't cut corners," *Celestial Mechanics and Dynamical Astronomy*, vol. 59, pp. 253–278, Jul. 1994.

Wizinowich, P. L., Acton, D. S., Lai, O., Gathright, J., Lupton, W., and Stomski, P. J., "Performance of the W.M. Keck Observatory Natural Guide Star Adaptive Optic Facility: the first year at the telescope," in *Society of Photo-Optical Instrumentation Engineers (SPIE) Conference Series*, ser. Society of Photo-Optical Instrumentation Engineers (SPIE) Conference Series, Wizinowich, P. L., Ed., vol. 4007, 2000, pp. 2–13.

Zacharopoulos, A. D., Arridge, S. R., Dorn, O., Kolehmainen, V., and Sikora, J., "Three-dimensional reconstruction of shape and piecewise constant region values for optical tomography using spherical harmonic parametrization and a boundary element method," *Inverse Problems*, vol. 22, no. 5, p. 1509, 2006. [Online]. Available: http://stacks.iop.org/0266-5611/22/i=5/a=001

Zhang, R., Tsai, P.-S., Cryer, J. E., and Shah, M., "Shape-from-shading: a survey," *Pattern Analysis and Machine Intelligence, IEEE Transactions on*, vol. 21, no. 8, pp. 690–706, 1999.

Publications

Publication I

Kaasalainen M. and Viikinkoski M., "Shape reconstruction of irregular bodies with multiple complementary data sources," *Astronomy & Astrophysics* 543 (2012):A97

Reproduced with permission from Astronomy & Astrophysics, ©ESO 2012

A&A 543, A97 (2012)
DOI: 10.1051/0004-6361/201219267
© ESO 2012

Astronomy & Astrophysics

Shape reconstruction of irregular bodies with multiple complementary data sources

M. Kaasalainen and M. Viikinkoski

Department of Mathematics, Tampere University of Technology, PO Box 553, 33101 Tampere, Finland
e-mail: mikko.kaasalainen@tut.fi

Received 22 March 2012 / Accepted 14 May 2012

ABSTRACT

We discuss inversion methods for shape reconstruction with complementary data sources. The current main sources are photometry, adaptive optics or other images, occultation timings, and interferometry, and the procedure can readily be extended to include range-Doppler radar and thermal infrared data as well. We introduce the octantoid, a generally applicable shape support that can be automatically used for surface types encountered in planetary research, including strongly nonconvex or non-starlike shapes. We present models of Kleopatra and Hermione from multimodal data as examples of this approach. An important concept in this approach is the optimal weighting of the various data modes. We define the maximum compatibility estimate, a multimodal generalization of the maximum likelihood estimate, for this purpose. We also present a specific version of the procedure for asteroid flyby missions, with which one can reconstruct the complete shape of the target by using the flyby-based map of a part of the surface together with other available data. Finally, we show that the relative volume error of a shape solution is usually approximately equal to the relative shape error rather than its multiple. Our algorithms are trivially parallelizable, so running the code on a CUDA-enabled graphics processing unit is some two orders of magnitude faster than the usual single-processor mode.

Key words. methods: data analysis – methods: numerical – techniques: high angular resolution – techniques: interferometric – techniques: photometric – minor planets, asteroids: general

1. Introduction

Photometric measurements, i.e., lightcurves (sparse or dense), are the main data source for the physical modelling of asteroids. This is because they are in principle available for all targets that can be observed in the first place, and they allow a unique (usually global convex) shape and pole/period solution (Kaasalainen et al. 1992, 2001; Ďurech & Kaasalainen 2003; Kaasalainen 2004; Ďurech et al. 2005; Kaasalainen & Lamberg 2006, henceforth KL06). Lightcurves can also be used to determine more complex spin states (Kaasalainen 2001; Kaasalainen et al. 2007; Scheirich et al. 2010) or colour maps over the surface using filters of various wavelengths (Nathues et al. 2005). Other data sources providing more detailed information are available for a much smaller portion of asteroids. In addition to space mission targets, these include asteroids that have a large enough apparent diameter for some resolution in adaptive optics images, interferometric measurements, or occultation timings, or come close enough for radar observations. Though this portion is relatively small, it nevertheless comprises several hundreds or even thousands of targets, so standard procedures for analysing these in the same way as lightcurve-only targets are necessary. In KL06, it was shown that all the aforementioned data types are different versions of generalized projections of the objects, and hence have some common mathematical properties.

The most natural way of modelling targets with datasets from various data sources is to combine all the datasets and analyse them simultaneously. In Kaasalainen (2011, henceforth K11), a general scheme was introduced for combining lightcurves and adaptive optics images to produce more detailed nonconvex shape models, and the uniqueness properties and computational aspects of the problem were discussed. The ground truth validating this scheme via the Lutetia flyby of the Rosetta probe (Sierks et al. 2011) was presented in Carry et al. (2012). Occultation timings are essentially profile projections of the object and can be modelled in the same way as adaptive optics profiles (Ďurech et al. 2012). The use of interferometric data is described in KL06 and, in more detail, in this paper. Radar data have been used for modelling tens of asteroids (Ostro et al. 2002; Magri et al. 2011, and references therein), and the uniqueness properties and information content of these were discussed in KL06. Including radar data in our formalism is straightforward, and we discuss this in a forthcoming paper.

This paper is an addition to a series of reports on our ongoing project of using all available data sources to model asteroids. The aim of this paper is to expand and complement the formalism of the aforementioned papers to include i) a shape support for general shapes, including non-starlike ones (Sects. 2 and 3.1); ii) interferometric measurements (Sect. 3.2); and iii) a technique for modelling the complete asteroid surface using flyby images combined with other data (Sect. 6). In addition, we present some examples of these (Sect. 5) and review the principle of finding the optimal weights for various data modalities (Sect. 4). We discuss future work in Sect. 7.

2. General shape representation: octantoids

Our aim is to find a general surface parametrization for the reconstruction of non-starlike shapes from generalized projections. A popular approach is the usual spherical harmonics representation in which each coordinate function is represented independently as a spherical harmonics series (see, e.g., Zacharopoulos et al. 2006). However, while this parametrization is powerful enough to represent any shape that can be

parametrized on the unit sphere S^2 (with sufficient continuity properties), it requires excessive smoothness regularization during the inversion process. What is more, the actual topology of the mesh of the evaluation points on the surface may change during iteration (which does not happen in the starlike case): the mesh can cross itself and become "tangled" as its vertices are allowed to move freely. Thus, instead of trying to find a regularization method to stabilize the surface topology, we decided to try a different approach of defining a representation that is general enough to represent non-starlike asteroid shapes, yet more stable than the usual spherical harmonics representation in the inversion process.

We consider surfaces that can be represented in the form

$$\boldsymbol{x}(\theta,\varphi) = \begin{cases} x(\theta,\varphi) = & \mathrm{e}^{a(\theta,\varphi)} \sin\theta\cos\varphi, \\ y(\theta,\varphi) = & \mathrm{e}^{a(\theta,\varphi)+b(\theta,\varphi)} \sin\theta\sin\varphi, \\ z(\theta,\varphi) = & \mathrm{e}^{a(\theta,\varphi)+c(\theta,\varphi)} \cos\theta, \end{cases} \tag{1}$$

where a, b, and c are linear combinations of the (real) spherical harmonic functions $Y_l^m(\theta,\varphi)$, with coefficients $\{a_{lm}\}$, $\{b_{lm}\}$, and $\{c_{lm}\}$, respectively. The coordinates (θ,φ), $0 \le \theta \le \pi$, $0 \le \varphi < 2\pi$, parametrize the surface on the unit sphere S^2 but do not represent any physical directions such as polar coordinates. We use the exponential representation to ensure that the generalized radii e^a, e^{a+b}, and e^{a+c} are all positive.

It is clear that our representation is more restrictive than the general spherical harmonics representation, for the coordinate functions cannot change sign within each S^2-octant. We call shapes that can be rendered in the form (1) *octantoids*. For a body to be an octantoid, it must be possible to choose the origin (inside the body) and coordinate axes such that if the body is cut along the coordinate planes, there is only one piece from each octant (and the pieces join together smoothly). For example, the ellipsoid is the simplest octantoid, as it can be represented by Eq. (1) by choosing the functions a, b, and c to be constants so that the semiaxes are the generalized radii. A curved banana is an example of a strongly non-starlike octantoid. From irregular small asteroids to planets, the currently known shapes of solar system bodies are octantoids. A non-octantoid body is typically made of sculpted material with great tensile strength and has a markedly twisted shape, whereas processes guided by gravitation (accumulation etc.) tend to favour octantoid shapes.

The usual representation for starlike shapes can be obtained by setting $b = c = 0$ in the parametrization of Eq. (1). If we think of starlike surfaces as our basic "stable" shapes, an intuitively obvious measure for shape complexity is a weighted norm of the coefficients $\{b_{lm}\}$ and $\{c_{lm}\}$ (and possibly $\{a_{lm}\}$). We thus define

$$\eta = \sum_{l,m} l\left(b_{lm}^2 + c_{lm}^2\right), \quad \eta_0 = \sum_{l,m} l\left(a_{lm}^2 + b_{lm}^2 + c_{lm}^2\right). \tag{2}$$

We note that for an ellipsoid $\eta = 0 = \eta_0$, as the only nonzero coefficients are a_{00}, b_{00}, and c_{00}. This reflects the compact information content of the octantoid parametrization: representing an ellipsoid in the more usual starlike formulation with $b = c = 0$ would require an infinite spherical harmonics series for a. Using η_0 also formally solves the nonuniqueness problem of the choice of (θ,φ): for a given octantoid, the optimal parametrization is the one with the smallest η_0 (when the spherical harmonics series are truncated at some $l_{\max}$).

For the inversion algorithm, we assume that our surface is represented as a polytope with triangular facets. The vertex locations (θ_i,φ_i), $i = 1,...,N$, on the parametrizing unit sphere are obtained from a triangular mesh of the size N on the sphere, with any usual mesh topology (vertex connections; cf., e.g., Kaasalainen et al. 2001), and the actual vertex locations are then given by Eq. (1). Enforcing small values of η (or η_0) as regularization greatly stabilizes the procedure and improves convergence.

The regularization measure of Eq. (2) mostly affects the global surface shape. A regularization method for smoothing out more local irregularities is often required. We define a smoothing regularization function (K11), designed to minimize the sum of local nonconvex features, as

$$\gamma = \frac{1}{\sum_i A_i} \sum_{i\ j} A_j\left(1 - \nu_i \cdot \nu_j\right), \tag{3}$$

where A_i is the area of the facet i and ν_i its unit normal vector, $\nu \in S^2$. The sum is over all those facets j that are adjacent to the facet i and tilted above its plane. In the same vein, we introduce a physical regularization function for non-monolithic bodies by constraining the gravitational slope so that steep rubble-pile slopes are avoided:

$$\phi = \frac{1}{\sum_i A_i} \sum_i A_i[1 - \nu_i \cdot \nabla\Phi(x_i)], \tag{4}$$

where x_i is the centroid of the facet i, and $\Phi(x)$ is the gravitational potential computed from the tetrahedra formed by the centroid of the body and the facet triangles (see, e.g., Werner 1994). The gravitational slope for the facet i is $\arccos[\nu_i \cdot \nabla\Phi(x_i)]$.

The octantoid form of Eq. (1) can also be written for a set of independent vertices (rather than spherical harmonics series) by using $a(\theta_i,\varphi_i)$, $b(\theta_i,\varphi_i)$, and $c(\theta_i,\varphi_i)$ as a set of $3N$ free parameters, with smoothness regularization and, for instance, a penalty function $f(b,c)$ to suppress deviation from starlike shapes:

$$f(b,c) = \sum_i^N b(\theta_i,\varphi_i)^2 + c(\theta_i,\varphi_i)^2, \tag{5}$$

where b and c represent the set of values $b(\theta_i,\varphi_i)$ and $c(\theta_i,\varphi_i)$.

3. Data modes and their modelling

3.1. Non-starlike contours

The theoretical aspects of shape inversion from generalized profiles were extensively studied in KL06 and K11. Here we restrict ourselves to some practical observations of the goodness-of-fit measure and the optimization process.

Let ω and ω_0 be, respectively, the viewing and the illumination directions; $\omega_0, \omega \in S^2$. As the surface is no longer convex, the set of facets approximating the visible and illuminated portion $\mathcal{A}_+(\omega_0,\omega)$ of the surface is determined by ray-tracing. A computationally fast form of this determination, approximate but sufficiently accurate for most of our purposes and easily refinable for higher accuracy, was given in Kaasalainen et al. (2001). A facet with the unit normal vector ν is in $\mathcal{A}_+$ if the dot products $\omega \cdot \nu$ and $\omega_0 \cdot \nu$ are both positive, and the rays from the facet centroid to the directions ω and ω_0 do not intersect any other facet.

The use of the image boundary contours is necessary because it is considerably more reliable than using the pixel brightness values of adaptive optics images. The contour mode is also faster than the pixel one. For reliable pixel values, the goodness-of-fit measure of especially non-starlike objects is easiest to formulate in the pixel space. However, even in these cases the use of boundary contours is often necessary if one wishes to employ efficient gradient-based optimization procedures. An algorithm for

constructing the outer shadow and limb boundary of the projection of a polyhedron was outlined in K11. However, for a general non-starlike object, the construction is too time-consuming and complex to be used in an inversion algorithm. Instead, we construct an approximate image boundary $\partial\mathcal{B}(\omega_0, \omega)$ of the object $\mathcal{B}$ using a two-step algorithm:

1. Construct the set $\mathcal{E}$ of edges that are shared by a facet in $\mathcal{A}_+$ and one not in it. The actual outer projection boundary (profile contour) of the object is not necessarily well approximated by the projection of this set of line segments, since $\mathcal{E}$ usually also contains edges that are caused by other concavities and shadows, but are not part of the true outer boundary.
2. Project the edges found in step 1 onto the plane defined by the viewing direction ω. With line sweeping, remove those edges from the set that are contained between edges in both the horizontal and vertical directions in the projection plane. This set of two-dimensional line segments is denoted by $\partial\mathcal{B}(\omega_0, \omega)$.

We define the distance $d(e, P_0)$ between a point P_0 and a line segment e with end points P_1 and P_2 as follows. Let $d_1(e, P_0)$ be the perpendicular distance of the point P_0 from the line defined by P_1 and P_2 if its projection is inside the line segment, and $d_2(e, P_0)$ be the smaller one of the distances (P_0, P_1) and (P_0, P_2). We can then set

$$d(e, P_0) = \min\{d_1(e, P_0), d_2(e, P_0)\}. \tag{6}$$

A goodness-of-fit measure between the model boundary $\partial\mathcal{B}$ and a set $\varkappa$ of the observed profile contour points $\varkappa_i$ can be defined as follows:

$$\chi^2_{\rm pc} = \sum_{e\in\partial\mathcal{B}} \min_i d(e, \varkappa_i) + \sum_i \min_{e\in\partial\mathcal{B}} d(e, \varkappa_i). \tag{7}$$

We usually assume that the displacement of the model profile contour from the observed contour in the viewing plane is unknown. The optimal offset parameters must then be determined during the inversion as in K11.

3.2. Interferometry

As our second data source, we consider the interferometric projection operator (KL06). An interferometric curve is essentially obtained by projecting the image of the object on the POS to an interferometric base line in the same plane and convolving it with a point-spread-like instrument response function. In our case, the base line is one of the orthogonal axes of the Fine Guidance Sensor of the *Hubble* Space Telescope (HST/FGS), but the procedure presented here is generic for any interferometric case. To be more precise, the final observable response function $S(x)$ of the HST/FGS can be computed by convolving the brightness distribution $I(u, v)$ of the image of the object on the plane-of-sky (POS) with the template transfer function $T(x)$ of the instrument:

$$S(x) = \frac{1}{L}\int\int_{P_\omega(\mathcal{A}_+)} I(u, v)T(x_0 + x - u\cos\xi + v\sin\xi)\,{\rm d}u\,{\rm d}v, \tag{8}$$

where

$$L = \int\int_{P_\omega(\mathcal{A}_+)} I(u, v)\,{\rm d}u\,{\rm d}v \tag{9}$$

is the total brightness of the visible and illuminated part of the object, $P_\omega(\mathcal{A}_+)$ denotes the POS projection of $\mathcal{A}_+$, and ξ is the angle between the image u-axis and the FGS base line x-axis. A similar measurement is made in the y-direction perpendicular to x, and the parameters x_0 and y_0 are the location offset values of the object w.r.t. the FGS coordinates.

The template transfer function $T(x)$ cannot usually be written in an analytical form and is thus given as a set of sampled values. To obtain a continuous function, the transfer function is linearly interpolated between the sampled points so that we have a form suitable for gradient-based optimization (i.e., all parameters to be adjusted have existing and locally continuous partial derivatives w.r.t. the goodness-of-fit measure).

For a polytope, the integral can be easily computed for practical inversion. The visible and illuminated facets are determined by ray-tracing using the same approach as in the previous section[1]. In this case, we evaluate an integral over the POS, so we must have a sufficiently high resolution for the sampling points (u, v) even if the polyhedral model itself is not in high resolution. Indeed, it is computationally much more efficient to sprinkle each facet with a number of sampling points than to use many very small facets. For each facet f_i with $\omega\cdot\nu$ and $\omega_0\cdot\nu$ positive, we generate N points $\{p_{ij}\}$, $j = 1\ldots N$, uniformly distributed within the facet. The value of N, typically of order $N \sim 10$, depends on the resolution of the instrument, the size of the facets, and the apparent size of the target on the POS; this is simple to probe by noting when the numerical approximation of $S(x)$ with some test case starts to converge to the desired accuracy. The point p_{ij} on the facet f_i is visible if the rays from the point p_{ij} to the directions ω and ω_0 do not intersect any other facet. The integral in Eq. (8) can then be approximated as the sum

$$S^{\rm mod}(x) \approx \frac{1}{L}\sum_{f_i\in\mathcal{A}_+}\frac{B_i}{N}\sum_j T(x_0 + x - u_{ij}\cos\xi + v_{ij}\sin\xi), \tag{10}$$

where (u_{ij}, v_{ij}) is the projection of the point p_{ij} onto the plane defined by ω, B_i is the brightness of the facet f_i, and the inner sum is over all of those points in the facet that are visible and illuminated. The goodness-of-fit measure $\chi^2_{\rm sc}$ for an interferometric S-curve of M data points is of the usual form

$$\chi^2_{\rm sc} = \sum_{i=1}^{M}\left[S^{\rm obs}(x_i) - S^{\rm mod}(x_i)\right]^2. \tag{11}$$

4. Maximum compatibility estimate

In our problem of combining lightcurves and other data sources, the data modalities are complementary but incommensurable, which causes an additional problem: how exactly is the combined dataset defined? Ideally, the solution of the inverse problem should be independent of, e.g., noise level estimates or scale factors such as physical units. It should reflect the best compatibility estimate and the optimal relative weight factors of the data modes: how much does each mode bring reliable information into the solution? In this sense, one can even separate subsets of a single data mode: should data obtained in one set of conditions be weighted more than those acquired in another? This problem was addressed in K11, where a rigorous definition of the maximum compatibility estimate – a multimodal generalization of the

[1] The mathematical properties of generalized projections are helpful here from the computational point of view. We essentially have a common routine for computing the POS image of the target, and each data mode is just a different way of sampling that image. This makes it easy to add a plug-in module for a data source.

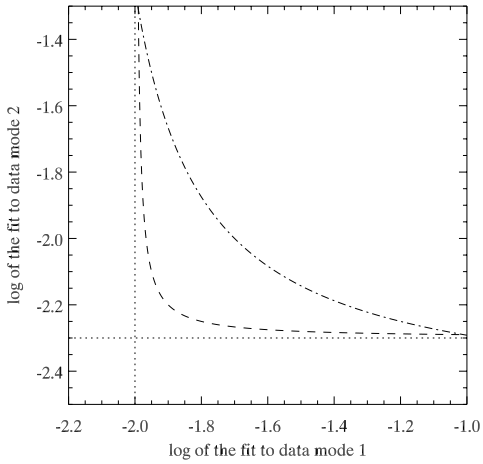

Fig. 1. A schematic of the curve $[x(\lambda), y(\lambda)]$ and the maximum compatibility estimate (the point closest to the new origin at the intersection of the dotted lines). The dashed line corresponds to a case with closely compatible data sources, while dot-dash indicates a case with systematic errors in models and/or data. The weight parameter λ for data mode 2 increases from left ($\lambda = 0$) to right ($\lambda = \infty$) on a curve.

maximum likelihood estimate – was derived. For convenience, we briefly review this formulation.

Let us choose as goodness-of-fit measures some functions δ_i, $i = 1, \ldots, n$, of n data modalities. Typically, δ is the usual χ^2-fit form. Our task is to construct a joint $\delta_{\rm tot}$ with well-defined weighting for each data mode:

$$\delta_{\rm tot}(P, D) = \delta_1(P, D_1) + \sum_{i=2}^{n} \lambda_{i-1}\delta_i(P, D_i), \quad D = \{D_i\} \tag{12}$$

(to which regularization functions $g(P)$ can be added), where D_i denotes the data from the source i, and P is the set of model parameter values.

The principle of deriving the maximum compatibility estimate is easiest first to describe in two dimensions. We can plot the separate fit levels for each δ_i, obtained by minimizing $\delta_{\rm tot}$ at various λ in the $(\log\delta_1, \log\delta_2)$-plane, denoting

$$\begin{aligned} x(\lambda) &= \log\delta_1 \left[\arg\min_P \delta_{\rm tot}(P)|_\lambda\right], \\ y(\lambda) &= \log\delta_2 \left[\arg\min_P \delta_{\rm tot}(P)|_\lambda\right], \end{aligned} \tag{13}$$

(the logarithm keeps the shape of the plot invariant in, e.g., unit conversions as multiplicative factors in δ_i are converted to translations in the plot plane). We can also translate the origin to (X, Y) given by

$$\begin{aligned} X &= x(\lambda)|_{\lambda=0} = \log\min\delta_1 \\ Y &= y(\lambda)|_{\lambda\to\infty} = \log\min\delta_2. \end{aligned} \tag{14}$$

A suitable choice of λ then corresponds to the point closest to (X, Y). Figure 1 is a schematic plot of this: the dashed line is an (x, y)-plot for a dataset with two well compatible data sources, while the dot-dash line portrays a case with some apparent mutual discrepancies.

The parameter vector P_0

$$P_0 = \arg\min_P \left([\log\delta_1(P) - X]^2 + [\log\delta_2(P) - Y]^2 \right) \tag{15}$$

is called the *maximum compatibility estimate* (MCE). The *maximum compatibility weight* (MCW) λ_0 is given by

$$\lambda_0 = \arg\min_\lambda \left([x(\lambda) - X]^2 + [y(\lambda) - Y]^2 \right). \tag{16}$$

We note that, in this formalism, P_0 can be found directly as a solution of an optimization problem in the usual manner, without having to determine λ_0. It is, however, useful to make the plot with different values of λ to see how well the data modalities are compatible with each other in general (see Fig. 1 and the discussion in K11).

The above is straightforward to generalize to n functions δ_i and $n - 1$ parameters λ_i describing the position on an $n - 1$-dimensional hypersurface. The MCE is

$$P_0 = \arg\min \sum_{i=1}^{n} \left[\log\frac{\delta_i(P)}{\delta_{i0}}\right]^2, \quad \delta_{i0} := \min\delta_i(P), \tag{17}$$

and the MCW is, with $\lambda \in \mathbb{R}^{n-1}$,

$$\lambda_0 = \arg\min \sum_{i=1}^{n} \left[\log\frac{\hat\delta_{i,\rm tot}(\lambda)}{\delta_{i0}}\right]^2, \ \hat\delta_{i,\rm tot}(\lambda) := \{\delta_i \,|\min\delta_{\rm tot}; \lambda\}. \tag{18}$$

5. Examples: Kleopatra and Hermione

As an example of our shape representation and the inversion process, we consider two asteroids with complicated shapes: (216) Kleopatra and (121) Hermione. For the general goodness-of-fit measure, we choose

$$\chi^2 = \chi^2_{\rm lc} + \lambda_1\chi^2_{\rm pc} + \lambda_2\chi^2_{\rm sc} + \lambda_3\eta + \lambda_4\gamma, \tag{19}$$

where $\chi^2_{\rm lc}$, $\chi^2_{\rm pc}$, and $\chi^2_{\rm sc}$ are the fits obtained from the lightcurves, profile contours, and S-curves, respectively. Optimal weight coefficients λ_i can be determined using the maximum compatibility procedure described above. For smoothness and to keep the procedure stable and ensure convergence, we use the two regularization functions η and γ discussed above. We can also use physical constraints: the function ϕ of Eq. (4) and one that strives to align the principal axis of the maximum moment of inertia with the rotation axis of the object (K11). However, for these two asteroids, these regularization measures are apparently not required: the inertia tilt is less than 5° and the average gravitational slope is small for all shape versions obtained.

In addition to the shape parameters $\{a_{lm}\}$, $\{b_{lm}\}$, $\{c_{lm}\}$, the spin direction angles β, λ, and the rotation period P, we also determine optimal offset parameters for each profile contour and S-curve. The parameters minimizing Eq. (19) are found using the Levenberg-Marquardt optimization algorithm as in Kaasalainen et al. (2001). The reconstructed shape is no longer necessarily unique since it is a compromise between several data sources and regularization functions. However, even if the depiction of fine detail varies among the solutions, the overall shape is usually relatively stable, regardless of the weighting between the data sources. The truncation point of the spherical harmonics series reflects this level of resolution.

Our algorithm is implemented in MATLAB and C. The computational performance is strongly enhanced by CUDA-enabled programming of the graphics processing unit (GPU). This is a general feature of most algorithms dealing with the computational problems of generalized projections because they are highly parallelizable due to the discretization of the surface by

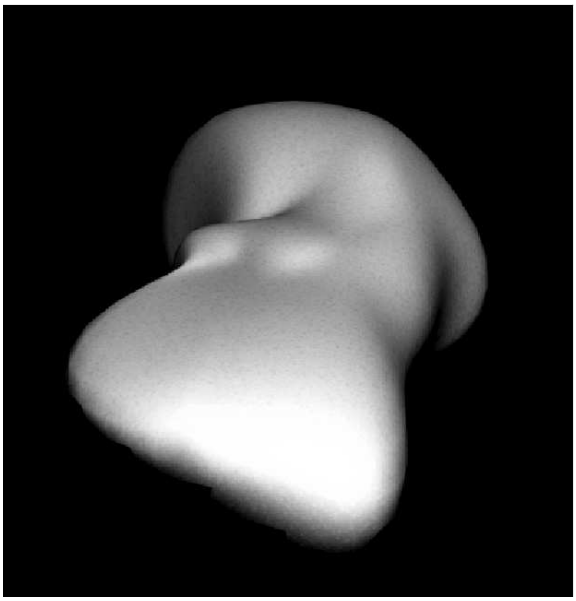

Fig. 2. Kleopatra reconstructed from lightcurves, AO, and interferometric data.

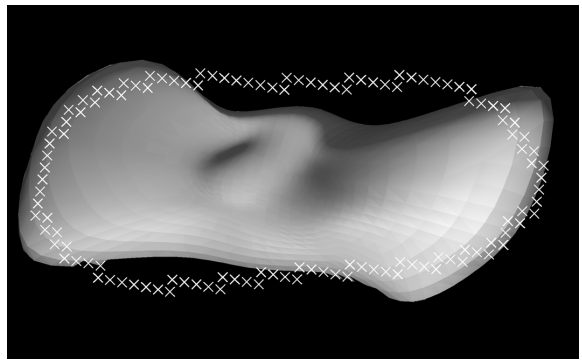

Fig. 3. An adaptive optics contour (white crosses) with systematic errors.

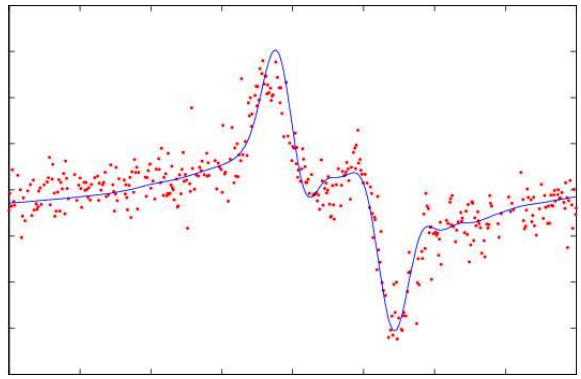

Fig. 4. A typical HST/FGS S-curve fitted by the Kleopatra model.

facets. The GPU-version is over two orders of magnitude faster than running the same code in CPU-only mode, so its use is strongly recommended. An alternative approach is grid computation. With GPU programming, the inversion result is typically obtained in less than a minute, and with moderately sized datasets in seconds.

For the asteroid Kleopatra, we used 46 lightcurves, 18 profile contours from adaptive optics images (Descamps et al. 2011), and 30 interferometric HST/FGS observations (Hestroffer et al. 2002). Interestingly enough, shape solutions obtained from the lightcurves and profile contours alone show almost none of the bifurcated structure attributed to the asteroid (Ostro et al. 2001). This is mostly due to the limited observation geometries and inaccuracies in the data. Thus the bifurcation evident in the full LC+AO+HST model of Fig. 2 is almost exclusively based on HST/FGS data. The model fits the dataset better than the radar model (see the comparison in Descamps et al. 2011). It has a bifurcated structure in common with the radar model, but the details of the two models are different.

An interesting feature is that the datasets from the different modalities are not very compatible with each other. Using all the data sources with the maximum compatibility estimate yields a compromise that clearly fits none of the single-source datasets as well as a single-source model would. This is a typical signature of systematic errors in data (cf. Fig. 3) and/or the model used in inversion (see the discussion in K11). Nevertheless, such erroneous data cannot always be discarded. For example, AO contours such as that in Fig. 3 do stabilize the result as they contain important information on the size and orientation. The radar data should be included in the complete dataset for a more refined model, but even then the current datasets from different sources are likely to be somewhat at odds with each other. However, this is perhaps not so atypical when the data are acquired by instruments working at their resolution limits.

The rotational parameters for our solution are $P = 5.38528 \pm 0.00001$ h, $\beta = +21°$, and $\lambda = 73°, \pm 8°$ of arc, close to (and halfway between) the ones presented in Ostro et al. (2001) and Descamps et al. (2011). Assuming a homogeneous density, the mean gravitational slope is 15°, indicating that the solution is physically feasible. Sample HST/FGS and AO fits are shown in Figs. 4 (best revealing the bifurcated structure) and 5.

Using the radar-based model, we simulated data with the same observing geometries as in our real dataset, and the resulting model, compared with the original one, is shown in Fig. 6. The spherical harmonics series were truncated at $l = 6$. This demonstrates that our octantoid model is powerful enough to represent complicated non-starlike shapes, and that the dataset should facilitate the construction of a reliable model if there were no systematic and/or modelling errors. The model is insensitive to typical random noise in the data sources. (Note that our original and inversion models are entirely different in their surface representations, so this result is not overoptimistic due to "inverse crime".) As it is, the jury is still out: all models and data sources of Kleopatra are somewhat discrepant with each other, so only additional disk-resolved data will help us to construct a reliable model.

For a quick estimate of which features in our model are due to the data and which are mostly the result of regularization and parametrization, we use the following greatly simplified but illustrative approach. A vertex (or a set of nearby vertices) is sequentially displaced in the normal direction, and the model fit to the data is computed. If the fit remains essentially unchanged, the facets surrounding the vertex are coloured white (we use a black-and-white classification for clarity). This method mostly

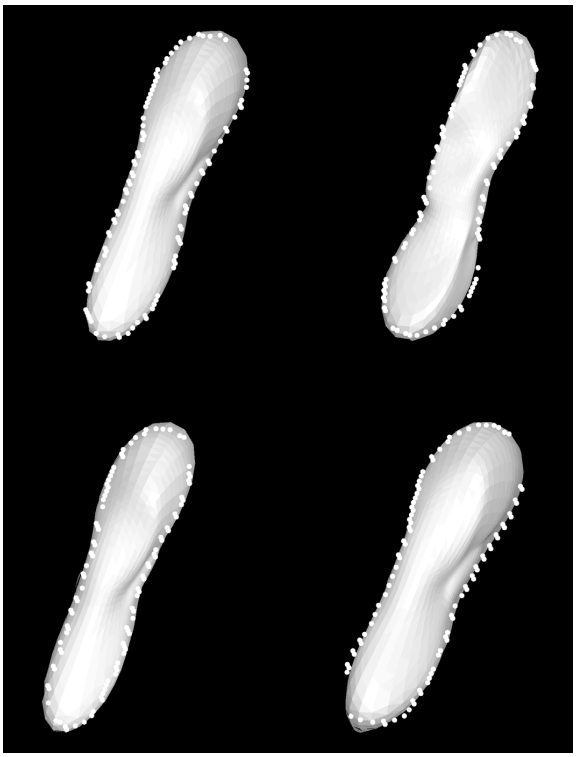

Fig. 5. Sample fits of the reconstructed Kleopatra model to the AO data.

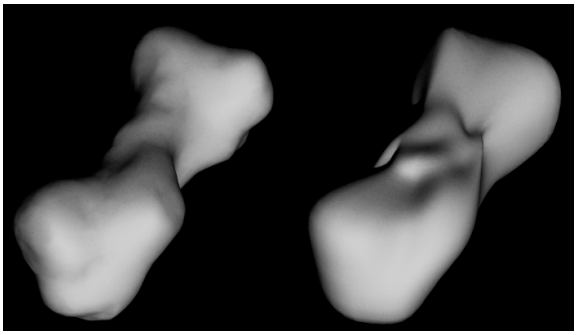

Fig. 6. A radar-based test model (*left*) and its reconstruction (*right*) from simulated Kleopatra data.

reveals the effect of AO contours and their aspect coverage: the white areas are poorly constrained by the disk-resolved data. Figure 7 confirms that we do not have enough data for a reliable reconstruction of all the features. Most of the purported details in the model are due to LC and HST data, and the AO geometries are limited in addition to the systematic error due to fuzzy images, poor weather conditions, etc. AO contours can usually be extracted more reliably than here (cf. Carry et al. 2010). We emphasize that, in multimodal inverse problems, the whole is indeed more than the sum of its parts: even a limited coverage of the surface by AO contours (or HST/FGS measurements) constrains the model details from photometry considerably more than if lightcurves were used alone. In this sense, Fig. 7 can be

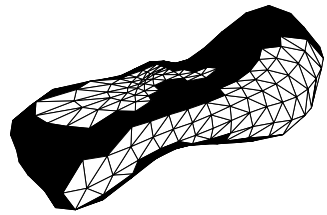

Fig. 7. Uncertain regions (white) of the Kleopatra reconstruction.

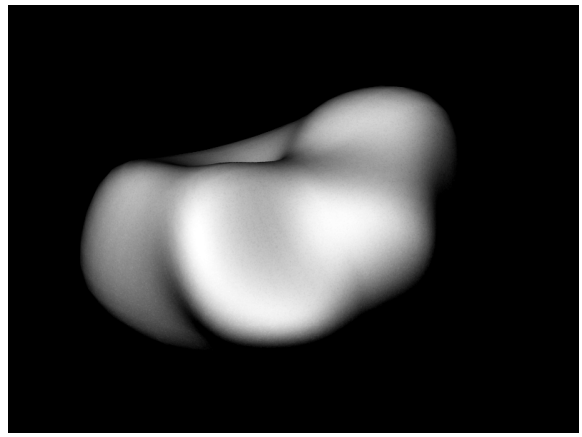

Fig. 8. Hermione reconstructed from lightcurves and AO data.

compared with the plots in Keller et al. (2010) and Carry et al. (2012) that portray parts of Steins and Lutetia in different colours corresponding to the datasets used. We will investigate issues related to error analysis in more detail in future work.

For the asteroid Hermione, we used 41 lightcurves and 6 profile contours (the same dataset as in Descamps et al. 2009). Only one of the profile contours seems to display bifurcation-like features. As can be seen from Figs. 8 and 9, the apparent bifurcation in the AO image can, in fact, be explained by a large indentation on the asteroid's surface, and this is (for the given dataset) a more probable solution than actual bifurcated features. The rotational parameters for our solution are $P = 5.55088 \pm 0.00001$ h, $\beta = +14°$, and $\lambda = 4°, \pm 6°$ of arc, which are virtually the same as in Descamps et al. (2009). The shape result is also essentially the same as in Descamps et al. (2009), but the octantoid representation helps to resolve the valley-type concavity and explains the AO contours better than a starlike parametrization. The smoothness regularization level required to explain the contours typically causes obvious artificial details in other parts of the surface as can be seen in Fig. 9. For a more refined version of the model, these can be smoothed out locally.

6. Tailoring the procedure to flyby missions

6.1. Modelling the dark side

Asteroid flybys by space probes form an important class of dataset combination. During a flyby, only about half of the asteroid's surface is usually seen (here denoted by $\mathcal{S}$) as the other half remains in darkness. To complete a model of the whole surface, we must use other data to reconstruct the unseen part $\mathcal{U}$, and in this process the probe-based model of $\mathcal{S}$ is important in

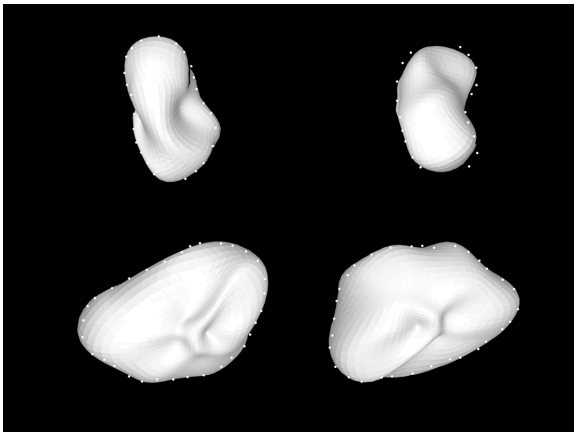

Fig. 9. Hermione model fits to the AO contours (white dots). The ridge-like structure visible in the two lower images is an artifact of the chosen smoothness level.

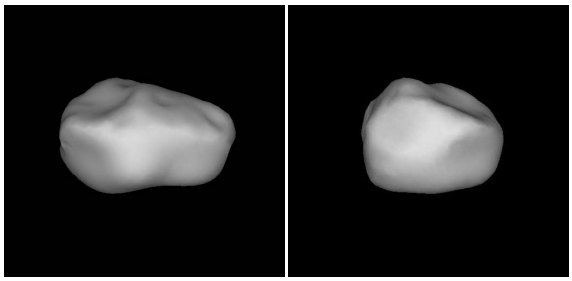

Fig. 10. Equatorial views of Lutetia reconstructed from space probe (upper part) and ground-based data (lower part).

constraining the possible solutions for $\mathcal{U}$. Because of this, $\mathcal{U}$, though never directly seen, can be reconstructed in more detail than in the usual case of ground-based observations only. We remark that this setup is rather different from that in Simonelli et al. (1994), where some minor parts of the probe-based model of the asteroid Gaspra were refined using lightcurve data. Here we consider a problem in which there is no probe-based model for a large portion of the surface at all.

The reconstruction procedure described here was successfully used in the flybys of the Rosetta probe past the asteroids Steins (Keller et al. 2010) and Lutetia (Sierks et al. 2011), and can be used in any flyby missions. Sample views of the Lutetia model are shown in Fig. 10; a more detailed description of the model is given in Carry et al. (2012) and Jorda et al. (in prep.).

Our problem of reconstructing the body $\mathcal{B}$ is of the form

$$\mathcal{B} = \mathcal{S}(D_\mathrm{p}) + \mathcal{U}(\mathcal{S}; D_\mathrm{o}), \tag{20}$$

where D_p are space-probe image and position data, and D_o are other data: ground-based observations and typically lightcurves measured by the probe prior to the flyby.

We define two terms necessary for the reconstruction algorithm. By the *limb boundary* $\mathcal{L}(\omega)$ we mean, in a polyhedral representation of the surface, that an edge of $\mathcal{L}(\omega)$ is any edge common to two facets with $\omega \cdot \nu$ of opposite signs, when ω is the projection direction and ν the outward normal of a facet. By the *envelope*, we mean the boundary of the set of those points in space (in the asteroid's frame of reference) that can be in the asteroid without contradicting the spacecraft images; i.e., points that would not appear as protrusions outside the limb boundaries or inside the shadowed regions in the images. The envelope is not necessarily a closed surface. More exactly, the envelope is the intersection of the cylinder continuations (see K11) of all the projection boundaries $\partial\mathcal{P}$ formed by the outermost projections of $\mathcal{L}(\omega)$ of $\mathcal{A}_+(\omega_0, \omega)$, in the sense of Sect. 3.1 (ω is the direction of the spacecraft seen from the asteroid), and those of $\mathcal{L}(\omega_0)$ of $\mathcal{A}_+(\omega_0, \omega)$. When $\omega_0 \neq \omega$, $\partial\mathcal{P}$ are not closed curves, but they can be completed as closed ones by assuming some maximal limb projections for the target in the shadowed areas. In other words, the envelope is made closed by making physical assumptions of the maximal size of the object in the regions where the envelope is not determined by the spacecraft images. For starlike bodies, we can denote the envelope by the function $\mathrm{env}(\theta, \varphi)$, where (θ, φ) are spherical coordinates.

The flyby reconstruction procedure, given the reconstruction of $\mathcal{S}(D_\mathrm{p})$ by standard procedures (Capanna et al., in prep.), is a modification of the general multimodal case. Here we assume a starlike body for clarity; i.e., each vertex can be described by its radius $r(\theta, \varphi)$ in the direction (θ, φ) (measured from some centre inside the body). We note that, in this procedure, the part $\mathcal{S}$ is assumed to be exact, i.e., fully consistent with the spacecraft images. Thus the images themselves need not be used in this approach; we only need the directions ω_0 and ω for each flyby image if the step 2(b) below is used (these are known because the shape part $\mathcal{S}$ is known). The algorithm is as follows:

1. Fix the flyby-determined vertices of $\mathcal{S}(D_\mathrm{p})$, and choose the directions (θ_i, φ_i), $i = 1, \ldots, N$ for the adjustable vertices of the surface part $\mathcal{U}$; these can be picked with some tessellation scheme, or they follow as by-products of the determination of $\mathcal{S}$. A practical scheme is to represent the adjustable vertices by the positive-valued exponential spherical harmonics series

$$r(\theta, \varphi) = \exp\Big[\sum_{lm} c_{lm} Y_l^m(\theta, \varphi)\Big], \tag{21}$$

   but the radii can be taken as separate parameters as well. The series representation provides a smoothing and regularizing element, and reduces the number of parameters. The resolution level expected for $\mathcal{U}$ can typically be represented by a series with $6 \leq l_\mathrm{max} \leq 8$. The procedure and regularization functions for minimizing χ^2 are as described in the general cases above and in K11. The initial guesses for c_{lm} can be obtained, e.g., from an ellipsoid best matching $\mathcal{S}$ or they can be some plausible values resulting as by-products of the flyby-determination of $\mathcal{S}$. The latter are useful as they initially join $\mathcal{S}$ and $\mathcal{U}$ smoothly together. The flyby-determination usually also fixes the pole direction of the object since its orientation (and hence the zero-time and zero-rotation phase) at some epoch during the flyby is fixed. This defines the asterocentric frame of reference. The rotation period is usually left adjustable as the long time span of other data constrains it more accurately than the flyby data.
2. (a) The $\mathcal{S}$ model may provide an envelope $\mathrm{env}(\theta, \varphi)$ as well. The radii of $\mathcal{U}$ can be explicitly constrained to lie within the envelope with

$$r(\theta, \varphi) = \mathrm{env}(\theta, \varphi)\, \frac{\mathrm{e}^{a(\theta,\varphi)}}{1 + \mathrm{e}^{a(\theta,\varphi)}}, \tag{22}$$

   where $a(\theta, \varphi)$ is a spherical harmonics series (or a parameter for an independent vertex). In our experience,

however, this often weakens the convergence of the algorithm. In such cases, or if no envelope is available, it is best to use the more approximate but also more robust version (b) below.

(b) Constraints equivalent to an envelope can be enforced by vertex retraction using the projection directions of the flyby images (for a detailed description of the profiles of polyhedra and the terms used below, see K11). In the following, the projections are checked in all the directions of the flyby images, and the direction Ω is, in turn, both $\Omega = \omega$ and $\Omega = \omega_0$ for each image (this takes care of both the shadow and limb boundaries seen from the spacecraft).
For each $\mathcal{A}_+$ vertex i of $\mathcal{U}$, check whether its projected radius $p(\alpha_i;\Omega)$ (from the origin at the direction α_i in the projection plane) is larger than the radius $p_{\mathcal{S}}(\alpha_i;\Omega)$ of an intersection of the radius line with an $\mathcal{L}(\Omega)$ edge of $\mathcal{S}$ in $\mathcal{A}_+(\omega_0,\omega)$. If yes, retract according to the nearest smaller value $p_{\mathcal{S}}(\alpha_i;\Omega)$ of projected radius:

$$r(\theta_i,\varphi_i)_{\rm new} = \frac{p_{\mathcal{S}}(\alpha_i;\Omega)}{p(\alpha_i;\Omega)} r(\theta_i,\varphi_i). \tag{23}$$

The retraction produces a shape that is consistent with probe images, i.e., is within the shape envelope, while the effect of the retraction on χ^2 is usually negligible since few model vertices from step 1 are expected to lie outside the envelope if the data are good (and, e.g., inertia tensor regularization is used).

3. For the vertices of $\mathcal{U}$ within some angular distance δ on S^2 from the $\mathcal{S}/\mathcal{U}$ boundary, use the neighbouring radii (again within some suitable distance) for averaging $r_i \rightarrow \langle r\rangle$ to smooth out any unrealistic indentations that may occur near the $\mathcal{S}/\mathcal{U}$ boundary. Bulges at the boundary are ruled out by step 2 at the start, but after averaging go back to retraction (step 2) if necessary. Again, the effect of this smoothing on χ^2 is usually negligible.
4. The result obtained is a set of vertices of $\mathcal{S}$ and $\mathcal{U}$ joined smoothly together. Since $\mathcal{S}$ can usually be given with a level of resolution much higher than one that would affect the model fit of the other data $D_{\rm o}$, it is computationally advantageous to use a low-resolution version of $\mathcal{S}$ in the procedure. Once $\mathcal{U}$ is determined, it can be glued to any higher-resolution version of $\mathcal{S}$ at will. Such glueing can be done without an explicit definition of the complete vertex circuits of the boundaries of $\mathcal{S}$ and $\mathcal{U}$. First create sets of $\mathcal{U}$ and $\mathcal{S}$ facet triangle edges that occur only once in their respective facet lists: these are boundary edges. Then connect each boundary vertex of one set to the nearest one of the other set. This results in triangles or (non-planar) quadrangles in the region between the boundaries, and the quadrangles can be split into triangles as desired.

6.2. Distributions of derived quantities: note on volume uncertainty

A typical quantity derived from a shape model is its volume. The uncertainty in the volume is related to the shape uncertainty somewhat in the sense of a marginal distribution, so we briefly discuss this aspect. The uncertainty estimate of the volume was, for example, important in deducing the density of the asteroid Lutetia, and confirming that it was indeed at the high end of the estimated densities of asteroids (Sierks et al. 2011). When using normal distributions for radius- or volumelike variables x here, we assume that the distributions $p(x)$ are narrow enough so that $p(x) = 0$, $x \le h$ for all practical purposes for some $h > 0$.

Consider first a sphere with the centre of $p_R(R)$ at some R_0. With $V_0 = 4\pi R_0^3/3$, we have, from $p_R(R)\,{\rm d}R = p_V(V)\,{\rm d}V$,

$$p_V(V) = \frac{1}{3}\left(\frac{3}{4\pi}\right)^{1/3} p_R\left[\left(\frac{3V}{4\pi}\right)^{1/3}\right] V^{-2/3}, \tag{24}$$

which, for a Gaussian normal distribution $p_R(R) = \mathcal{N}(R_0,\sigma)$ (here σ denotes the relative standard deviation w.r.t. R_0), is well approximated by $p_V(V) \approx \mathcal{N}(V_0, 3\sigma)$, consistent with the basic approximation from ${\rm d}V/V = 3{\rm d}R/R$ (the top of the distribution is at a slightly smaller value than V_0 due to the $V^{-2/3}$-term).

For an ellipsoid with semiaxes a, b, and c, using $V = 4\pi abc/3$, we take V to be a variable, and change $c = 3V/(4\pi ab)$ so that

$$p(a,b,c)\,{\rm d}a\,{\rm d}b\,{\rm d}c = p\left(a,b,\frac{3V}{4\pi ab}\right)\frac{3}{4\pi ab}\,{\rm d}a\,{\rm d}b\,{\rm d}V. \tag{25}$$

The marginal distribution $p(V)$ is thus given by

$$p(V) = \frac{3}{4\pi}\int\int p\left(a,b,\frac{3V}{4\pi ab}\right)\frac{1}{ab}\,{\rm d}a\,{\rm d}b. \tag{26}$$

For $a_0 = b_0 = c_0 = l$ and $p(a,b,c) = \mathcal{N}_3(l,\sigma)$, where $\mathcal{N}_3$ is a three-dimensional multivariate normal distribution with equal means and deviations, $p(V)$ is approximated by

$$p(V) \approx \mathcal{N}(V_0, 1.7\sigma), \tag{27}$$

already strongly in contrast with the spherical case and the basic approximation $\Delta V/V \approx 3\sigma$. The distribution of $p(V)$ is more concentrated because the shape of the ellipsoid can change in all semiaxis directions. If the shape stayed the same and only the size changed, $p(a,b,c)$ would only lie along a line in the (a,b,c)-space rather than sample the whole space.

For general cases, the integral is replaced by a cumulative distribution function $C(V)$ over N MCMC samples, i.e.,

$$C(V_i) = i/N, \quad V_i = V[\mathcal{S}_i(p(x))], \tag{28}$$

for $i = 1,\ldots N$, and $\mathcal{S}_i(x)$ denotes the ith randomly drawn sample from the distribution $p(x)$ of the shape parameters x, and the draws are sorted in ascending order of V_i. For numerical purposes, obtaining $p(V) = {\rm d}C(V)/{\rm d}V$ is unstable, so it is easier to work with $C(V)$ and, e.g., fit the parameters V_0 and σ_V of a normal distribution $\mathcal{N}(V_0,\sigma_V)$ to $C(V)$ using the Gaussian cumulative integral $C_{\mathcal{N}}(V;V_0,\sigma_V)$.

For a sphere with i.i.d. radii for each octant, we have $p(V) \approx \mathcal{N}(V_0,\sigma_V)$ with $\sigma_V \approx \sigma_R$, while a further division into four parts of equal solid angles for each octant already yields $\sigma_V \approx 0.5\,\sigma_R$. A needle-cushionlike division into infinitely many parts thus yields $p(V) = \delta(V - V_0)$ (regardless of σ), i.e., a step function for $C(V)$. This emphasizes that, if we have a multiparameter shape model with polyhedral radii r_i, the relative volume uncertainty can be smaller than the relative radius uncertainty: $0 < \Delta V/V < \Delta r/\langle r\rangle$ even when r_i are correlated by a smoothness constraint. The fluctuations of r effectively cancel out most of each other as far as the total volume is concerned. As a rule of thumb, the approximation $\Delta V/V \approx \Delta r/\langle r\rangle$ is more appropriate than $3\Delta r/\langle r\rangle$ when the shape uncertainty is not dominated by a scale factor for size (cf. Carry et al. 2012).

7. Discussion

We have presented methods for expanding the sets of data sources and surface types in multimodal asteroid modelling. The most plausible compromise between the datasets is given by the maximum compatibility estimate. We emphasize the mutual "synergy" effect of multimodal data in constraining shape details. This is particularly striking when partial flyby data are available. As discussed in Sierks et al. (2011) and Carry et al. (2012), the fixed flyby-determined portion of the surface greatly constrains the allowed solutions for the dark side $\mathcal{U}$ even when its data are disk-integrated only. Thus the solution based on photometry is considerably more restricted than if photometry were used alone. This allows the construction of large-scale nonconvex features on the dark side. The same phenomenon can be seen in the cases where good AO contours are combined with photometry. The power of this approach is demonstrated in Carry et al. (2012), where the match of the ground-based Lutetia model (published prior to the flyby) to the flyby images was shown to be remarkably good. What is more, the ground-based Lutetia data were not special in any way: the AO contours contained several systematic errors, and their aspect coverage of the target was not especially good. Of the examples presented here, the quality of the Hermione dataset is roughly similar to that of Lutetia. The octantoid parametrization allows the modelling of non-starlike features, which in the case of Hermione best explains the kidney-bean shaped AO images as views of the shadow of a large indentation. Kleopatra, on the other hand, turned out to be something of a riddle. In spite of the many available data modes, a valid model cannot be constructed yet as the data (plus the model from radar, the fourth source) are mutually inconsistent. Disk-resolved data (with fewer systematic errors) at complementary observing geometries are needed to establish a reliable multimodal reconstruction.

Reliability estimates are important in any schemes that produce detailed asteroid shape models from indirect data of various types and quality. Assessing the reliability of depicted surface features is not a simple task as the uncertainties are typically dominated by systematic errors, "unknown unknowns" rather than "known unknowns" in both data and the model setup. This makes practically all standard procedures for uncertainty evaluation (such as MCMC) more or less deficient and overoptimistic in our case. We will study this problem and develop estimation procedures in the future versions of the modelling software package described below. A further aspect of this is observation/experiment design. Using reliability estimates, we can predict how observations made at various geometries can improve the result. This should improve the time efficiency and planning of observation campaigns.

Our inversion procedures are incorporated in a continuously updated software package that is downloadable at the DAMIT asteroid modelling website[2]. Asteroid models and the data used in constructing them are available there as well (Ďurech et al. 2010). GPU programming typically speeds up the computation by a factor of more than one hundred. This makes the inversion very fast and allows, e.g., time-efficient Monte Carlo sampling. The software will be described in a separate paper (Ďurech et al., in prep.). The first public version of the package contains procedures for lightcurve inversion; the second one will provide the routines for analysing lightcurves, occultation timings, adaptive-optics (or other) images, and interferometric data simultaneously. Radar and thermal infrared data will be added to the source options in a forthcoming version. We will also study the use of level sets and control point sets in analysing bifurcated and other complex shape structures in a general manner. One of the advantages of level sets is their ability to provide a continuous sequence of models from a connected bifurcated shape to a separated binary one without having to change the model setup.

Acknowledgements. This work was supported by the Academy of Finland project "Modelling and applications of stochastic and regular surfaces in inverse problems". We thank Franck Marchis, Daniel Hestroffer, and Pascal Descamps for the datasets of Hermione and Kleopatra, and Josef Ďurech and Benoit Carry for discussions and comments.

References

Carry, B., Dumas, C., Kaasalainen, M., et al. 2010, Icarus, 205, 460
Carry, B., Kaasalainen, M., Merline, W., et al. 2012, Planet. Space Sci., 60, 200
Descamps, P., Marchis, F., Ďurech, J., et al. 2009, Icarus, 203, 88
Descamps, P., Marchis, F., Berthier, J., et al. 2011, Icarus, 211, 1022
Ďurech, J., & Kaasalainen, M. 2003, A&A, 404, 709
Ďurech, J., Grav, T., Jedicke, R., et al. 2005, Earth Moon Planets, 97, 179
Ďurech, J., Sidorin, V., & Kaasalainen, M. 2010, A&A, 513, A46
Ďurech, J., Kaasalainen, M., Herald, D., et al. 2011, Icarus, 214, 652
Hestroffer, D., Tanga, P., Cellino, A., et al. 2002, A&A, 391, 1123
Kaasalainen, M. 2001, A&A, 376, 302
Kaasalainen, M. 2004, A&A, 422, L39
Kaasalainen, M. 2011, Inv. Prob. Imag., 5, 37 (K11)
Kaasalainen, M., & Lamberg, L. 2006, Inv. Prob., 22, 749 (KL06)
Kaasalainen, M., Lamberg, L., Lumme, K., & Bowell, E. 1992, A&A, 259, 318
Kaasalainen, M., Torppa, J., & Muinonen, K. 2001, Icarus, 153, 37
Kaasalainen, M., Ďurech, J., Warner, B., et al. 2007, Nature, 446, 420
Keller, H. U., Barbieri, C., Koschny, D., et al. 2010, Science, 327, 190
Nathues, A., Mottola, S., Kaasalainen, M., & Neukum, G. 2005, Icarus, 173, 108
Magri, C., Howell, E., Nolan, M., et al. 2011, Icarus, 214, 210
Ostro, S. J., Hudson, R. S., Nolan, M., et al. 2000, Science, 288, 836
Ostro, S. J., Hudson, R. S., Benner, L., et al. 2002, Asteroids III, eds. W. Bottke, A. Cellino, P. Paolicchi, & R. Binzel, 151
Scheirich, P., Ďurech, J., Pravec, P., et al. 2010, Met. Plan. Sci., 4, 1804
Sierks, H., Lamy, P., Barbieri, C., et al. 2011, Science, 334, 487
Simonelli, D., Veverka, J., Thomas, P., & Helfenstein, P. 1994, Icarus, 114, 387
Werner, R. 1994, Cel. Mech. Dyn. Ast., 59, 253.
Zacharopoulos, A. D., Arridge, S. R., Dorn, O., et al. 2006, Inv. Prob., 22, 1509

[2] http://astro.troja.mff.cuni.cz/projects/asteroids3D/web.php

Publication II

Viikinkoski M. and Kaasalainen M., “Shape reconstruction from images: Pixel fields and Fourier transform,” *Inverse Problems and Imaging* 8, no. 3(2014) 885-900

Reproduced with permission from Inverse Problems and Imaging, ©AIMS 2014

Inverse Problems and Imaging
Volume 8, No. 3, 2014, 885–900
doi:10.3934/ipi.2014.8.885

SHAPE RECONSTRUCTION FROM IMAGES: PIXEL FIELDS AND FOURIER TRANSFORM

Matti Viikinkoski and Mikko Kaasalainen

Department of Mathematics
Tampere University of Technology
PO Box 553, 33101 Tampere, Finland

(Communicated by Margaret Cheney)

Abstract. We discuss shape reconstruction methods for data presented in various image spaces. We demonstrate the usefulness of the Fourier transform in transferring image data and shape model projections to a domain more suitable for shape inversion. Using boundary contours in images to represent minimal information, we present uniqueness results for shapes recoverable from interferometric and range-Doppler data. We present applications of our methods to adaptive optics, interferometry, and range-Doppler images.

1. **Introduction.** It is an early lesson in mathematics that many problems are considerably easier to handle by transferring the variables and functions to another domain via, e.g., the Fourier transform (FT). Here we show that this principle can be used in reconstructing the shape (and dynamics) of a body from data presented in various image spaces. Shape reconstruction can actually be seen as a form of model-based image processing, or de-noising with strong prior constraints: from noisy images, we determine a model of the object seen in them, and this model can be used to reconstruct the original images (compare Figs. 1 and 2). Such an interpretation does not even necessitate a unique object model (for viewing geometries other than those of the original images).

Our approach is applicable to any shape modelling from images; here we use images obtained with astronomical instruments as our application examples. Image-resolved astronomical data are usually presented as pixel image fields defined by generalized projection operators [7]. Such images are obtained by, e.g., adaptive optics or radar.

The viability of shape reconstruction from the boundary curves of object projections in optical images was investigated in [8, 9]. For completeness, we show below that the shape can also be uniquely defined from the boundary contours of its range-Doppler images under some mild conditions, and that the uniqueness results of optical images can be extended to interferometric images. The boundary extraction methods have the advantage that they are independent of both the scattering model of the target and the often erroneous interior pixel intensity values. On the other hand, they can be problematic as the image boundaries are not always clearly defined due to blurring and other imaging errors.

2010 *Mathematics Subject Classification.* 68U05, 68T45, 65D18, 52B10, 49N45, 65J22, 85-08.
Key words and phrases. Inverse problems, three-dimensional polytopes, generalized projections, image analysis, adaptive optics, interferometry, radar.

 ©2014 American Institute of Mathematical Sciences

An efficient way to use pixel values is to make a continuous (complex-valued) image function of a pixel field or a model projection via the Fourier transform. As we show below, this explicitly retains most of the weight on the image boundary curves as well. We present analytical Fourier transforms of projected images in Sect. 2. We describe the FT reconstruction method in Sect. 3, and discuss its advantages. Applications in adaptive optics, interferometry, and range-Doppler radar (with uniqueness results) are discussed in Sect. 4, and we sum up in Sect. 5.

2. **Fourier transforms of images of polyhedral models.** Let us first consider the usual approach of fitting the pixel values directly without FT. The model representation is a polyhedron that is projected onto some projection plane $(\xi, \eta) \in \mathbb{R}^2$ via a linear transformation [7, 8]. Let $\mathcal{P} : \mathbb{R}^3 \to \mathbb{R}^2$ be the operator for this linear mapping. Then the projection $\mathcal{P}T_i$ of each facet T_i is assigned a brightness factor B_i depending on the visibility, attitude, and surface scattering or radiation flux model of the facet. The scattering model $S(\mu\,\mu_0, \alpha)$ is typically dependent on the cosines μ and μ_0 between the surface normal and, respectively, the viewing and illumination directions, and on the angle α between the latter two [7]. Since the projection cosine μ is traditionally taken as a fixed factor in S, we write

$$B_i = \begin{cases} S_i(\mu, \mu_0, \alpha)/\mu, & \mu\mu_0 > 0, \\ 0, & \text{otherwise.} \end{cases}$$

As far as their role in B_i is concerned, models of thermal surface radiation flux are essentially similar to the scattering models, except that they have a time-lag component as discussed below.

For each point on the projection, we assign a factor $I(\xi, \eta) \in \{0, 1\}$, a piecewise constant integer function encoding the visibility and illumination (VI) condition of the point (ξ, η). This constitutes the generalized projection or image mapping. In principle, one could determine the exact projection polygons inside which $I(\xi, \eta) = 1$ by considering all intersections due to occluding facets [8]. In practice, this is unnecessarily laborious, so we use the separate projections of the original polyhedron facets. Each facet is checked for VI as a whole by ray-tracing (using the centroid of the facet), and the level of resolution can be controlled at will by dividing a facet into subfacets; for example, the radar imaging process usually requires greater accuracy than the thermal infrared. Thus we approximate, for each facet T_i,

$$I_i = \begin{cases} 1, & i \text{ is VI}, \\ 0, & \text{otherwise.} \end{cases}$$

Two polygons in a plane (a facet projection of a polyhedral shape model and a pixel frame) overlap, if any of their boundary lines intersect, or if any vertex of either is inside the other. For such cases, one finds all the intersection points, if any, and thus determines the boundary lines of the overlap polygon. The sum of the areas of all the overlap polygons inside a pixel frame, each multiplied by the factors $B_j\, I_j$ of the corresponding facet, then determine the model intensity P_i^{mod} of the pixel. The derivatives w.r.t. the vertex coordinates of the polyhedron, and hence the parameter gradients for efficient optimization, follow directly from this. We find the solution that minimizes $\|P^{\mathrm{obs}} - P^{\mathrm{mod}}\|$, where $P^{\mathrm{obs/mod}}$ are the vectors that contain the observed and modelled pixel intensities. Since each feasible facet-pixel overlap pair must be checked, this is essentially an N^2 process, although the number of function-value computations is smaller than in the N^2 process of the FT sampling below.

We remark that it is possible just to sample the B_i at various points on the surface (or the image plane), and then use these samples to produce the model pixel intensities. However, though fast in computing the forward problem, this is not efficient in shape reconstruction. This is because now there are no analytical partial derivatives with respect to parameters only related to the position in the image plane (such as model size and offset factors, unless there is a significant point-spread function), and other shape parameters have derivatives only through the orientation of the local model surface patches.

Consider now doing the computations in the Fourier-transformed domain, the plane $(u, v) \in \mathbb{R}^2$. For practical purposes, we define our (two-dimensional) Fourier transform of some function $f(\xi, \eta)$ somewhat differently from the standard form:

$$\mathcal{F}(u, v) := \int_{\mathbb{R}^2} f(\xi, \eta) e^{-2\pi\imath(u\xi+v\eta)} d\xi d\eta. \tag{1}$$

The point here is that any integral transform that has the same basic properties as FT is suitable for our purposes, so constants and normalizations used in the definition are irrelevant. Indeed, some completely different transforms may be just as good, but we have found the FT approach to converge very well. Also, interferometric data are typically samples of a Fourier transform, given in the frequency (u, v)-plane, so the FT approach is ideal for such cases.

Letting $\mathcal{T}$ be the set of facets forming the polyhedron, the transform integral can be written, by Green's theorem, as

(2)

$$\begin{aligned}\mathcal{F}(u, v) &= \sum_{T_i \in \mathcal{T}} \int\int_{\mathcal{P}T_i} B_i \, I(\xi, \eta) e^{-2\pi\imath(u\xi+v\eta)} \, d\xi d\eta \\ &= \sum_{T_i \in \mathcal{T}} B_i \sum_j \frac{1}{2\pi\imath} \int_{\Gamma_{ij}} \left(\frac{v}{u^2+v^2} e^{-2\pi\imath(u\xi+v\eta)} \, d\xi - \frac{u}{u^2+v^2} e^{-2\pi\imath(u\xi+v\eta)} \, d\eta \right) \\ &:= \sum_i B_i \sum_j \mathcal{I}_{ij}(u, v),\end{aligned}$$

where Γ_{ij} are the boundary line segments defining the VI part of the projected facet $\mathcal{P}T_i$, oriented counterclockwise. In practice, these are the edges of entire projected facets (or subfacets) included in the sum depending on their I_i. The facet factor B_i can also include the intrinsic lightness (albedo) of the local surface, and this can be left as a a free parameter (or a function over the surface). For $(u, v) = (0, 0)$, the Fourier transform is the total brightness of the image:

$$\mathcal{F}(0, 0) = \sum_{T_i \in \mathcal{T}} \int\int_{\mathcal{P}T_i} B_i \, I(\xi, \eta) \, d\xi d\eta = \sum_i B_i \sum_j \int_{\Gamma_{ij}} \xi \, d\eta, \tag{3}$$

i.e., the last sum is the area of the VI part of $\mathcal{P}T_i$.

For a line segment Γ_{ij} with end points (a, b) and (c, d), $\mathcal{I}_{ij}(u, v)$ can be written in a closed form by substituting the line equations so that we have

$$\mathcal{I}_{ij}(u, v) = \frac{1}{4\pi^2(u^2+v^2)} \frac{(b-d)u - (a-c)v}{(a-c)u + (b-d)v} (e^{-2\pi\imath(au+bv)} - e^{-2\pi\imath(cu+dv)}). \tag{4}$$

The summation over $\mathcal{I}_{ij}(u, v)$ can be reordered and speeded up by noting that each polygon edge in the interior is shared by two polygons, so a new factor $\tilde{B}$ can be taken to be the difference between the two B_i, and the edge term is computed only once. Note that this explicitly shows why most of the information in the image is

indeed from the limb and shadow boundary curves discussed in [8, 9]. The values of $\tilde{B}$ for interior edges are usually close to zero (indeed, they vanish for the geometric scattering $B_i = const.$), so most of the weight is on the boundary edges. From the above expression, it is obvious that the integral has continuous partial derivatives with respect to the projected vertices, which are linear combinations of the original vertices of the facet. Thus the Fourier transform has continuous partial derivatives with respect to the facet vertices.

3. **Fourier transform method for model reconstruction.** Our approach is largely independent of shape representations. For their effectiveness and simplicity, we prefer *octantoids* [9]. An octantoid is a surface given by $p \in \mathbb{R}^3$ that can be parametrized in the form

$$p(\theta,\varphi) = \begin{cases} x(\theta,\varphi) = & e^{a(\theta,\varphi)} \sin\theta\cos\varphi, \\ y(\theta,\varphi) = & e^{a(\theta,\varphi)+b(\theta,\varphi)} \sin\theta\sin\varphi, \\ z(\theta,\varphi) = & e^{a(\theta,\varphi)+c(\theta,\varphi)} \cos\theta, \end{cases} \tag{5}$$

where a, b and c are conveniently expressed as linear combinations of the (real) spherical harmonic functions $Y_l^m(\theta,\varphi)$, with coefficients a_{lm}, b_{lm} and c_{lm}, respectively. Note that (θ,φ), $0 \le \theta \le \pi$, $0 \le \varphi < 2\pi$, are coordinates on the unit sphere S^2 parametrizing the surface but not describing any physical directions such as polar coordinates. As usual, the Laplace series for a, b, c are useful for keeping the number of unknowns small and the surface smooth; separate vertex parameters can be used as well, but this usually necessitates heavy regularization. The drawback of this is its globality: one might want less smoothness regularization in some regions than in others. When more local control is desired (e.g., a feature clearly visible in fly-by images or in radar), the representation (5) may be expanded with spherical splines or spherical wavelets to provide local detail without affecting the global shape.

The representation (5) is convenient for asteroid shapes, as asteroids are often geometrically starlike or close to it. This indicates that we can use the deviation from starlikeness as a regularization measure. For this effect, we define

$$\gamma = \sum_{l,m} l(b_{lm}^2 + c_{lm}^2). \tag{6}$$

In many cases, we can explicitly set $b = c = 0$ for starlike shapes, but it is often useful to employ γ instead as this gives more room for shape adjustment. The parametric representation (5) using a finite number of spherical harmonics is global in the sense that a change in each parameter will affect shape globally. This has a strong regulating effect, which is usually beneficial as the available data are often incomplete and noisy.

We can now write the FT reconstruction procedure as follows:

1. For each data image D_i and observation geometry $\mathcal{E}_i$, the two- dimensional Fourier transform $\mathcal{F}D_i(u,v)$ of D_i is sampled at a set of points $\{(u_{ij}, v_{ij})\}$, $j = 1 \dots N_i$, on the spatial frequency plane. For pixel images, the transform can be computed by Eq. (2) when considering each pixel as a polygon, or by using fast Fourier transform functions for chosen grid points (but the time spent for $\mathcal{F}D_i(u,v)$ is irrelevant as most of the computations are for the trial models).
2. The shape parameters a_{lm}, b_{lm}, and c_{lm} are initialized such that Eq. (5) represents a sphere approximately equal in size to the target.

3. For each observation geometry $\mathcal{E}_i$, the Fourier transform $\mathcal{F}M_i(u,v)$ of the corresponding projection image M_i of the model is calculated as described in the previous section, together with the partial derivatives of $\mathcal{F}M_i(u,v)$ with respect to the shape parameters.
4. An objective function χ^2 is formed, with the square norm of the complex-valued FT fit error:

$$\chi^2 = \sum_i \sum_{j=1}^{N_i} \left\| \mathcal{F}D_i(u_{ij}, v_{ij}) - e^{2\pi\imath(o_i^x u_{ij} + o_i^y v_{ij})} \mathcal{T}_i(u_{ij}, v_{ij}) \mathcal{F}M_i(u_{ij}, v_{ij}) \right\|^2 + \lambda\gamma^2$$

where (o_i^x, o_i^y) is the offset between the data image D_i and the model image M_i, and, by the convolution theorem, $\mathcal{T}_i$ is the Fourier transform of the point-spread function of the imaging system. The regularization term γ corresponds to Eq. (6). Additional regularization measures are also possible, e.g., local convexity, gravitational slope or the inertia tensor [8, 9]. Usually γ is the best choice, as the physical regularization methods tend to restrict the shape too severely during the initial convergence.

In addition, the intensity level of each data and model image must be normalized. Often it is enough to divide both model M_i and data image D_i by their respective mean intensities. Equivalently, writing

$$\chi^2 := \sum_{ij} \left\| \mathcal{D}_i(u_{ij}, v_{ij}) - \tilde{\mathcal{M}}_i(u_{ij}, v_{ij}) \right\|^2 + \lambda\gamma^2,$$

we have (cf. [6])

$$\chi^2_{\mathrm{rel}} = \sum_{ij} \left\| \frac{\mathcal{D}_i(u_{ij}, v_{ij})}{\langle \|D_i\| \rangle} - \frac{\tilde{\mathcal{M}}_i(u_{ij}, v_{ij})}{\langle \|\tilde{M}_i\| \rangle} \right\|^2 + \lambda\gamma^2,$$

where the mean $\langle\cdot\rangle$ is taken over $\{(u_{ij}, v_{ij})\}$, $j = 1 \dots N_i$. However, sometimes it is better to allow the intensity level of each M_i to be a free parameter and use χ^2; this is useful in the case where the mean intensity of D_i is corrupted by excessive noise in the image background (this is typical for range-Doppler images). This causes the χ^2_{rel}-based solution to have a slightly wrong size to compensate for the "diluted" normalized intensity level inside the actual object region of D_i.
5. The shape parameters a_{lm}, b_{lm} and c_{lm}, spin vector direction, and the offsets (o_i^x, o_i^y) as well as the possible intensity level factors C_i minimizing χ^2 are determined with a suitable method such as the Levenberg-Marquardt algorithm.

The crux of the idea is that the Fourier transform of the plane-projected mesh of a model polytope is simple to compute analytically, and the partial derivatives with respect to vertex coordinates exist and can be straightforwardly given in a closed form. Since $\mathcal{F}^{-1}\mathcal{F} = \mathbb{I}$, FT retains all the information in the original image. We can list some particular advantages of the FT approach:

- The FT method algorithm is simpler than direct pixel fitting, and it converges robustly
- Information at any point in the frequency plane comes from all points in the image plane, which increases robustness
- FT sampling can be used to filter the image information at different frequency (i.e., resolution) scales
- Point-spread functions can easily be taken into account

The downside of the FT method is increased computation time and complexity as we move from the sparse boundary curve to the two-dimensional Fourier transform of the projection image. For image fields with N relevant pixels, the boundary curve approach pertains to essentially $\sqrt{N}$ boundary elements and is basically an N process, whereas the FT method is N^2. In all methods, much of computing time is, of course, spent on the same ray-tracing computations. In any case, the polyhedral and Fourier computations are trivially parallel. Each facet or each point on the (u, v)-plane can be considered separately, so the computations can be implemented very effectively on a graphics processing unit.

4. **Applications.**

4.1. **Adaptive optics images.** The resolution of even the best telescopes is not limited by their optics but by the Earth's atmosphere. The incoming wavefront is distorted by the atmospheric turbulence causing speckle patterns in the image. In effect, the angular resolution of a single telescope is limited to 0.5 arcseconds, making image-resolved imaging of asteroids nearly impossible. Adaptive optics tries to correct the atmospheric distortion with a help of a computer-controlled deformable mirror. The effects of the atmosphere are mitigated by the means of a reference star. The degradation of the wavefront from a known star is analyzed, and the mirror is adjusted to counter the effect. Further, the raw image obtained this way can be post-processed with various image-processing algorithms. With adaptive optics, disk-resolved imaging with angular resolution approaching the diffraction limit becomes possible. However, the improved precision comes at a cost. The most reliable information in the adaptive optics image is the boundary curve, as the the interior contains artefacts caused by the imaging process. In addition, the boundary extraction methods will often introduce artefacts of its own, especially if the boundary pixels are fuzzy. Thus, using the image field, the boundary extraction may be bypassed altogether, and even the raw image can be used directly without separate image-processing.

As an example, we consider the large main-belt asteroid 41 Daphne. We used 14 adaptive optics images obtained from the Very Large Telescope array at ESO, with pixel size of approximately 0.01 arcseconds. This corresponds to $7 - 12$ kilometers per pixel, as the geocentric distance varies between images. Each image is transformed to the frequency plane and sampled on a rectangular grid consisting of 8064 points. In addition, we included several lightcurves, which mostly refined the spin state solution. Interestingly enough, they had no discernible effect to the actual shape solution as the available AO images seem to constrain the shape adequately. The solution is similar to the one in [8] obtained with image boundaries. The adequacy of AO data can also be seen in the curve in [8] depicting the lightcurve fit as the weight of AO data is increased: the lightcurve fit does not decrease much along the curve.

Our model consists of a triangular mesh with 1568 facets, with vertex locations defined by 243 shape parameters. The highest degree of spherical harmonics in the reconstruction is nine. In addition to the shape parameters and the direction of the rotation axis, we also determined optimal offset parameters for each image, since the object's location on the image plane is unknown. The light-scattering model used in the reconstruction is not important since most of the information is on the boundaries. We chose the standard combination of the Lommel-Seeliger and

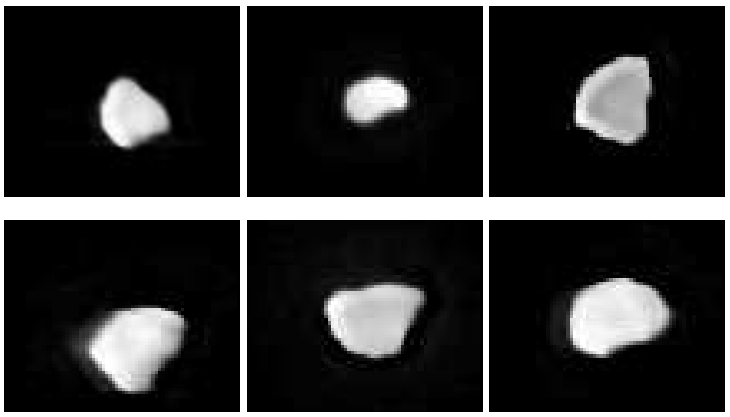

Figure 1. Examples of the adaptive optics images of the asteroid Daphne.

Lambert laws [6]:

$$B_i = C\,\mu_0^{(i)}\left(\frac{1}{\mu^{(i)}+\mu_0^{(i)}}+0.1\right),$$

where C is a free constant for each image for adjusting the intensity level of the model to match that of the data. More complicated scattering models such as Hapke can be used, but this has no effect on the result as the interiors of the object are not reliable in the images in any case. In Fig. 1 we show some of the adaptive optics images. Projections of the reconstructed model are presented in Fig. 2. It is interesting to note that the non-convex details visible in the AO images (Fig. 1) are also apparent in the reconstructed model, so the result could indeed be seen as a form of image processing as well.

4.2. **Interferometry in the thermal infrared: Heat diffusion equation and its inversion model.** The advances in ground-based thermal infrared interferometry are now making it possible to obtain angular resolution approaching the milliarcsecond range; i.e., corresponding to tens of pixels across typical 100-km size class targets in the main belt. Each antenna pair in the array making up the interferometer samples the two-dimensional Fourier transform of the plane-of-sky thermal flux density [13]. Since the observable is already in the form of a Fourier transform, this data type is especially suitable for the FT approach of the inverse problem.

After enough Fourier transform samples are obtained, the Fourier transform may in principle be inverted to a form a dirty image, from which the actual final thermal image is reconstructed as a pixel field with the aid of various iterative algorithms and prior assumptions [13]. However, in the case of asteroids, we can use the mathematical model of the target as a very strong prior constraint, so the image-forming step can be discarded altogether and the raw Fourier data used directly for reconstructing the three-dimensional model. This is beneficial especially in the

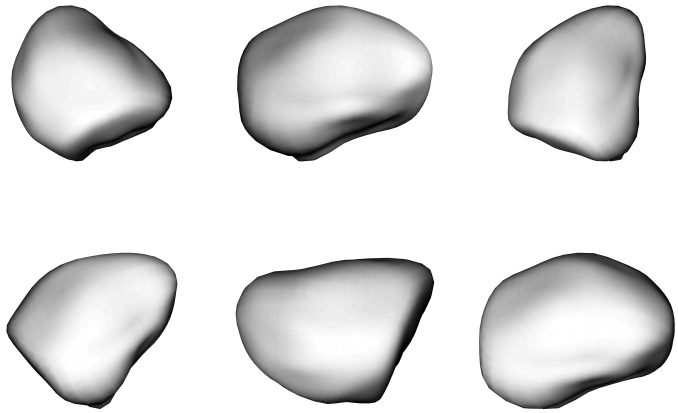

FIGURE 2. Reconstructed model of Daphne from adaptive optics images. Viewing directions correspond to the AO images shown in Fig. 1; in this sense, these images are results of model-based image processing. Shading is exaggerated with the Lambert law for clearer illustration.

cases where the Fourier plane is too sparsely sampled to form the image. In this sense, asteroids are particularly suitable for interferometric observations. We will discuss the practical aspects of the interferometric inversion procedure elsewhere, and present the main theoretical points here.

Thermal-range interferometry differs from optical wavelengths in that the radiation of the surface cannot be described as simply as with light-scattering models. However, we note here an uniqueness result concerning the optical-equivalent region, meaning optical wavelengths or other domains where the boundary curves of the image of the radiating target are the same as those in the optical region. This is the case with, e.g., zero thermal inertia, when the surface releases the received radiation energy immediately.

Theorem 4.1. *The uniqueness theorems obtained with image boundaries in* [8] *are valid for interferometry (or image fields) in the optical-equivalent case.*

Proof. This is an immediate corollary of $\mathcal{F}^{-1}\mathcal{F} = \mathbb{I}$: due to $\mathcal{F}^{-1}$, full coverage of the (u, v)-plane data at different viewing geometries uniquely produces a full set of (ξ, η) images for which the uniqueness results are derived. Note that one does not need to produce images (and extract the boundaries) from the FT data by $\mathcal{F}^{-1}$; the result applies to the (u, v)-data directly since no other model can match the boundaries if the images are constructed (we assume that the light-scattering model is correct). This applies to image field data directly, of course. □

The resolution provided by thermal-range inteferometers makes it possible to build detailed $3D$ models of asteroids if the thermal radiation and conduction process on the surface and in the subsurface layer can be modelled with sufficient accuracy. Several models for asteroid heat radiation exist, with varying complexity [4].

As the facets in the polyhedral mesh of the model are usually much larger than the diurnal thermal skin depth, it is reasonable to assume that heat is conducted only in the direction of the facet normal. Hence it is enough to solve the one-dimensional heat diffusion equation with a radiation boundary condition for each facet, with shadowing and mutual heating between facets taken into account.

Calculating the heat flux of an polyhedral model consists of solving the heat diffusion equation numerically for each facet and for each time step. For even moderately-sized models, with the shadowing and the diurnal solar radiation variation taken into account, it can be prohibitively expensive computationally.

An elegant alternative approach to the finite difference-method is the Fourier-series method [1, 11] briefly described below in view of our application. As the fast Fourier transform is computationally cheap, the Fourier-series approximation is much faster than the finite-difference method for solving the diffusion equation. The downside is that the approximation originally pertains to moderate heat variations, and the mutual heating of facets must be ignored. However, even in this case the Fourier-series approximation will still provide good initial values for the finite-difference method decreasing the computation time.

From the point of view of the inverse problem, the Fourier-series method, though an approximation, is nevertheless quite adequate for describing the observed radiative flux (thermal brightness) on the object's surface. This is because, again, the bulk of the information comes from the boundary of the target (a heated surface patch vs. cold background). Just as in the adaptive optics case, the accuracy of the model of the interior intensity distribution is not crucial.

4.2.1. *Diurnal cycle and Fourier series.* We present here the main points of the Fourier-series thermal approach. We define the insolation factor $\mathrm{ins}(\mu_0, p)$ for a point p on the surface [10] as

$$\mathrm{ins}(\mu_0, p) = \begin{cases} \mu_0, & p \text{ is illuminated,} \\ 0, & \text{otherwise.} \end{cases}$$

This is obviously a cyclic function of ϕ, the rotation angle of the asteroid around its axis (when the asteroid is effectively stationary during one rotation; i.e., its rotation period is much smaller than the orbital one), so it can be expanded as a Fourier series:

$$\mathrm{ins}(\mu_0, p) = \sum_n d_n \, e^{in\phi}. \tag{7}$$

For a convex body, the function $\mathrm{ins}(\mu_0, p)$ is continuous. If the minimum and maximum limits of ϕ for $\mu_0 \geq 0$ are, respectively, ϕ_{rise} and ϕ_{set} for a point p, we have

$$d_n(p) = \frac{1}{2\pi} \int \mathrm{ins}(\mu_0, p) \, e^{-in\phi} \, d\phi = \frac{1}{2\pi} \int_{\phi_{\mathrm{rise}}(p)}^{\phi_{\mathrm{set}}(p)} \mu_0(p, \phi) \, e^{-in\phi} \, d\phi. \tag{8}$$

The coefficients $d_n(p)$ can be readily computed analytically to any order n.

For a nonconvex body, we check the interval $[\phi_{\mathrm{rise}}, \phi_{\mathrm{set}}]$ for facets rising above the local horizon and blocking the Sun at some ϕ (dividing the interval into N epochs).

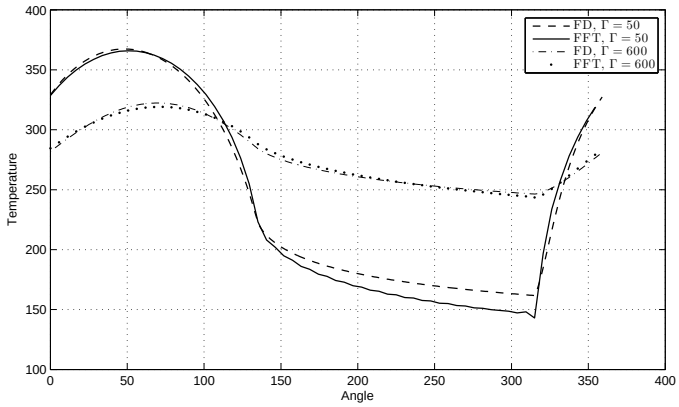

FIGURE 3. Comparison of two solutions of the diffusion equation for two different values of thermal inertia

Then we write the Fourier integral as above to obtain $d_n(p)$, when the integrand is zero between shadow epochs ϕ_{in} and ϕ_{out} (this creates derivatives w.r.t. shape parameters). Since the integration limits ϕ_{in} and ϕ_{out} are approximate, one can just as well compute the integral by taking the FFT of the values of $\text{ins}(\mu_0, p)$ of 2^M equidistant epochs distributed inside $[0, 2\pi]$; this gives the Fourier coefficients up to order 2^{M-1}. The derivatives of d_n w.r.t. parameters can also be computed simply by taking the FFT of the derivatives of $\text{ins}(\mu_0, p)$. In fact, one can use FFT for convex bodies as well for an approximation. Now $\text{ins}(\mu_0, p)$ is discontinuous for some p, so the Fourier representation is more approximative than in the convex case.

4.2.2. *Heat diffusion equation and IR flux.* The heat diffusion equation (with density ρ, heat conductivity K, specific heat capacity c_p, and temperature T) is given by

$$\rho c_p \frac{\partial T}{\partial t} = K \frac{\partial^2 T}{\partial \xi^2}, \tag{9}$$

where the vertical direction ξ in the surface material is aligned with the direction of the surface normal.

This can be solved analytically with a suitable boundary condition, a periodic ansatz, and by assuming that the temperature variation ΔT is small compared to the mean temperature T_0. Then we can linearize equations and solve for ΔT as a Fourier series [1, 11]. We define damping factors Ψ_n and phase lags $\Delta\phi_n$ by

$$\Psi_n = (1 + 2\Theta_n + 2\Theta_n^2)^{-1}, \quad \Delta\phi_n = \text{sgn}(n) \arctan \frac{\Theta_n}{\Theta_n + 1}, \tag{10}$$

where

$$\Theta_n = \frac{\sqrt{\rho c_p}}{4\varepsilon\sigma T_0^3} \sqrt{\frac{1}{2}|n|\, K\, \omega}, \quad T_0^4 = (1 - A) F_o / \varepsilon\sigma,$$

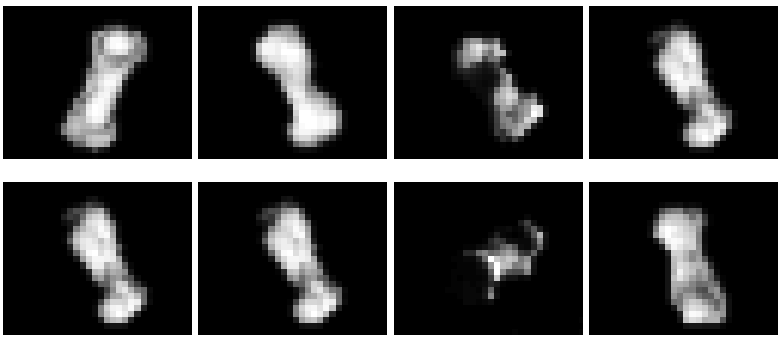

FIGURE 4. Simulated thermal infrared flux images of an asteroid.

and ω is the rotation rate of the asteroid, ε the material emissivity at thermal wavelengths, A the albedo (lightness, $0 \le A \le 1$, of the surface material), σ the Stefan-Boltzmann constant, and F_o the solar flux at the asteroid. Then the radiated IR flux at a point p_i (the centroid of facet i) per surface area is

$$B_i = C\,\varepsilon\sigma T(t)^4|_{\xi=0} \simeq C\,(1-A)F_o \sum_n \Psi_n\, d_n(p_i,t)\, e^{i[n\omega(t-t_0)-\Delta\phi_n]}. \tag{11}$$

The assumption $\Delta T/T \ll 1$ does not always hold. This is dependent on the thermal inertia Γ, which is defined as

$$\Gamma = \sqrt{K\rho c_p}.$$

Thermal inertia measures how resistant the surface is to diurnal temperature changes; an object with a high thermal inertia is cooler with smaller diurnal temperature variations than an object with relatively small thermal inertia. It follows that for objects of low thermal inertia $\Delta T/T \ll 1$ no longer necessarily holds, and the FFT solution deviates from the numerical finite-difference solution of the diffusion equation [4]. This is illustrated in Fig. 3. However, in our simulations this discrepancy between the solutions has an indiscernible effect to the final shape solution. The shapes of the thermal curves are essentially same for the two methods, and the largest temperature differences do not matter in the inversion.

The Atacama large submillimeter array (ALMA) is an interferometer array in the Chilean desert. The maximum spacing between the antennas is 16 kilometers, making possible the resolution of 5 milliarcsecond at infrared wavelengths. Even if the detail present in many radar images is unattainable by the thermal infrared observations, a thermal map of an asteroid surface is enough for shape reconstruction, as we demonstrate here.

To generate the simulated data, we considered a hypothetical asteroid at the heliocentric distance 1.5 AU, with a thermal inertia of 100 $Jm^{-2}Ks^{-\frac{1}{2}}$ and the albedo 0.1. The pixel size of the instrument is assumed to be 10 milliarcseconds which, taking into account the distance of the target from the Earth, corresponds to approximately 10 kilometers per pixel. The plane-of-sky projections of observed thermal flux of the model asteroid are illustrated in Fig. 4. The actual data are the samples of the Fourier transforms of these projections. To avoid 'inverse crime', the

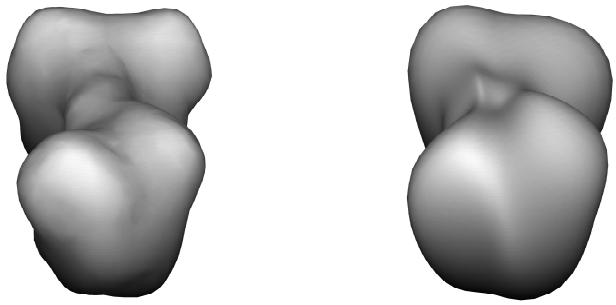

FIGURE 5. Original model (left) and the shape reconstructed from the thermal images shown in the previous figure.

data were generated with the finite difference method, and the FFT method was used in the inversion. The original model and the reconstructed shape parametrized by 108 parameters are shown in Fig. 5.

4.3. **Range-Doppler radar.** With planetary radar observations, spatial resolution of the scale of ten meters is possible (Arecibo and Goldstone radars) [12]. Unfortunately the power received by the radar is inversely proportional to the fourth power of distance, severely restricting the range of possible targets. In range-Doppler imaging the object is resolved in the range and in the frequency. A nonzero radial velocity of a point on the surface of the object causes a frequency shift in the reflected signal proportional to the velocity. Thus the frequency resolution of a radar image depends on the apparent spin vector of the asteroid. Now the projection mapping $(x, y, z) \to (r, D)$ is [7]

$$\begin{aligned} r &= (x\cos\varphi + y\sin\varphi)\sin\theta + z\cos\theta, \\ D &= \omega\sin\theta\,(x\sin\varphi - y\cos\varphi), \end{aligned} \tag{12}$$

where the radar direction in a coordinate system fixed to the asteroid (the z-axis aligned with the rotation axis) is (θ, φ), and the rotation rate of the asteroid is ω. The image mapping of this, unlike the previous ones, is many-to-one. The many-to-one mapping property and the depth vs. width plane makes visual image interpretation tricky; ridges and craters visible in the radar image are not necessarily physical features, but could also be artefacts due to the peculiar way the image is formed. For the scattering law we use a simple cosine law [12]:

$$B_i = C\,[\mu^{(i)}]^n.$$

The specularity of the surface is measured by the exponent n.

We next state a uniqueness theorem on radar-based shape determination, based on boundary contours. In practice, the boundary curve method for radar images is not as simple to implement as for adaptive optics images. The uniqueness result here is not so much a prescription for reconstruction as a statement on the minimal information content of radar images (indeed, noisy radar images have most of their information on a boundary curve). It also shows formally what is apparent numerically: that the many-to-one mapping of the radar image is no hindrance to obtaining shape details.

For other uniqueness results on radar, see [7]. For details of the terminology and definitions of silhouettes and shape reconstruction see [8]. As in the other uniqueness results on shape reconstruction, we assume the geometry of the system to be known; i.e., the rotation speed and the direction of the rotation axis are given. By a *free tangent* we mean a tangent of a surface point that does not intersect any other parts of the body (except as a possible tangent of some other point), and a *free direction* on S^2 means that a half-line in that direction from a surface point does not intersect the body either.

The *nearest radar image boundary* ρ is the boundary of the radar image closest to the radar direction; i.e., the curve $\rho(D) = \min r|_D$, where r is the range of an image pixel from the radar and D is the Doppler width, $D_{\min} \le D \le D_{\max}$. Note that $\rho(D)$ can be discontinuous. The nearest boundary is usually the clearest feature of a radar image, and if we use just $\rho(D)$, we can disregard both pixel brightnesses and scattering models. The data and inverse problem model are thus robust. We also normalize, as in [7],

$$\tilde{D} := \frac{D}{\sin\theta},$$

and assume that the radar image plane $(r, \tilde{D})$ is defined for all directions $\omega = (\theta, \phi) \in S^2$; i.e., that the limits at $\theta \to 0$ and $\theta \to \pi$ exist, even though in these directions $D = 0$ for all image points and the image contracts to a line in r.

Definition 4.2. A *direction pair* is given by the direction $\omega = (\theta, \phi)$ on S^2 and its image $\mathcal{S}\omega = (k\pi + \pi/2 - \theta, \phi + \pi)$, where $k = 0, 0 \le \theta \le \pi/2$, and $k = 1, \pi/2 < \theta \le \pi$. The pair is one-to-one and symmetric: $\mathcal{S}^{-1} = \mathcal{S}$.

Theorem 4.3. *The shape of a body for which each surface point has at least one direction pair consisting of a free tangent (either of its two directions) and a free direction is uniquely reconstructable from the nearest radar image boundaries obtained at radar directions covering the whole of* S^2.

Proof. The nearest boundary $\rho(\tilde{D})$ of a radar image in the direction ω defines part of a silhouette in the plane whose normal is $\mathcal{S}\omega$ (hence the many-to-one mapping causes no ambiguity in this construction). The part occluded by the body is obtained at the opposite radar direction $-\omega$ (the silhouette planes $\mathcal{S}\omega$ and $\mathcal{S}(-\omega)$ coincide). Since the images are obtained at all $\omega \in S^2$, and each point on the surface is thus mapped onto at least one silhouette plane by the assumption of the theorem, the body can be reconstructed as in [8] by taking the intersection of the cylinder continuations of the silhouettes in $\mathbb{R}^3$ (this also takes care of possible discontinuous $\rho(\tilde{D})$ since each surface point is covered by at least one image boundary). □

Remark 1. The set $\mathcal{R}$ of bodies reconstructable from radar boundaries is a subset of the set $\mathcal{T}$ of bodies reconstructable from their silhouettes (these are tangent-covered bodies; i.e., each surface point has at least one free tangent [8]). The set $\mathcal{C}$

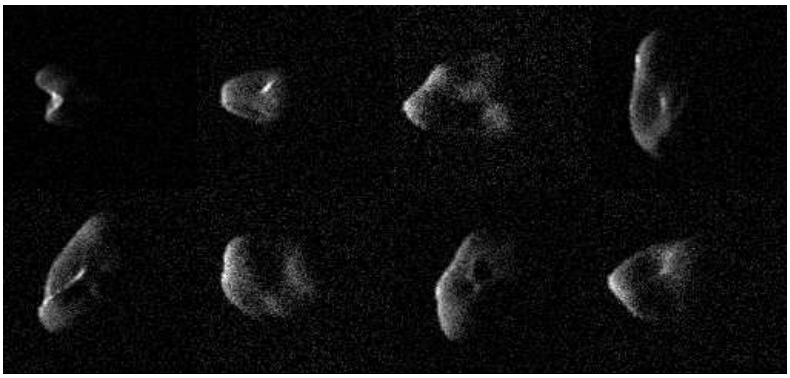

FIGURE 6. Simulated radar images. The range r increases from left to right, and the Doppler frequency D is measured vertically. The nearest boundary $\rho(D)$ is the leftmost boundary of each image.

of convex bodies, reconstructable from integrated brightnesses on S^2, is obviously a subset of $\mathcal{R}$. Thus we can arrange the sets of bodies reconstructable from various image boundary data in the sequence

$$\mathcal{C} \subset \mathcal{R} \subset \mathcal{T} \subset \mathcal{G},$$

where $\mathcal{G}$ is the set of bodies reconstructable from their edge and shadow boundaries [8].

Among natural bodies such as asteroids, the set $\mathcal{R}$ is not much smaller than $\mathcal{T}$ or $\mathcal{G}$ (for example, a curved banana is in $\mathcal{R}$). In other words, the radar boundary data define a typical shape almost as well as adaptive optics boundary data. The pixel brightnesses can be used to determine concave details (valleys and craters not visible in silhouettes). As Fig. 6 shows, there is much more information in full radar images than just the boundary. Indeed, the body that created those images is clearly not in $\mathcal{T}$. However, general uniqueness results on such data (as well as full optical image fields) are difficult, and perhaps impossible, to prove.

As real observed data sets are currently unavailable to us, we have to rely on simulations to test our reconstruction algorithm. In Fig. 6 simulated radar images are shown, obtained from the model in Fig. 7 (left) with added Gaussian blurring and noise. Our reconstructed model uses 108 shape parameters, and for each radar image, the optimal offset on the plane and the scaling parameter are also determined during the optimization process. The goal here was to produce an intermediate-resolution model rather than a high-resolution one. In principle, the latter could be achieved by adjusting the individual vertices of the model after determining the function series, but usually the noise level sets limits for this; we will discuss this aspect elsewhere.

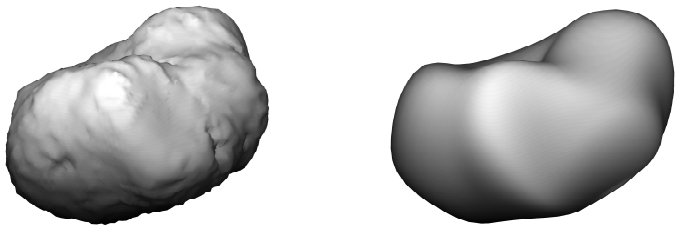

Figure 7. Original model (left) and the reconstructed model (right) from simulated radar images.

5. **Discussion.** We have completed the series of papers describing the theory and solution procedures of inverse problems of generalized projections. In [5, 6], the solution of shape and spin reconstruction from integrated brightnesses was presented with uniqueness results, and the general concept of generalized projections was introduced in [7] with uniqueness results on some radar observation types. Boundary-curve solutions for images and the corresponding uniqueness theorems, special types of interferometric data, and the methods for combining data from different source types were discussed in [8, 9]. Here we have introduced an efficient way of solving the inverse problems of various image types with the Fourier transform approach, and presented uniqeness results on general interferometry and radar data.

Now we have practical and efficient theoretical and computational methods at our disposal for all the data types associated with generalized projections in astronomy: photometry (integrated brightnesses), adaptive optics or stellar occultations (images and their boundaries), radar, and interferometry. We plan to combine these into a general software package for data analysis.

Acknowledgments. We thank Josef Ďurech, Benoit Carry, and Marco Delbó for valuable discussions and comments, and the use of AO data. This work was supported by the Academy of Finland (the project "Inverse problems of regular and stochastic surfaces" and the centre of excellence in inverse problems).

REFERENCES

[1] B. Bertotti, P. Farinella and D. Vokrouhlický, *Physics of the Solar System*, Astrophysics and Space Science Library (Kluwer), **293** (2003).

[2] B. Carry, C. Dumas, M. Kaasalainen and 9 colleagues, Physical properties of 2 Pallas, *Icarus,* **205** (2010), 460–472.

[3] B. Carry, M. Kaasalainen, W. J. Merline and 12 colleagues, Shape modeling technique KOALA validated by ESA Rosetta at (21) Lutetia, *Planet. Space Sci.,* **66** (2012), 200–212.

[4] M. Delbó, *The Nature of Near-Earth Asteroids from the Study of Their Thermal Infrared Emission*, Ph.D. thesis, Freie Universität Berlin, 2004.

[5] M. Kaasalainen, L. Lamberg, K. Lumme and E. Bowell, Interpretation of lightcurves of atmosphereless bodies. I. General theory and new inversion schemes, *Astron. Astrophys.,* **259** (1992), 318–332.

[6] M. Kaasalainen, J. Torppa and K. Muinonen, Optimization methpds for asteroid lightcurves inversion. II. The complete inverse problem, *Icarus,* **153** (2001), 37–51.

[7] M. Kaasalainen and L. Lamberg, Inverse problems of generalized projection operators, *Inverse Problems,* **22** (2006), 749–769.

[8] M. Kaasalainen, Multimodal inverse problems: Maximum compatibility estimate and shape reconstruction, *Inverse Problems and Imaging,* **5** (2011), 37–57.
[9] M. Kaasalainen and M. Viikinkoski, Shape reconstruction of irregular bodies with multiple complementary data sources, *Astron. Astrophys,* **543** (2012), 9pp.
[10] M. Kaasalainen and H. Nortunen, Compact YORP formulation and stability analysis, *Astron. Astrophys,* **558** (2013), 8pp.
[11] D. Nesvorný and D. Vokrouhlický, Analytic theory for the Yarkovsky-O'Keefe-Radzievski-Paddack effect on obliquity, *Astron. J.,* **136** (2008), 291–299.
[12] S. J. Ostro, R. S. Hudson, L. Benner and 4 colleagues, *Asteroid Radar Astronomy*, in Asteroids III, Arizona University Press, 151, 2002.
[13] A. R. Thompson, J. M. Moran and G. W. Swenson, *Interferometry and Synthesis in Radio Astronomy*, Interferometry and Synthesis in Radio Astronomy, Second Edition, 2007.

Received December 2013; revised April 2014.

E-mail address: matti.viikinkoski@tut.fi
E-mail address: mikko.kaasalainen@tut.fi

Publication III

Viikinkoski M., Kaasalainen M. and Ďurech J., "ADAM: a general method for using various data types in asteroid reconstruction," *Astronomy & Astrophysics* 576 (2015):A8

Reproduced with permission from Astronomy & Astrophysics, ©ESO 2015

A&A 576, A8 (2015)
DOI: 10.1051/0004-6361/201425259
© ESO 2015

Astronomy & Astrophysics

ADAM: a general method for using various data types in asteroid reconstruction⋆

Matti Viikinkoski[1], Mikko Kaasalainen[1], and Josef Ďurech[2]

[1] Department of Mathematics, Tampere University of Technology, PO Box 553, 33101 Tampere, Finland
e-mail: matti.viikinkoski@tut.fi
[2] Astronomical Institute, Faculty of Mathematics and Physics, Charles University in Prague, V Holešovičkách 2, 18000 Prague, Czech Republic

Received 1 November 2014 / Accepted 26 January 2015

ABSTRACT

We introduce ADAM, the All-Data Asteroid Modelling algorithm. ADAM is simple and universal since it handles all disk-resolved data types (adaptive optics or other images, interferometry, and range-Doppler radar data) in a uniform manner via the 2D Fourier transform, enabling fast convergence in model optimization. The resolved data can be combined with disk-integrated data (photometry). In the reconstruction process, the difference between each data type is only a few code lines defining the particular generalized projection from 3D onto a 2D image plane. Occultation timings can be included as sparse silhouettes, and thermal infrared data are efficiently handled with an approximate algorithm that is sufficient in practice because of the dominance of the high-contrast (boundary) pixels over the low-contrast (interior) pixels. This is of particular importance to the raw ALMA data that can be directly handled by ADAM without having to construct the standard image. We study the reliability of the inversion, using the independent shape supports of function series and control-point surfaces. When other data are lacking, one can carry out fast non-convex lightcurve-only inversions, but any shape models resulting from it should only be taken as illustrative large-scale models.

Key words. minor planets, asteroids: individual: 2000 ET70 – methods: analytical – minor planets, asteroids: general – methods: numerical – minor planets, asteroids: individual: Daphne

1. Introduction

Ground-based and other remote-sensing data on asteroids are obtained with a variety of instruments that essentially sample regions on the surface of the target in various ways. These share some common mathematical characteristics of generalized projections (Kaasalainen & Lamberg 2006; Kaasalainen 2011; Viikinkoski & Kaasalainen 2014). The most abundant source of data for asteroid shape and spin reconstruction is disk-integrated photometry, because even data that are sparse in time are often sufficient for modelling (Kaasalainen 2004; Ďurech et al. 2006). Lightcurve-inversion procedures (Kaasalainen et al. 2001) are available at e.g. the Database of Asteroid Models from Inversion Techniques (DAMIT) site[1]. Because of the inherently limited information content of the disk-integrated data, the corresponding models are usually most reliably described in convex space (Ďurech & Kaasalainen 2003, and further discussed below). However, even partially disk-resolved data offer a realistic possibility of more detailed modelling. Previously described approaches for such reconstruction are the SHAPE software (Ostro et al. 2002) for radar and lightcurve data, and the KOALA procedure (Kaasalainen & Viikinkoski 2012; Carry et al. 2012) for optical images, occultation timings, and lightcurves.

The best way to reconstruct a model of an asteroid is to use all available data. To combine disk-resolved data (adaptive optics or other images, interferometry, and range-Doppler radar data) with disk-integrated data (photometric or infrared lightcurves) and occultation timings ("sparse silhouettes"), we need a general procedure for using any data sources in asteroid modelling. We call this ADAM: all-Data Asteroid Modelling. Concise accounts of the various data types and their modelling aspects are given in Kaasalainen & Lamberg (2006), Kaasalainen & Ďurech (2013), and Ďurech et al. (2015). This paper is intended as a technical companion to those reviews.

We present the ADAM algorithm in a high-level format that includes all the necessary methods and formulae, either written here or given by references to the literature. We discuss and collect the essential techniques and aspects of a complete inversion procedure capable of handling all the major asteroid data sources and formats. The key point is that complementary data sources can facilitate a good reconstruction even when none of them is sufficient alone.

The paper is organized as follows. In Sect. 2 we describe the various shape supports we use in the reconstruction; some with the emphasis on global features, some concentrating on local details. This is intimately connected with the reliability estimate of the result, since independent shape representations help to reveal the most probable features. Section 3 introduces the Fourier transform method necessary for a simple and universal handling of data sources of disk-resolved type. In Sect. 4, we present examples of these types (interferometry, radar, and optical images). The interferometric data from ALMA are of particular interest. We also discuss the special case of one-dimensional projections (continuous-wave radar and certain types of interferometry). In Sect. 5 we sum up everything in the form of the

⋆ The code is only available at the CDS via anonymous ftp to cdsarc.u-strasbg.fr (130.79.128.5) or via http://cdsarc.u-strasbg.fr/viz-bin/qcat?J/A+A/576/A8
[1] http://astro.troja.mff.cuni.cz/projects/asteroids3D

ADAM algorithm, and conclude in Sect. 6. Some basic ADAM functions are listed in Appendix A.

Using the methods and algorithm described here and in Kaasalainen et al. (2001), Kaasalainen (2011), and Kaasalainen & Viikinkoski (2012), writing an ADAM program from scratch is quite straightforward (for example, convex lightcurve inversion is inherently more complex). We have uploaded free ADAM code files and functions written in Matlab and C to a toolbox at the DAMIT site. These can be used for writing customized inversion software, and for browsing and understanding the computational methods. These methods, too numerous to be discussed here in detail, include techniques, such as the partial derivative chains for gradient-based optimization, ray-tracing procedures, projections and transforms, scattering and luminosity models, GPU acceleration, etc. (Note that we do not offer any user support: the files are presented as is.)

The ADAM procedure is a considerably more general package than the KOALA (Kaasalainen & Viikinkoski 2012; Carry et al. 2012), which is based on extractable image contours. The KOALA contour-fitting principle is necessary for including occultation data, so a full ADAM procedure inherits this function from KOALA. For fitting any pixel images, we recommend the ADAM Fourier-transform functions rather than KOALA.

We take asteroid reconstruction to mean here that the following output parameters are derived from input data: 1) shape (surface) definition; 2) rotational state (period and spin axis direction; possibly also terms for YORP acceleration, precession, or a binary orbit); 3) scattering or other luminosity parameters (often fixed a priori); and 4) image offset (alignment) and possible other auxiliary or normalization terms. Without the loss of generality, we do not discuss each item separately, but mostly take the shape parameters to represent all the free parameters since the optimization principle is technically the same for all parameter types. The speed, convergence, and reliability of gradient-based optimization methods are here superior to global optimization methods (such as genetic algorithms or Monte Carlo; see the discussion in Kaasalainen et al. 2001). We emphasize that the spin parameters, especially the period, usually have numerous local minima, so a dense enough comb of initial values of these parameters is a prerequisite for a good final reconstruction.

2. Shape

Given the diverse shapes of asteroids and the continuing progress in instrument technology, effective methods for shape representation are required for a general reconstruction scheme from observations. In inverse problems it is typically not clear a priori how well a given shape support will perform. In this section we present shape supports and corresponding regularization functions well suited for asteroid-like shapes.

2.1. Shape supports

An important part of shape modelling is the choice of shape representation. Assuming a typical asteroid surface is homeomorphic to the unit sphere, we can consider each coordinate as a function on the sphere, and choosing a suitable basis for functions, expand coordinate functions using this basis. This can be generalized to multiple bodies such as binaries in a straightforward manner. Typical such bases are spherical harmonics, spherical wavelets, and spherical splines. Our experiments suggest that parametrizations, which expand each coordinate function separately, tend to produce suboptimal results since they ignore the geometric dependencies and constraints between coordinates when considering surfaces represented by non-tangled meshes. Thus we have found it useful to consider two well-regulated, but conceptually different, shape supports in practice: octantoids based on spherical harmonics, and subdivision surfaces.

2.1.1. Function series

An octantoid is a surface given by $p \in \mathbb{R}^3$ that can be parametrized in the form

$$p(\theta,\varphi) = \begin{cases} x(\theta,\varphi) = & \mathrm{e}^{a(\theta,\varphi)} \sin\theta\cos\varphi, \\ y(\theta,\varphi) = & \mathrm{e}^{a(\theta,\varphi)+b(\theta,\varphi)} \sin\theta\sin\varphi, \\ z(\theta,\varphi) = & \mathrm{e}^{a(\theta,\varphi)+c(\theta,\varphi)} \cos\theta, \end{cases} \quad (1)$$

where a, b and c are conveniently expressed as linear combinations of the (real) spherical harmonic functions $Y_l^m(\theta,\varphi)$, with coefficients a_{lm}, b_{lm} and c_{lm}, respectively. Note that (θ,φ), $0 \le \theta \le \pi$, $0 \le \varphi < 2\pi$, are coordinates on the unit sphere S^2 parametrizing the surface, but not describing any physical directions such as polar coordinates. As usual, the Laplace series for a, b, c are useful for keeping the number of unknowns; i.e. the coefficients of Y_l^m, small and the surface smooth. If $b = c = 0$, this representation is the usual star-like one with the radius $\exp(a)$, but we have found that even if the target is star-like, the octantoid form allows us to capture of detail better, and b and c we can represent with considerably fewer terms than the main function a. The number of shape parameters is thus between the $(l_{\max}+1)^2$ of the star-like case and $3(l_{\max}+1)^2$, when $l_{\max}$ is the largest degree of the function series. The drawback of this representation is its globality: one might want less smoothness regularization in some regions than in others. When more local control is desired (e.g. a feature clearly visible in fly-by images or in radar), the representation (1) may be expanded with spherical splines or spherical wavelets to provide local detail without affecting the global shape. Depending on the desired level of resolution and the non-star-like irregularity of the surface, the number of free function series coefficients is typically between 50 and 300 from low- to mid-resolution. Function series are seldom useful for high resolution, where one may ultimately want to adjust each vertex separately by defining individual a_i, b_i, and c_i.

2.1.2. Subdivision control points

Subdivision surfaces offer local control more than global representations like function series. Beginning with an initial set of vertices and corresponding triangles, called a control mesh, the surface is iteratively refined by adding new vertices and computing new positions for old vertices. The vertex coordinates of the control mesh form the parameter set defining the surface. Each subdivision step smoothes out the surface in a higher level of resolution. Those subdivision schemes that are well-behaved converge to a smooth limit surface.

In this paper, we use the Loop subdivision scheme (Loop 1987). Considering a vertex p with immediate neighbours $p_0, \ldots, p_{n-1}$, the subdivision method first creates new vertices by splitting each edge

$$q_i = \frac{3p + 3p_i + 3p_{i-1} + p_{i+1}}{8}, \qquad i = 0, \ldots, n-1, \quad (2)$$

where the indices should be interpreted as modulo n. After the vertex creation step, the position of the vertex p is refined as

$$p' = (1 - n\beta)p + \beta \sum p_i. \quad (3)$$

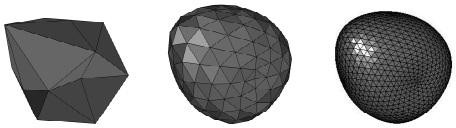

Fig. 1. Original control mesh (*left*) with 18 vertices (54 coordinates) as the shape parameter set and 32 facets, after two $\sqrt{3}$-subdivision steps (*middle*), and after four subdivision steps (*right*).

The multiplier β is usually chosen to be

$$\beta = \frac{1}{n}\left[\frac{5}{8} - \frac{(3+2\cos(2\pi/n))^2}{64}\right], \tag{4}$$

but other choices are also possible. The limit surface is continuous; C^2 at the ordinary vertices (i.e. vertices that have six neighbours) and C^1 at extraordinary vertices. The number of free control points for model rendering is similar to or somewhat lower than the number of function series coefficients (for a comparable level of resolution).

The main computational aspect with subdivision methods is that the number of facets increases exponentially with the number of divisions. After n subdivision steps, each facet that has been divided has produced 4^n subfacets. An alternative scheme to Loop subdivision is the $\sqrt{3}$-subdivision (Kobbelt 2000). Instead of splitting the edges, $\sqrt{3}$-scheme subdivides facets by inserting a new vertex to the facet centroid and connecting it to the vertices of the facet (Fig. 1). The main attraction of the $\sqrt{3}$-scheme compared to the Loop subdivision is the slower increase (3^n) of facets, while performing similarly in the limit.

In practice, it is usually a good idea to choose the initial control mesh to be an ellipsoid or a scaled convex surface obtained from lightcurve inversion, with a suitable number of vertices for the mesh. The number of subdivision steps should be chosen carefully: while each subdivision increases resolution and stability by spreading the influence of each parameter to a larger number facets, the computational burden grows exponentially. Instead of subdividing all the facets, better performance may be obtained with adaptive subdivision, where only facets benefiting from increased resolution are subdivided. However, it is not obvious how to do this automatically during optimization. A heuristic inclusion of surface regions to be refined based on a ranking of the improvement of the fit is one possibility (cf. the χ^2-sensitivity map of Kaasalainen & Viikinkoski 2012); visual inspection of the model fit and a graphical user interface can guide the refining process.

2.2. Regularization functions

In inverse problems, finding a feasible regularization method is typically the most delicate part of problem solving. Ideally, both the shape representation and regularization method should be chosen to complement each other. The shape support should be general enough to represent probable shapes, and the regularization should prevent unrealistic or degenerate shapes while, at the same time, reveal the features present in the data. For octantoids, the choice is remarkably easy. Assuming the basic shape is geometrically star-like, it is intuitively obvious to penalize the deviation from star-likeness. To this effect, we define

$$\eta = \sum_{l,m} l\left(b_{lm}^2 + c_{lm}^2\right). \tag{5}$$

Every star-like surface has a representation for which $\eta = 0$, so η is a natural quantity to be included in the final χ^2-function to be minimized (Sect. 5). The χ^2-sum contains both the goodness-of-fit measure and the regularizing functions that represent prior assumptions and expectations of the solution.

Subdivision surfaces have somewhat different smoothness properties in this regard. It is well known that the Loop subdivision converges to a smooth surface, so each subdivision step will produce a smoother result. However, it is computationally expensive to take a large number of subdivision steps. Therefore, it is advantageous to combine a few, usually two or three, subdivision steps with mesh-based regularization methods.

While not strictly necessary, it is convenient to assume that the triangular mesh representing the shape forms a manifold. This assumption makes the checking of shadowing and illumination both conceptually and computationally simpler. Thus it is imperative to avoid self-intersections, as they introduce errors to the fitting process. One approach is to explicitly check for intersecting facets and retriangulate if required. However, triangulation and intersection tests are costly, and usually optimization steps leading to self-intersections are suboptimal. A better approach is to prevent self-intersections in the first place.

Regularization based on dihedral angles penalizes large angles between adjacent facet normals; i.e. the regularization prefers planar regions. We thus want to minimize

$$\gamma_1 = \sum_{i,j\in\mathcal{T}} w_{ij}(1 - \nu_i \cdot \nu_j), \tag{6}$$

where $\mathcal{T}$ are the facets of the mesh, and ν_k is the unit normal vector corresponding to the facet k. The sum is over all those facets j that are adjacent to the facet i, and the weights w_{ij} are usually chosen to be unity. As a special case, we may suppress only concave features, obtaining convex regularization (Kaasalainen & Viikinkoski 2012)

$$\gamma_2 = \frac{1}{\sum_j A_j}\sum_{i,j} A_j(1 - \nu_i \cdot \nu_j), \tag{7}$$

where A_i is the area of the facet i and the sum is over those facets j that are adjacent to the facet i and tilted above its plane.

To prevent degenerate facets and maintain a homogeneous mesh, it is advantageous to inhibit large variations in facet areas

$$\gamma_3 = \sum_i \left(A_i - \bar{A}\right)^2, \tag{8}$$

where $\bar{A}$ is the mean facet area of the polyhedron.

In practice, the regularization functions η and γ_2 are sufficient for octantoid surfaces, while γ_2 and γ_3 are useful for the subdivision surfaces. Unrealistically sharp angles can be prevented with γ_1, but a weight that is too large will inhibit convergence. In addition to geometric considerations, one can use regularization based on physical constraints, such as the requirement for the rotation axis to be close to the largest principal axis of the inertia tensor (Kaasalainen 2011; Kaasalainen & Viikinkoski 2012).

2.3. Reliability estimates

The octantoid representation or the subdivision mesh tend to produce aesthetically pleasing, "asteroid-like" surfaces, but it is not initially obvious which surface features of the model are actually present in the data, and which are the side effects of the shape support and the regularization used. Conventionally, Markov

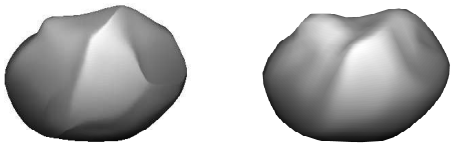

Fig. 2. Model of asteroid (41) Daphne from adaptive optics images, reconstructed as a subdivision surface (*left*) and an octantoid (*right*).

Fig. 3. Asteroid (6489) Golevka reconstructed from disk-integrated photometry. *From left to right*: convex, octantoid and subdivision surface.

chain Monte Carlo (MCMC) methods are used to obtain a reliability estimate for the model parameters. However, in our case, modelling and systematic errors usually dominate (Kaasalainen & Ďurech 2006), rendering the MCMC approach inefficient and inaccurate because the error distribution is not known (it is certainly not random Gaussian as in standard MCMC).

Moreover, the posterior distribution of shape parameters from MCMC will not really tell anything about the reliability of the model with respect to data, but only about the distribution of the estimate within the adapted shape support. We have found that this results in an overly optimistic conception of the reliability of the result, simply because the acceptable shape results cannot be probed widely enough using one shape support only. The Monte Carlo procedure focusses on regions of shape variation that are too small for both computational and geometric reasons. In addition, the computation of the model fit is time consuming if the data set and parameter space are large, making MCMC estimation computationally expensive.

To circumvent these obstacles, we have found the following approach fast and robust in practice. Any real feature of the model based on the data should also be present if another, independent model type such as a shape support is used. When model errors dominate, it is thus better to sample the "model space" within some χ^2 than the χ^2-space with some fixed model. As an example, shape models of the asteroid Daphne from adaptive optics images and photometry (Viikinkoski & Kaasalainen 2014), using both the octantoid representation and subdivision surfaces, are shown in Fig. 2. The models are quite similar and fit the data equally well, and their difference gives an idea of the real level of resolution. The MCMC probing with either shape support leads to small differences that are unrealistic (insignificant compared to those in Fig. 2). Even the shape-support test is likely to produce reliability limits that are too optimistic; the model error can be further enlarged by e.g. introducing random fluctuations in the scattering properties over the surface. This principle could be developed into a meta-level Monte Carlo procedure that probes the space of possible model types using latent parameters.

We conclude that shape sampling based on a fixed model type, no matter how diligently done with Monte Carlo or other methods, leads to overly optimistic resolution with artificial details. A typical example of this is the radar model of the asteroid Itokawa that portrayed imaginary detail at the resolution level expected from the data while not capturing even the large-scale features. There was nothing wrong with the model fit to the data as such: the inverse problem was not unique (or very unstable) because of the restricted observing geometries and instrumental projection (Sect. 4.2), but the constrained shape support of the program did not reveal this (Ostro et al. 2005; Nolan et al. 2014).

2.4. Inversion with photometry only

Since ADAM utilizes photometric data in addition to disk-resolved data, we note that ADAM can be used to reconstruct a model using only photometric data (simply using only the photometric fit function from the toolbox). This is easy and fast to do (and the shape rendering is even faster than the standard convex inversion of lightcurves), but the result is inevitably unreliable: it is well known that even sizable non-convex shape features require high solar phase angles to show in disk-integrated data (Kaasalainen et al. 2001; Ďurech & Kaasalainen 2003; Kaasalainen & Ďurech 2006). This can be probed with the shape reliability approach above.

As an example, we show reconstructed shapes of the asteroid Golevka in Fig. 3, based on the data in Kaasalainen et al. (2001). Both the subdivision method and the octantoid-based model display additional detail not seen in the convex model. However, the details are not supported by the data: the convex model gives at least as good a fit as the non-convex, as is almost always the case with lightcurves (so far the only case of a better non-convex model fit to photometry is that of the asteroid Eger in Ďurech et al. 2012). Indeed, with Golevka and other ground truth cases (maps from space probe missions), even the lightcurve fit with the correct shape and the scattering model assumed in inversion is not better than that with the convex model (Kaasalainen et al. 2001; Kaasalainen & Ďurech 2006). This underlines the fact that, because of systematic errors, any best-χ^2 optimized solution that relies only on photometry is likely to miss the details.

While the convex model yields the best overall agreement with the radar-based Golevka model (see the comparison in Figs. 3 and 4 in Kaasalainen et al. 2002), the non-convex models portray much of the general sharpness and ruggedness of the body even though their details are not correct. The convex shape presents something of a softened error envelope within which numerous local shape variations are possible (as if the target were seen unfocussed), while the non-convex representations are samplings of those variations. Their details coincide neither with each other nor with those in the radar-based model, but they are useful as illustrations and for probing the potential shape options (cf. the non-convex examples in Kaasalainen et al. 2004).

3. Fourier transform and information content

As discussed in Viikinkoski & Kaasalainen (2014), the Fourier transform (FT) facilitates a natural interpretation for the pixel size as the maximum frequency present in the data, and makes it easy to incorporate the impulse response function of the imaging system. It also makes the optimization procedure fast and straightforward, without the cumbersome aspects related to pixellated image fields and binned model image distributions. The principle of the ADAM approach is to compare, instead of the images themselves, a set of FT samples (typically some

thousands depending on the level of resolution) from the model image with those of the data image, and to iterate until the best fit is found. This is described in Sect. 5.

Letting $\mathcal{T}$ be the set of facets forming a model polyhedron and $\mathcal{P}$ a projection operator, the two-dimensional Fourier transform of a projected polyhedron in the (ξ, η)-plane is

$$\mathcal{F}(u,v) = \sum_{T_i \in \mathcal{T}} \iint_{\mathcal{P}T_i} B_i \, I_i(\xi,\eta) \, \mathrm{e}^{-2\pi\imath(u\xi+v\eta)} \, \mathrm{d}\xi \, \mathrm{d}\eta, \tag{9}$$

where B_i is the luminosity value of the facet i, and the function $I(\xi, \eta)$ is unity if the point projected on (ξ, η) is visible and zero otherwise. As shown in Viikinkoski & Kaasalainen (2014), we obtain by Green's theorem, dividing a facet into subfacets if necessary so that we may assume I is constant within each sub-facet,

$$\mathcal{F}(u,v) = \sum_i B_i \sum_j \mathcal{I}_{ij}(u,v), \tag{10}$$

where

$$\mathcal{I}_{ij}(u,v) = \frac{1}{4\pi^2(u^2+v^2)} \frac{(b-d)u-(a-c)v}{(a-c)u+(b-d)v} \times \left[\mathrm{e}^{-2\pi\imath(au+bv)} - \mathrm{e}^{-2\pi\imath(cu+dv)}\right] \tag{11}$$

for the jth boundary line segment (oriented counterclockwise) of the facet i, with the end points (a, b) and (c, d).

The summation over the interior edges of a projected polyhedron can be reordered by noting that each polygon edge in the interior is shared by two polygons, so a new factor $\tilde{B}$ can be taken to be the difference between the two B_i, and the edge term is computed only once. This explicitly shows why most of the information in the image is indeed from the limb and shadow boundary curves discussed in Kaasalainen (2011) and Kaasalainen & Viikinkoski (2012). The values of $\tilde{B}$ for interior triangle edges are usually close to zero (indeed, they vanish for the geometric scattering B_i = const.), so most of the weight is on the boundary edges. In practice, this is confirmed by the similar results for e.g. the asteroid Daphne obtained by KOALA and ADAM. There is little real information in the interior pixels of adaptive optics images, but on the other hand their errors do not distort the result either: the difference between the KOALA and ADAM models (for the same initial values and shape support) is negligible.

The role of boundary information can be understood when compared to the extreme case of lightcurve data: if we sum the pixel brightnesses over the image as in photometry, all the local shape information in the image is lost, so the remaining information is considerably more dependent on the light-scattering properties that are never very well known. With images the boundary contrast is always largest, however, so it is sufficient to have some kind of reasonable scattering (or thermal distribution) model to account for the interior pixel contrasts. Indeed, the uniqueness theorems on the image, interferometry, occultation, or radar data are based on robust boundary contour information (Kaasalainen 2011; Kaasalainen & Viikinkoski 2012; Viikinkoski & Kaasalainen 2014). With disk-integrated data only, Minkowski stability is luckily on our side when using convex models (Kaasalainen et al. 2001, 2002).

4. Data sources

The versatility of the ADAM algorithm enables the handling of different data sources with only minor changes to the instrument-dependent part of the procedure (essentially just the definition of the instrumental projection plane and the adopted point-spread function). In this section, we present diverse examples of shape reconstruction with ADAM using both simulated and observed data.

4.1. Interferometry and ALMA

The interferometric imaging method differs radically from a typical telescope; instead of observing the sky brightness directly, the interferometer samples the Fourier transform of sky brightness. Each antenna pair of the interferometric array determines one sample on the Fourier plane. The maximum separation between antennas determines the maximum attainable resolution. The interferometer most relevant to asteroid shape studies is the Atacama Large Millimeter Array (ALMA) in the Chilean desert. In its full configuration, the interferometer will be capable of observing at the resolution of a few milliarcseconds at the wavelength of 0.3 mm, corresponding to the separation of 16 km between antennas.

Given the brightness distribution $I(\xi, \eta)$ on the plane-of-sky, the visibility function is defined as the integral

$$V(u,v) = \iint I(\xi,\eta) \, \mathrm{e}^{-2\pi\imath(u\xi+v\eta)} \, \mathrm{d}\xi \, \mathrm{d}\eta, \tag{12}$$

which is a two-dimensional Fourier transform of the brightness distribution. Each antenna pair, corresponding to the projected baseline on the plane-of-sky, samples the visibility function. When the visibility function is sampled on a sufficiently dense set, the Fourier transform can be inverted to obtain the brightness distribution $I(\xi, \eta)$. Since the function $V(u, v)$ is measured only at a finite number of points, the observed visibility function is

$$\tilde{V}(u,v) = F(u,v) \, V(u,v), \tag{13}$$

where $F(u, v)$ is a sampling function corresponding to the sampled points on the (u, v)-plane. Thus the obtained brightness distribution is actually

$$\tilde{I}(\xi,\eta) = f(\xi,\eta) \star I(\xi,\eta), \tag{14}$$

i.e., a convolution of the true brightness distribution with the inverse Fourier transform $f(\xi, \eta)$ of the sampling function. Deducing the true brightness distribution I from the partially measured brightness $\tilde{I}$ is an inverse problem and there are several iterative algorithms to infer I from $\tilde{I}$, see, e.g. Labeyrie et al. (2006).

While the images obtained from the interferometer are informative, the great advantage with ADAM is that the algorithm works directly with the values of the visibility function obtained from the instrument. This approach has several distinct advantages:

- sparse data may be used (e.g. interferometry with a few baselines);
- the distribution of antennas does not cause bias, since the Fourier transform is not inverted;
- possible artefacts caused by the inversion process are avoided;
- the dependence between different observations is taken automatically into account.

To obtain the luminosity values for the model surface (i.e. the brightness factor B_i for each facet) in the infrared regime of ALMA, we can use the Fourier-series approximation of Nesvorný & Vokrouhlický (2008) as discussed in

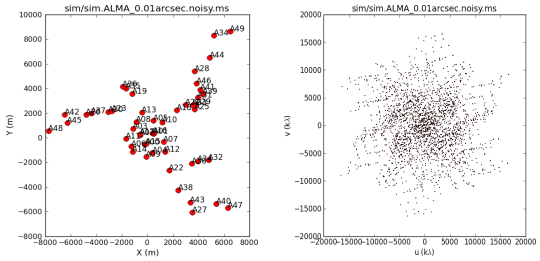

Fig. 4. Antenna locations of ALMA (*left*) and corresponding *uv*-plane visibilities (*right*). Images generated with the CASA software package.

Viikinkoski & Kaasalainen (2014). The fast analytical computations are then efficient in the optimization. A simple thermophysical model is sufficient for shape reconstruction, as the most relevant information is contained in the boundary data, which are quite robust with respect to our thermal model. This is in contrast to the disk-integrated thermal data that are more sensitive to both the surface properties and the thermal model.

For thermal infrared imaging, ALMA facilitates asteroid observations at resolution levels previously attained only by range-Doppler radar. To explore the possibilities of ALMA for shape modelling, we use the Common Astronomy Software Applications (CASA) package developed by National Radio Astronomical Observatory (NRAO) to simulate observations.

Consider a hypothetical asteroid with geocentric and heliocentric distances of 1.5 and 1 AU, respectively. The thermal flux is observed at the 350 GHz band, a frequency located in an atmospheric window. There are 11 observation runs, each observation lasting 50 s with 10 s integration time. We choose an antenna configuration providing approximate resolution of 10 mas, a resolution which is well within the capabilities of ALMA. The antenna configuration and the corresponding *uv*-plane sampling pattern are shown in Fig. 4. The uncorrupted plane-of-sky images, with a resolution of five milliarcseconds, are displayed in the column on the left in Fig. 5. We use the CASA software to add realistic atmospheric noise to the observations. The resulting dirty images, which are obtained by assuming that the unsampled frequencies are zero, are shown in the middle column. These images are provided for illustration purposes only, since ADAM uses the *uv*-plane samples directly.

To test the ADAM reconstruction method, we use a low-resolution octantoid representation with 75 shape parameters. We also fit a scaling term, common to all observations. Usually it is a good idea to use scaling specific to each observation, but in this case we know that all the simulated observations are done in similar conditions, so the common scaling term is justified. The reconstructed shape is displayed in the right column in Fig. 5, with the same observation geometries as for the model images. The small-scale detail is lost, which is to be expected because of the added atmospheric noise and coarse instrument resolution. However, the bifurcated shape is well recovered despite the noisy data (note that we used ALMA data only). The computation time for this reconstruction was a few minutes. For real observations, complementary data are often provided by other observation methods e.g. disk-integrated photometric data are almost always available.

4.2. Radar data

The mathematical principles of the feasibility and uniqueness of the inversion of range-Doppler images are discussed in

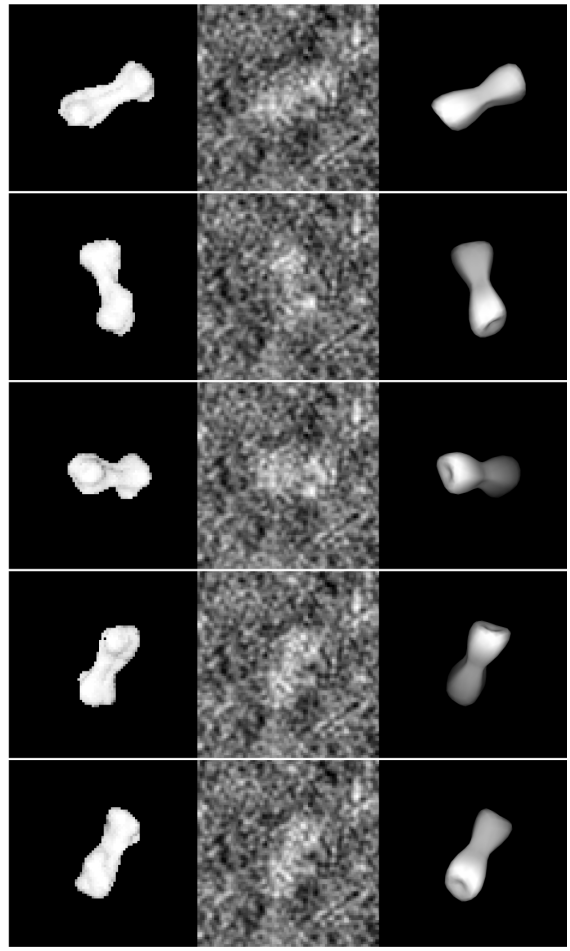

Fig. 5. Simulated, uncorrupted images with 5 mas pixel size (*left column*), observed dirty images generated with CASA (*middle*) and the reconstructed low-resolution shape model (*right*). Note that the *middle-column* images are not needed in inversion; we use the direct FT data instead. The images are what would be seen if the raw data were deconvolved for viewing purposes as is usually done for ALMA targets. The test shape model is from Ostro et al. (2000).

Viikinkoski & Kaasalainen (2014). Here we consider some practical issues related to shape reconstruction. While other imaging methods rely on detecting the radiation of the sun that is reflected or re-radiated from the asteroid, radar provides its own illumination, making it possible to observe an asteroid regardless of the position of the sun. Moreover, in contrast to the visible or infrared wavelengths, the frequencies used by the radar are not significantly distorted by the atmosphere. Additionally, the properties of the waveform may be carefully controlled to reveal structural details on the surface of the asteroid. These properties make it possible to obtain *data resolution* down to 10 m or less for near-Earth asteroids, but this does not immediately translate to the same *model resolution* because of the inverse problem (cf. the Itokawa example in Sect. 2.3).

Range-Doppler radar resolves an object both in the range and in the line-of-sight velocity that translates to the Doppler shift of the reflected pulse. The frequency spectrum may be extracted

by taking the fast Fourier transform of the pulses corresponding to a particular range gate. The actual hardware implementation and the signal processing are complicated as the detected signals are below the noise level of the instrument (Ostro et al. 2002). Fortunately, the technical specifics are not required for the actual shape reconstruction, since the radar performance may be modelled by the point-spread function of the system.

The point $p = (x, y, z)$ on the asteroid's surface can be transferred to the range-Doppler frame (r, D) by the linear mapping

$$r = (x\cos\phi + y\sin\phi)\sin\theta + z\cos\phi \quad (15)$$

$$D = \omega\sin\theta\,(x\sin\phi - y\cos\phi), \quad (16)$$

where ω is the rotation rate of the asteroid around the z-axis, and (θ, ϕ) are the spherical radar direction coordinates as seen from the asteroid. In this mapping, the range-Doppler radar image brightness L may be written as an integral over the asteroid surface S as

$$L(r, D) = \iint_S h_r\left[r - r(p)\right]\, h_D\left[D - D(p)\right]\, B(p)\, I(p)\,\mathrm{d}S, \quad (17)$$

where h_D and h_r are the point-spread functions of the radar system, corresponding to the Doppler-shifted frequency D and the range r, respectively. Here I is the visibility function, which is unity if the point is visible to the radar and zero otherwise. This form is similarly defined for all generalized projections (Kaasalainen & Lamberg 2006). The mapping $p \to (r, D)$ is unique, but its inverse is many-to-one, so the inherent information content of a range-Doppler image is considerably smaller than that of an optical image of similar resolution. Thus, while the nominal resolution provided by radar may be unmatched by any other instrument, the drawback of radar imaging is the difficulty of the interpretation of the images.

The radar scattering function is given by B, which is usually a simple cosine law

$$B(p) = C\left[\mu(p)\right]^n, \quad (18)$$

where μ is the cosine of the angle between the surface normal and the radar direction. The constants C and n measure the surface reflectivity and the specularity of scattering, respectively. The validity of Eq. (18) for modelling the microwave scattering from the asteroid's surface is a rather convoluted question. While the cosine law is quite simplified, it should be noted that as the reflected wave is formed in a complicated manner by the surface material whose properties and roughness are usually unknown, fully realistic modelling of the reflected wave is not computationally feasible. However, as in the other disk-resolved cases, most of the information is contained in the boundary contours and is thus independent of the scattering model used.

Assuming the asteroid is modelled as a polyhedron with triangular facets $\mathcal{T}$, the integral (17) may calculated separately for each facet, after projecting each triangle T_i as a triangle $\mathcal{P}T_i$ on the range-Doppler plane

$$L(r, D) = \sum_{T_i\in\mathcal{T}} B_i I_i \int_{\mathcal{P}T_i} h_r(r - r')\, h_D(D - D')\,\mathrm{d}r'\,\mathrm{d}D', \quad (19)$$

where we have assumed that the visibility I and the scattering law B are constant within a triangle.

Taking the Fourier transform on both sides, applying the convolution theorem, and writing $\mathcal{T}_i(u, v)$ for the sum over the edges of a Fourier transformed triangle as in Sect. 3, we obtain

$$\mathcal{L}(u, v) = \sum_{T_i\in\mathcal{T}} B_i\, I_i\, H_r(u)\, H_D(v)\, \mathcal{T}_i(u, v), \quad (20)$$

Fig. 6. Mid-resolution shape model of the asteroid 2000 ET_{70} reconstructed from radar images. Viewing directions are from the positive x, y, and z axes, respectively.

where $H_r(u)$ and $H_D(v)$ are the Fourier transforms of h_r and h_D, respectively.

Like any images, radar plots are seldom correctly aligned in some reference frame due to the errors in the centre of mass prediction, so the actual position of a radar image with respect to the two-dimensional projection of the model must be determined during the optimization. The task of image alignment is further complicated by the peculiar asymmetric structure of radar images, especially the bright leading edge, other possible ridges of strong reflectivity, and the fading farthest-range pixels. If the alignment information is unknown, it is usually a good idea to fit the image offsets to a fixed shape first, obtaining better initial positions that can be used in the shape optimization.

To demonstrate the reconstruction method, we make a fast ADAM model of the near-Earth asteroid 2000 ET_{70}. Our goal is to get a quick first look at an initial model (to be refined at will). The asteroid was observed during February 2012 at Arecibo and Goldstone observatories using 2380 and 8560 MHz range-Doppler radars (Naidu et al. 2013). The images obtained from Arecibo have a resolution of 15 m in range and 0.075 Hz in frequency. Goldstone images have a somewhat lower resolution, 15 to 75 m and 1 Hz, respectively. Our goal is to produce medium-scale detail in the reconstructed shape, so a typical model choice is an octantoid with $l_{\max} \sim 10$ and around 1500 facets. Our example is "first-result oriented" on purpose, so we assume no information about the instrument-specific distortions, or more importantly, knowledge about the point-spread functions determined by the instrument and the processing routines of the radar signal. Thus the point-spread function used in the shape reconstruction is simply the two-dimensional delta function.

For each data image, we fit, in addition to the shape parameters, the offset with respect to the model centre of mass and the reflectivity term in Eq. (18). The reconstructed middle-resolution shape is shown in Fig. 6 and the model fit to the data in Fig. 7. The shape model fits the boundary contours of the radar images satisfactorily, but there are some differences in the interior details. This is a consequence of the parametrization and facet size chosen for reconstruction. The interior could be reproduced in greater detail by choosing a different parametrization, for example locally adaptive subdivision surfaces, or by refining the positions of individual vertices. The model dimensions, shape features, and spin parameters agree with those published by Naidu et al. (2013; the spin parameters are identical except for a 2° difference in the pole latitude, well within error limits).

The main point of the initial low-to-middle resolution is that the speed of ADAM is considerable, and a detailed knowledge of the instrument or the surface scattering physics is not needed, so one obtains a first model very fast by just feeding in the images. The middle-resolution radar-based reconstruction (using 82 radar images) was computed in less than an hour on a standard laptop, and GPU programming can reduce the computation time significantly. This makes possible a broad sampling

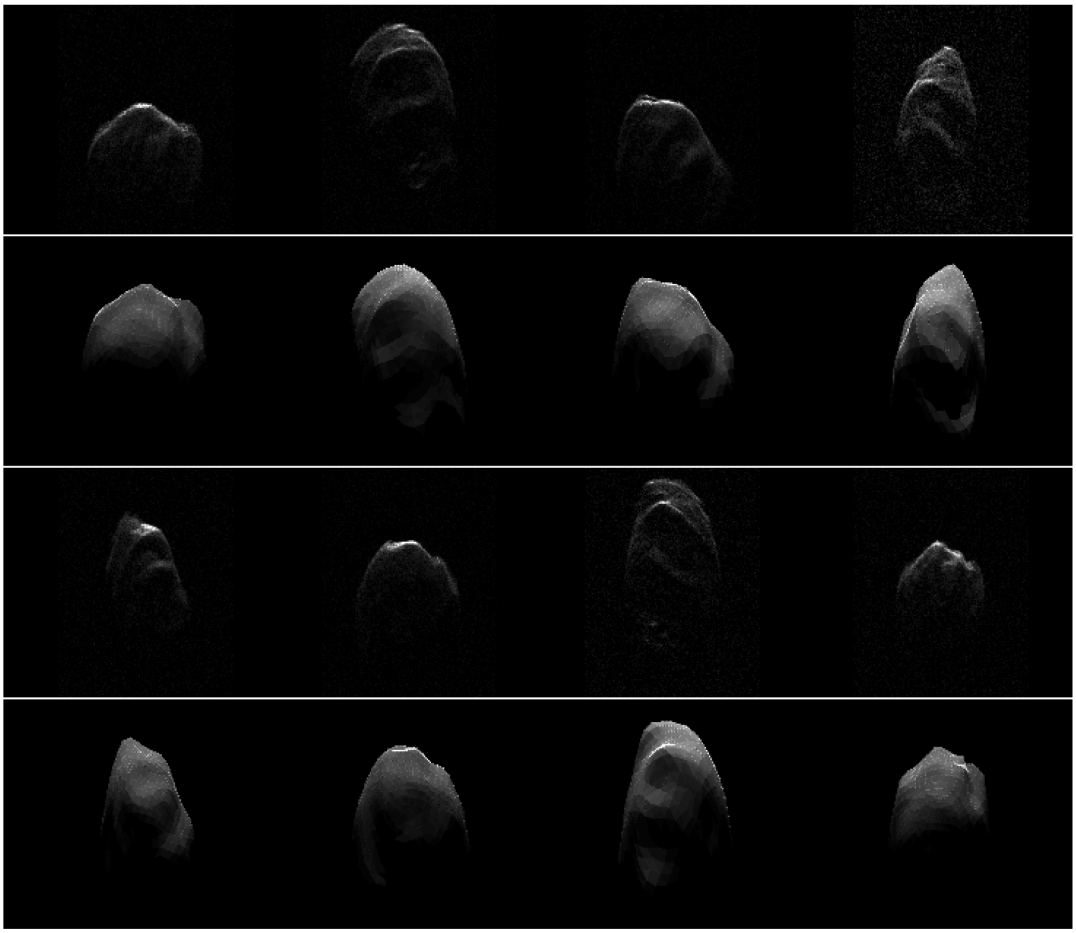

Fig. 7. Examples of range-Doppler images of the asteroid 2000 ET_{70} from Arecibo Observatory (rows 1 and 3) and corresponding simulated images from the mid-resolution model (rows 2 and 4). The contrast scale of the model image is somewhat modified to reveal inner image features.

of the parameter space or real-time experimenting with various models. Once a lower-resolution model has been adopted as the final frame, it is straightforward to refine it further. However, this requires accurate information about the point-spread and scatter functions.

4.3. Adaptive optics and other images

Model reconstruction from adaptive optics images in the Fourier approach is extensively covered in Viikinkoski & Kaasalainen (2014), along with an example of the reconstruction of the main belt asteroid Daphne from adaptive optics images and photometry (Fig. 2). Other imaging data may be incorporated into the framework using a similar approach. For instance, fly-by images are, from the viewpoint of the reconstruction algorithm, conceptually identical to the AO images. This is one of the attractions of ADAM: at the bare minimum, the user does not need to know anything about the images except their projection matrix and epochs.

We note that the photometric data were actually not even needed in reconstructing Daphne (except for a better estimate of the rotation period than with AO images only). The shape results with or without photometry are similar. This shows that even sparse AO data are well sufficient for modelling asteroid spin states and shapes in detail.

4.4. One-dimensional projection operators

In the regime between disk-integrated and disk-resolved observations there are one-dimensional operators that project the plane-of-sky onto a line. Typical examples are the continuous-wave (CW) Doppler spectra that measure the distribution of the reflected power in frequency only, and the fine guidance sensors (FGS) onboard the *Hubble* Space Telescope, measuring the brightness distribution along an instrument axis. One-dimensional projections are seldom sufficient for actual shape reconstruction, but they may contain useful information about the object's size or indications about the bifurcated structure (Kaasalainen & Viikinkoski 2012), and combined with other sources, they facilitate shape inversion.

In both examples, the measurement can be written in the form

$$S(x) = \int I(\xi, \eta)\, P(x - \xi\cos\gamma - \eta\sin\gamma)\, \mathrm{d}\xi\, \mathrm{d}\eta, \tag{21}$$

where $I(\xi, \eta)$ is the plane-of-sky brightness (optical or radar) distribution of an object, P is the point-spread function of the instrument, and the angle γ corresponds to the rotation of the sensor in the image plane. In Kaasalainen & Viikinkoski (2012), the integral was evaluated using a Monte Carlo method: the projected model was sprinkled with uniformly distributed sampling points, and the integral was approximated as a sum over the visible and illuminated sampling points. We demonstrate how the Fourier transform method can be used to interpret the integral as a tomographic operator on the Fourier plane.

Taking the Fourier transform on both sides and using the projection-slice theorem (a slice of a 2D FT along a line through the origin equals the 1D FT of the projection of the original 2D function onto a line in the same direction; see e.g. Bracewell 2003), we get

$$\mathcal{S}(f) = \mathcal{I}(f\cos\gamma, -f\sin\gamma)\,\mathcal{P}(f), \tag{22}$$

where the calligraphic characters denote the Fourier-transformed functions. Now it is obvious that $\mathcal{S}(f)$ is a slice of a Fourier-transformed brightness distribution along a line through the origin, multiplied with the Fourier transform of the point-spread function. Moreover, this means that the same algorithm may be used to fit both FGS and adaptive optics data, and similarly both CW Doppler data and the range-Doppler images. In other words, we extract a one-dimensional Fourier transform from the 2D model FT, and compare this with the 1D FT formed from the data in the same manner as in the full 2D case.

5. ADAM algorithm

The flowchart in Fig. 8 describes the workings of ADAM. More specifically, the algorithm may be divided in five distinct steps:

1. For each data image D_i and observation geometry $\mathcal{E}_i$, the two-dimensional Fourier transform $\mathcal{F}D_i(u, v)$ of D_i is sampled at a set of points $\{(u_{ij}, v_{ij})\}$, $j = 1 \dots N_i$, on the spatial frequency plane. The size of the set is chosen to correspond to the level of resolution. For pixel images, the transform can be computed with Eq. (10) when considering each pixel as a polygon, or with using fast Fourier transform functions for chosen grid points (but the time spent for $\mathcal{F}D_i(u, v)$ is irrelevant, as are most of the computations, for the trial models).
2. The shape support and resolution level (number of parameters) are chosen. The parameters are initialized such that the initial shape is a sphere approximately equal in size to the target.
3. For each observation geometry $\mathcal{E}_i$, the Fourier transform $\mathcal{F}M_i(u, v)$ of the corresponding projection image M_i of the model is calculated as described in the previous sections, together with the partial derivatives of $\mathcal{F}M_i(u, v)$ with respect to all optimized parameters. Ray-tracing, scattering or luminosity models, and coordinate transforms for the image plane are discussed in Kaasalainen et al. (2001), Kaasalainen (2011), and Viikinkoski & Kaasalainen (2014).
4. An objective function χ^2 is formed, with the square norm of the complex-valued FT fit error

$$\sum_i \sum_{j=1}^{N_i} \left\| \mathcal{F}D_i(u_{ij}, v_{ij}) - \mathrm{e}^{2\pi\mathrm{i}\left(o_i^x u_{ij} + o_i^y v_{ij}\right)}\, \mathcal{S}_i(u_{ij}, v_{ij})\, \mathcal{F}M_i(u_{ij}, v_{ij}) \right\|^2 + \sum_i \lambda_i \gamma_i^2 =: \chi^2, \tag{23}$$

where (o_i^x, o_i^y) is the offset between the data image D_i and the model image M_i, and, by the convolution theorem, $\mathcal{S}_i$ is the Fourier transform of the point-spread function of the imaging system. The γ_i represent various regularization terms defined above.

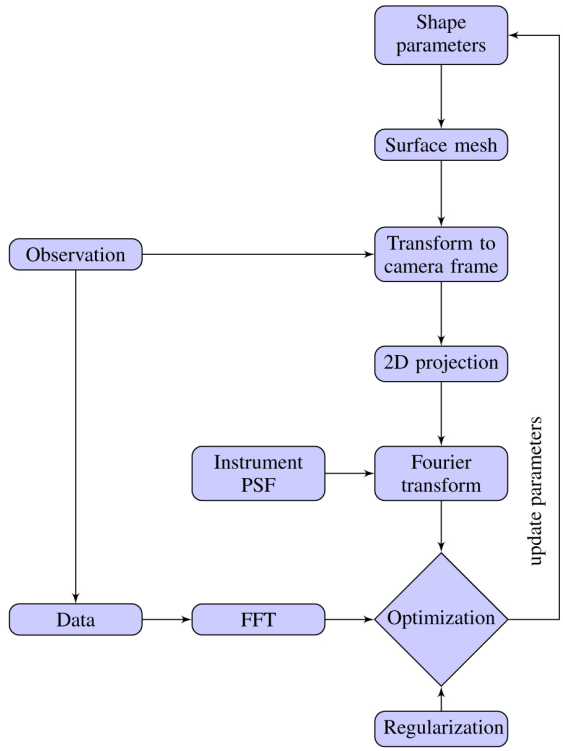

Fig. 8. ADAM optimization algorithm as a schematic for one image type.

For brevity, we have written only one data mode in Eq. (23); any number of modes with their goodness-of-fit functions can be added to the sum. These functions for photometry and silhouettes (occultations) are given in Kaasalainen et al. (2001), Kaasalainen (2011), and Viikinkoski & Kaasalainen (2014). The determination of the weights of the data modes (as λ_i for the regularization functions) is discussed in Kaasalainen (2011) and Kaasalainen & Viikinkoski (2012). Weights can be determined for any subsets of data (e.g. less reliable images) if necessary.

In addition, the intensity level of each data and model image must be normalized. Often it is enough to divide both model M_i and data image D_i by their respective mean intensities. Equivalently, writing

$$\chi^2 := \sum_{ij} \left\| \mathcal{D}_i(u_{ij}, v_{ij}) - \tilde{\mathcal{M}}_i(u_{ij}, v_{ij}) \right\|^2 + \lambda\gamma^2, \tag{24}$$

we have

$$\chi^2_{\mathrm{rel}} = \sum_{ij} \left\| \frac{\mathcal{D}_i(u_{ij}, v_{ij})}{\langle \|D_i\| \rangle} - \frac{\tilde{\mathcal{M}}_i(u_{ij}, v_{ij})}{\langle \|\tilde{M}_i\| \rangle} \right\|^2 + \lambda\gamma^2, \tag{25}$$

where the mean $\langle\cdot\rangle$ is taken over $\{(u_{ij}, v_{ij})\}$, $j = 1 \dots N_i$. However, sometimes it is better to allow the intensity level of each M_i to be a free parameter and use χ^2; this is useful in the case where the mean intensity of D_i is corrupted

by excessive noise in the image background (this is typical for range-Doppler images). This causes the $\chi^2_{\rm rel}$-based solution to have a slightly wrong size to compensate for the "diluted" normalized intensity level inside the actual object region of D_i.

5. The shape and spin parameters and the offsets (o_i^x, o_i^y) as well as the possible intensity level factors C_i minimizing χ^2 are determined with a suitable method such as the Levenberg-Marquardt algorithm. If there are several hundreds of parameters, as in the case of fitting all shape vertices directly (instead of using function series or control points) to produce maximal resolution, the conjugate gradient method is efficient (Kaasalainen et al. 2001).

6. Conclusions and discussion

The ADAM algorithm can handle radar data, images, interferometry (also in the thermal infrared), photometry, and occultations separately or in combinations. The ADAM procedure consists of a number of modules, and there are various options for each module that are customized to the end-user (e.g. the adopted optimization method, regularization functions, shape support and mesh structure, ray-tracing method, coordinate system, luminosity/scatter model, image formats, etc.). In this sense, ADAM is a toolbox and a set of building blocks rather than a ready-made program.

The main idea behind ADAM is the efficient use of the Fourier transform in handling both images and one-dimensional projection data. Fourier analysis has long been used in e.g. image compression because it conveniently captures the essential information in a hierarchy of resolution. In the same vein, the FT approach in ADAM is ideal for producing models of desired levels of resolution, especially in the low- to medium-resolution category. In this framework, the goodness-of-fit function between the model and the data is easy to compute and use in optimization. In addition, with this method, its convergence properties are more robust than if the images are used directly. In fact, one does not necessarily even have to look at the images or know much about the instrument that produced them. An analogy of this paradox is the simple one-dimensional problem of realigning two phase-shifted copies of a dual-frequency signal. If one does this by minimizing the signal difference by optimizing the shift in the original amplitude space, there are multiple local minima, but in frequency space the offset is found immediately.

Despite its automatic character, ADAM should not be used as a black box: asteroid reconstruction is a complicated inverse problem, and one should be familiar with its mathematical principles to understand the limitations and information content of the data sources.

Acknowledgements. This work was supported by the Academy of Finland project "Modelling and applications of stochastic and regular surfaces in inverse problems" and the CoE in inverse problems research. The work of J.Ď. was supported by the grant GACR P209/10/0537 of the Czech Science Foundation. We thank Jean-Luc Margot for providing the radar images of asteroid 2000 ET_{70}.

Appendix A: Sample ADAM functions

In order to make the structure of ADAM more concrete, we show an example of how the program is divided into sub-routines. We consider only the part of the program that computes the heat flux density of an object and its Jacobian (i.e. the partial derivatives of each modelled flux data point w.r.t. the free parameters), as all the other modules are structurally similar. In the case of optical images, the flux is replaced by brightness from scattering; for radar, by the signal strength in the range-Doppler plane.

The partial derivatives w.r.t. the shape parameters are initially calculated with respect to the vertex coordinates, making the routines independent of the parametrization we used. The Jacobian is determined using the chain rule only in the final phase. The functions are complex-valued, since the fitting is done on the frequency plane. In the optimization, the data are divided into real and imaginary parts and fitted separately. Usually, the Levenberg-Marquardt or the conjugate gradient method is used to optimize the χ^2-fit.

Three different coordinates systems are used in ADAM: the asteroid-centric coordinate frame with coordinate axes fixed to the asteroid, the asteroid-centric inertial frame, and the camera frame, which is determined by the instrumental orientation geometry. The plane-of-sky view of an asteroid is obtained by projecting the asteroid in the camera frame to the xy-plane.

The Jacobian and the vector, consisting of simulated values corresponding to the observations, are computed using the following subroutines:

- `Generate_HF_Matrix` calls the subroutine `Calc_Heat_Flux` for each observation, and then combines the Jacobian submatrices into a full Jacobian matrix corresponding to all the observations.
- `Calc_Heat_Flux` calculates the Fourier transform of the two-dimensional plane-of-sky flux density and its partial derivatives by calling the subroutines `Calc_Temp`, `Rot_Matrix`, `Cam_Matrix`, `Calc_Vis` and `Calc_FT`. After the flux density of each facet is determined, the routine transforms the triangular mesh to the camera frame and projects the visible part of the mesh onto the xy-plane by discarding the z-coordinate. Finally, each vertex is transformed to the frequency plane using the `Calc_FT` subroutine and the contributions of the Fourier-transformed facets are summed.
- `Calc_Temp` determines the temperature of the facets corresponding to the observation geometry, using the FFT method. The partial derivatives of the temperature with respect to the shape parameters are also calculated. This subroutine also calls subroutines `Rot_Matrix` and `Calc_Vis`.
- `Rot_Matrix` calculates the rotation matrix needed to transform the object to the inertial frame. The rotation matrix is determined by the spin vector and the observation time.
- `Cam_Matrix` determines the matrix needed to transform the inertial frame to the camera frame. This depends on the instrument location and orientation. The z-coordinate codes the relative distance from the instrument.
- `Calc_Vis` determines the visibility of facets using ray-tracing. In contrast to the optical case, a facet can be visible to the observer even if it is not illuminated by the sun.
- `Calc_FT` calculates the Fourier transform of a triangle projected onto the xy-plane together with the corresponding partial derivatives.

The most important setup factors determining the computation time of ADAM are the numbers of facets and data points (the number of images and their pixels). The computation time increases approximately linearly with both numbers. The cost of actual optimization steps increases superlinearly with the number of free parameters, but with large data sets (such as the radar example above) most of the computation is spent on determining function values and their partial derivatives with respect to the vertex coordinates. In such cases, the number of shape

parameters is not critical for the computational cost in the mid-resolution regime, so one is free to choose a number that best corresponds to the resolution level (and set the number of facets accordingly). When the data set is small, the computation time is short in any case, and the model is likely to be low resolution, so again the number of parameters is not an issue. The cost of visibility determination by ray-tracing is insignificant as the potential blocker facets can be precomputed (Kaasalainen & Torppa 2001).

The shape reconstruction from observations is an easily parallelizable problem. There are two obvious levels of parallelism: each observation can be calculated independently; or, within each observation, the contribution of each facet may be determined simultaneously. The best choice depends on the computer's architecture. The observation-level parallelism may be easily exploited using the MATLAB parallel computing toolbox, or more effectively by using the OpenMP API in the C language. The reduction in execution time scales almost linearly with the number of CPU cores. This is the approach currently implemented in ADAM.

While it is possible to implement facet-level parallelism on the CPU by dividing the facet computations between several CPU cores, a more natural approach is to use one thread per facet. This kind of implementation is inefficient on the CPU, since the thread-switching latency is high compared to the running time of a thread. However, the ability of the GPU to run thousands of lightweight threads simultaneously combined with the virtually costless thread switching makes it possible to attain orders of magnitude faster computation than with CPU. We will implement GPU acceleration in ADAM using the Nvidia CUDA programming platform.

References

Bracewell, R. 2003, Fourier analysis and imaging (Springer)
Carry, B., Kaasalainen, M., Merline, W. J., et al. 2012, Planet. Space Sci., 66, 200
Ďurech, J., & Kaasalainen, M. 2003, A&A, 404, 709
Ďurech, J., Grav, T., Jedicke, M., Kaasalainen, M., & Denneau, L. 2006, Earth Moon Planet., 97, 179
Ďurech, J., Vokrouhlický, D., Baransky, A. R., et al. 2012, A&A, 547, A10
Ďurech, J., Carry, B., Delbo, M., Kaasalainen, M., & Viikinkoski, M. 2015, Asteroids IV [arXiv:1502.04816]
Kaasalainen, M. 2004, A&A, 422, L39
Kaasalainen, M. 2011, IPI, 5, 37
Kaasalainen, M., & Ďurech, J. 2006, Proc. IAU, 2, 151
Kaasalainen, M., & Ďurech, J. 2013, in Asteroids, ed. V. Badescu (Berlin, Heidelberg: Springer), 131
Kaasalainen, M., & Lamberg, L. 2006, Inverse Probl., 22, 749
Kaasalainen, M., & Torppa, J. 2001, Icarus, 153, 24
Kaasalainen, M., & Viikinkoski, M. 2012, A&A, 543, A97
Kaasalainen, M., Torppa, J., & Muinonen, K. 2001, Icarus, 153, 37
Kaasalainen, M., Mottola, S., & Fulchignoni, M. 2002, Asteroids III, eds. W. F. Bottke Jr., A. Cellino, P. Paolicchi, & R. P. Binzel (Tucson: University of Arizona Press), Asteroids III, 139
Kaasalainen, M., Pravec, P., Krugly, Y. N., et al. 2004, Icarus, 167, 178
Kobbelt, L. 2000, in Proc. 27th annual conference on Computer graphics and interactive techniques (ACM Press/Addison-Wesley Publishing Co.), 103
Labeyrie, A., Lipson, S. G., & Nisenson, P. 2006, An introduction to optical stellar interferometry (Cambridge University Press)
Loop, C. 1987, Master's Thesis, University of Utah
Naidu, S. P., Margot, J.-L., Busch, M. W., et al. 2013, Icarus, 226, 323
Nesvorný, D., & Vokrouhlický, D. 2008, AJ, 136, 291
Nolan, M., Bramson, A., & Magri, C. 2014, in Asteroids, Comets and Meteors, Proc. Conf., eds. K. Muinonen, et al.
Ostro, S. J., Scott, R., Hudson, et al. 2000, Science, 288, 836
Ostro, S. J., Hudson, R. S., Benner, L. A., et al. 2002, Asteroids III (Tucson: Univ. of Arizona Press), 151
Ostro, S. J., Benner, L. A. M., Magri, C., et al. 2005, Meteoritics, 40, 1563
Viikinkoski, M., & Kaasalainen, M. 2014, IPI, 8, 885

Publication IV

Viikinkoski M., Kaasalainen M., Ďurech J. and Carry B. et al., "VLT/SPHERE- and ALMA-based shape reconstruction of asteroid (3) Juno," *Astronomy & Astrophysics* 581 L3 (2015)

Reproduced with permission from Astronomy & Astrophysics, ©ESO 2015

A&A 581, L3 (2015)
DOI: 10.1051/0004-6361/201526626
© ESO 2015

Astronomy & Astrophysics

L E

VLT/SPHERE- and ALMA-based shape reconstruction of asteroid (3) Juno⋆

M. Viikinkoski[1], M. Kaasalainen[1], J. Ďurech[2], B. Carry[3,4], M. Marsset[5,6], T. Fusco[6,7], C. Dumas[5], W. J. Merline[8], B. Yang[5], J. Berthier[3], P. Kervella[9,10], and P. Vernazza[6]

[1] Department of Mathematics, Tampere University of Technology, PO Box 553, 33101 Tampere, Finland
e-mail: matti.viikinkoski@tut.fi
[2] Astronomical Institute, Faculty of Mathematics and Physics, Charles University in Prague, V Holešovičkách 2, 18000 Prague, Czech Republic
[3] ACME, IMCCE, UMR 8028 du CNRS, UPMC, Université de Lille 1, 77 Av. Denfert-Rochereau, 75014 Paris, France
[4] Laboratoire Lagrange, UMR 7293 CNRS, UNS, Observatoire de la Côte d'Azur, 06304 Nice, France
[5] European Southern Observatory (ESO), Alonso de Còrdova 3107, 1900 Casilla Vitacura, Santiago, Chile
[6] Aix-Marseille University, CNRS, LAM (Laboratoire d'Astrophysique de Marseille) UMR 7326, 13388 Marseille, France
[7] ONERA – Optics Department, 29 avenue de la Division Leclerc, 92322 Chatillon Cedex, France
[8] Southwest Research Institute, 1050 Walnut St., #300 Boulder, CO 80302, USA
[9] Unidad Mixta Internacional FCA (UMI 3386), CNRS/INSU & Universidad de Chile, Las Condes, Santiago, Chile
[10] LESIA (UMR 8109), Observatoire de Paris, CNRS, UPMC, Univ. Paris-Diderot, PSL, 5 place Jules Janssen, 92195 Meudon, France

Received 28 May 2015 / Accepted 12 August 2015

ABSTRACT

We use the recently released Atacama Large Millimeter Array (ALMA) and VLT/SPHERE science verification data, together with earlier adaptive-optics images, stellar occultation, and lightcurve data to model the 3D shape and spin of the large asteroid (3) Juno with the all-data asteroid modelling (ADAM) procedure. These data set limits on the plausible range of shape models, yielding reconstructions suggesting that, despite its large size, Juno has sizable unrounded features moulded by non-gravitational processes such as impacts.

Key words. instrumentation: interferometers – instrumentation: adaptive optics – methods: numerical – minor planets, asteroids: individual: (3) Juno

1. Introduction

Despite a few early adaptive-optics images suggesting an intriguing shape (Baliunas et al. 2003), the asteroid (3) Juno remains relatively unobserved. The release of the ALMA science verification data[1] of Juno (ALMA Partnership et al. 2015) allows us, for the first time, to explore the viability of the shape reconstruction of asteroids from disk-resolved thermal infrared observations. We also use other data to test methods and procedures that employ a wide spectrum of various data sources. In particular, we use the science verification data from SPHERE, the recently commissioned extreme adaptive-optics (AO) system (Beuzit et al. 2008) mounted at the European Southern Observatory (ESO) Very Large Telescope (VLT). We survey the available observations of Juno that can be used for shape reconstruction using the recently introduced modeling (ADAM) package (Viikinkoski et al. 2015) and present a model based on ALMA data, lightcurves, AO images, and stellar occultations.

We discuss the reliability of the reconstruction by using different shape representations and data subsets. We show that all plausible shape-model variations are quite similar and suggest that, despite its large diameter of about 250 km, Juno has sizable unrounded and non-equilibrium features. This is in contrast to the very rounded shapes of the largest asteroids (1) Ceres, (2) Pallas, and (4) Vesta witnessed by the Dawn mission (Russell et al. 2012) or imaged from the ground and *Hubble* Space Telescope (Thomas et al. 2005; Carry et al. 2008, 2010a), but typical of large asteroids that present large flat facets or concavities as do (21) Lutetia, (52) Europa, or (511) Davida (Conrad et al. 2007; Carry et al. 2010b; Merline et al. 2013).

2. Data modes

2.1. Submillimeter interferometry

Juno was observed with ALMA on 2014 Oct. 19 using between 27 and 33 antennas, thereby providing projected baselines between 26 m and 13 km. At the observed frequencies of 224, 226, 240, and 242 GHz, this corresponds to angular resolutions as high as 0.021″, or about 30 km projected at the distance of Juno. A total of ten different epochs spread over 4.4 h were acquired, and they correspond to about 60%

⋆ Based on observations collected at the European Southern Observatory, Paranal, Chile (prog. ID: 60.A-9379, 086.C-0785), and at the W. M. Keck Observatory, which is operated as a scientific partnership among the California Institute of Technology, the University of California and the National Aeronautics and Space Administration. The Observatory was made possible by the generous financial support of the W.M. Keck Foundation.

[1] https://almascience.eso.org/alma-data/science-verification

Table 1. Range to observer (Δ, in au) and longitude (λ) and latitude (β) of the sub-Earth point (SEP) of the adaptive-optics images used for the shape reconstruction.

Obs. time	Instrument	Δ (au)	SEP$_\lambda$ (°)	SEP$_\beta$ (°)	Fig.
1996-10-15 08h	ADOPT	1.12	208	8	4a
2001-12-26 15h	NIRC2	1.59	248	−34	4b
2010-12-13 07h	NACO	2.41	342	−17	4c
2010-12-13 08h	NACO	2.41	292	−17	4d
2014-12-09 07h	SPHERE	1.52	218	−41	4e
2015-01-30 06h	SPHERE	1.33	223	−46	4f
2015-01-30 08h	SPHERE	1.33	123	−46	4g
2015-01-31 05h	SPHERE	1.34	154	−47	4h

of its rotation period, each epoch having several hundreds of thousands points in the visibility function plane. As stated by ALMA Partnership et al. (2015), each epoch on Juno lasted for 18 min, during which time Juno rotated 15°. The smearing effect is, however, limited to about 21 mas.

The ALMA data are samples of the Fourier transform (FT) of sky brightness. Unlike most other ALMA users, we can use the raw FT data directly for reconstruction. The "clean" ALMA images obtained by various deconvolution and self-calibration processes inevitably lose and distort some of the original information. On the other hand, there usually are residual antenna-based phase errors in the raw ALMA data (Hezaveh et al. 2013). We discuss the effect of this in Sect. 4.

2.2. Adaptive-optics images

The first adaptive-optics images of Juno were obtained at Mt. Wilson observatory in the 1990s with the 100-inch telescope fitted with the ADOPT adaptive-optics system, providing an angular resolution of 0.080″ at 800 nm. These observations are documented in Baliunas et al. (2003). The original data were no longer available in a usable format, so we used the images directly from the paper. The image scale in the paper was unknown, so we included it in the optimization as a free parameter.

In 2001 and 2010, we also acquired near-infrared disk-resolved images of Juno with the first-generation AO cameras NIRC2 (Wizinowich et al. 2000; van Dam et al. 2004) on the W. M. Keck II telescope and NACO (Lenzen et al. 2003; Rousset et al. 2003) on the ESO VLT. The angular resolution of these data is of 0.045 and 0.055″, respectively.

We also present here data we obtained during the science verification[2] of the recently commissioned second-generation SPHERE AO system, mounted at the VLT (Beuzit et al. 2008). SPHERE is an instrument designed for exoplanet detection and characterization by high-angular and high-contrast imaging and spectro-imaging. The AO module (Fusco et al. 2006) was therefore designed to provide extremely high fidelity correction, but limited to very bright targets ($R \sim 11$). We used the classical imaging mode of SPHERE (IRDIS, Dohlen et al. 2008) to image the apparent disk of Juno. The different data sets and observation times are summarized in Table 1. Although the images of Juno obtained with NACO and SPHERE theoretically have the same angular resolution, since they were taken at the same wavelength with the same aperture, the higher Strehl ratio achieved by the latter provides more detailed images (Fig. 4).

[2] http://www.eso.org/sci/activities/vltsv/spheresv.html

2.3. Optical lightcurves

It has been shown (Kaasalainen et al. 2001) that a three-dimensional convex model can be reconstructed with lightcurves from various observation geometries. However, recovering non-convex features reliably is seldom possible with lightcurves alone (Ďurech & Kaasalainen 2003). On the other hand, lightcurves are crucial for enabling and completing the reconstruction when only a few disk-resolved observations are available (Viikinkoski & Kaasalainen 2014; Viikinkoski et al. 2015). For Juno, 37 relative-magnitude lightcurves were obtained in the years 1954–1991. They are available in an electronic format in the Asteroid Photometric Catalogue[3] or in the Database of Asteroid Models from Inversion Techniques (DAMIT)[4] (Ďurech et al. 2010). Compared to the recent SPHERE and ALMA observations, even the latest lightcurve is more than 20 years old. Therefore, we acquired a lightcurve in April 2015 at the 1 m telescope of the Pic-du-Midi Observatory, France.

2.4. Stellar occultation

There are six stellar occultation events listed by Dunham et al. (2014) and publicly available on the Planetary Data System (PDS)[5]. However, only the occultation from 1979 with 16 full chords can be used for recovering an almost complete silhouette, although its timings are not as accurate as is customary nowadays. Ďurech et al. (2011) used this dataset to scale the convex model of Juno reconstructed from lightcurves by Kaasalainen et al. (2002).

3. Methods

We used the ADAM algorithm (Viikinkoski & Kaasalainen 2014; Viikinkoski et al. 2015) for the shape and spin reconstruction. ADAM enables an easy combining and weighting of various data types. In the case of Juno, the ALMA visibility data were combined with disk-integrated photometry and with the adaptive-optics images, and checked against the occultation data. The last did not improve the reliability of the solution or provide more information, so we only used them as a consistency check as depicted in Fig. 5.

Not all the apparent features present in the Mt. Wilson data could be accommodated in any acceptable solution (as defined in Kaasalainen 2011; Kaasalainen & Viikinkoski 2012) based on all the data. This is probably due to non-corrected aberrations by the early AO equipment and/or artifacts introduced by the deconvolution. Indeed, unlike Mistral (Mugnier et al. 2004), the algorithm we used to deconvolve the images from NACO, NIRC2, and SPHERE, the Lucy-Richardson deconvolution of Baliunas et al. (2003) is not optimized for objects with sharp boundaries.

We used both subdivision surfaces and octantoid parametrization for shape representations (Viikinkoski et al. 2015). Based on a global parametrization by spherical harmonics, octantoids produce smooth curved surfaces, while the subdivision surfaces, together with the regularization we use, are characterized by sharper local features. By using two different shape supports, we strove to distinguish the model features caused by the shape representation from those actually

[3] http://asteroid.astro.helsinki.fi/

[4] http://http://astro.troja.mff.cuni.cz/projects/asteroids3D

[5] http://sbn.psi.edu/pds/resource/occ.html

supported by the data. Similarly, we checked the effect of data sources by observing the model variations under varying data subset combinations.

For thermal modeling, we used a simple, semi-analytical FFT-based approach (Nesvorný & Vokrouhlický 2008; Viikinkoski & Kaasalainen 2014). While it lacks the sophistication of more detailed models, it is fast and sufficient for recovering the model boundaries, which are the most important feature for shape reconstruction. Also, owing to the very low thermal inertia of Juno of $5\,\mathrm{J\,m^{-2}\,s^{-0.5}\,K^{-1}}$ (Mueller & Lagerros 1998), the differences between our approach and more complex ones are expected to remain small.

4. Results

Most of the disk-resolved data (especially those from ALMA and SPHERE) were obtained at viewing geometries restricted to Juno's southern hemisphere, so the northern parts of the model are less constrained. Figure 3 shows ALMA deconvolved images vs. the ALMA-dominated shape model on the plane of sky. This is not the actual data fit, but a visual aid for illustration purposes. We used the calibrated visibility data instead of the ALMA deconvolved images (that are formed by a strongly iterative separate process and additional assumptions) in the primary reconstruction, and the model images are given as visible wavelength projections that look essentially the same as the thermal ones due to the low thermal inertia. ALMA-dominated models are shown in the first two rows of Fig. 1. These already emphasize the lopsided or lozenge-like shape hinted at by the lightcurve-only model of Kaasalainen et al. (2002). The viewing direction of the Mt. Wilson AO image is almost in the equatorial plane of the asteroid and, despite its lower reliability, provides useful additional information not present in the thermal data.

The model obtained from the full dataset is depicted in the last row of Fig. 1. Comparison of the model with optical lightcurves, AO images, ALMA reconstructed images, and stellar occultation are presented in Figs. 2, 4, 3, and 5, respectively. This model can be downloaded at the DAMIT web site.

There are 11 diameter and 23 mass estimates for (3) Juno in the literature (see Appendix), giving an average diameter of 249 ± 7 km and an average mass of $2.68 \pm 0.24 \times 10^{19}$ kg. Our determination of 249 ± 5 km corresponds exactly to this average diameter. Using this estimate, we find a density of $3.32 \pm 0.40\,\mathrm{g\,cm^{-3}}$. Compared with the grain density of L ordinary chondrites (Consolmagno et al. 2008), this implies a porosity of $7 \pm 1\%$ and a null macroporosity of $2 \pm 2\%$, which is consistent with an intact internal structure. As shown in Table 2, the spin determination by Kaasalainen et al. (2002) and Ďurech et al. (2011) agrees very well with the result here, and the study of AO images from Lick observatory by Drummond & Christou (2008) provides an independent confirmation of this spin location. Although the topography of the northern hemisphere is less constrained than the southern latitudes, the vertical dimension seems stable under shape support and data subset variations.

We also checked the effect of ALMA self-calibration on the quality of shape reconstruction. During self-calibration, the antenna phase errors causing deteriorated image quality are corrected iteratively, alternating between the frequency and the image domain (ALMA Partnership et al. 2015). The model reconstructed from the self-calibrated, deconvolved images instead of the raw data revealed no additional detail, at least for this level of resolution (even when using ALMA data only), so the self-calibration is not a major concern here. The best way to facilitate full high resolution in shape reconstruction from future full-baseline ALMA data is to let the antenna gains be free parameters (Hezaveh et al. 2013), so that the optimization of the shape, spin, and the antenna parameters is done simultaneously. This prevents the introduction of potentially spurious information into the shape solution.

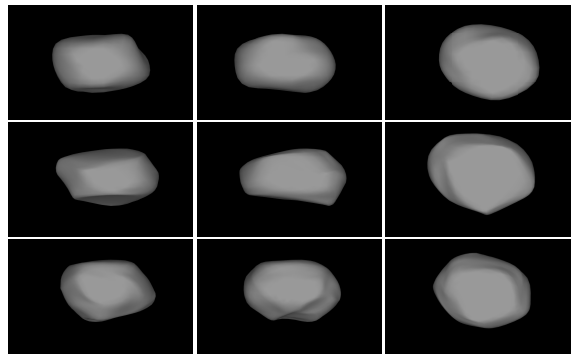

Fig. 1. Plausible variations of reconstruction. Models are from: ALMA and lightcurves – octantoid (*top*); subdivision surfaces: combined AO (Mt. Wilson), ALMA and lightcurve data (*middle*); full data set (*bottom*). Viewing directions are from the positive x-, y-, and z-axes.

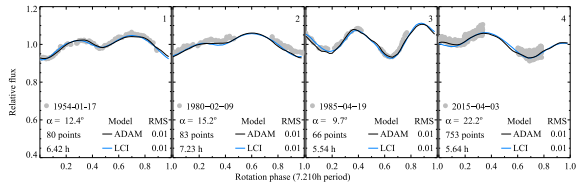

Fig. 2. Examples of the synthetic lightcurves generated with current ADAM shape model and the lightcurve model (LCI) by Kaasalainen et al. (2002) compared with photometric observations on four epochs. Also the phase angle (α) and the duration of observations are displayed. The models are hardly distinguishable.

Table 2. Comparison of different models.

	ADAM	Dru08	Dur11
λ (°)	103 ± 4	118 ± 13	103 ± 5
β (°)	$+22 \pm 4$	$+30 \pm 13$	$+27 \pm 5$
P (h)	3091 ± 100	–	3100 ± 100
a (km)	282 ± 5	298 ± 6	304 ± 29
b (km)	249 ± 5	237 ± 4	286 ± 29
c (km)	220 ± 5	222 ± 6	207 ± 29
D (km)	249 ± 5	250 ± 9	252 ± 29
a/b	1.13 ± 0.04	1.26 ± 0.03	1.06 ± 0.15
b/c	1.13 ± 0.05	1.07 ± 0.03	1.39 ± 0.21

Notes. Spin (ECJ2000 longitude λ and latitude β) and dimensions (volume-equivalent diameter D and tri-axial ellipsoid diameters a, b, c along principal axes of inertia) of Juno derived with ADAM compared with the results from Drummond & Christou (2008) from tri-axial ellipsoid modeling of adaptive-optics images obtained at Lick 3-m Shane telescope and from Ďurech et al. (2011). The leading digits of the period P are 7.2095 and only the trailing digits are displayed in the table.

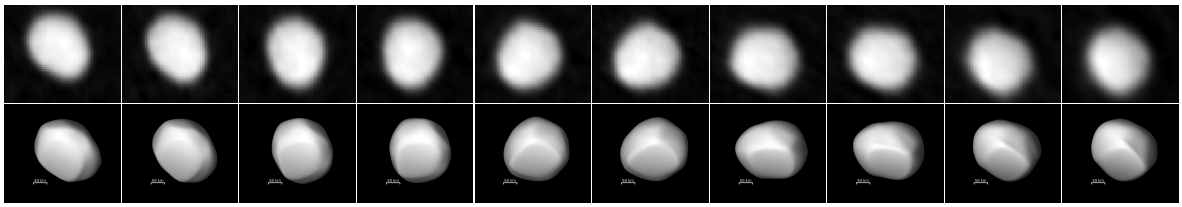

Fig. 3. Comparison of the ALMA deconvolved images (*top*) to the ALMA+lightcurve model (*bottom*). The scalebar corresponds to 50 km.

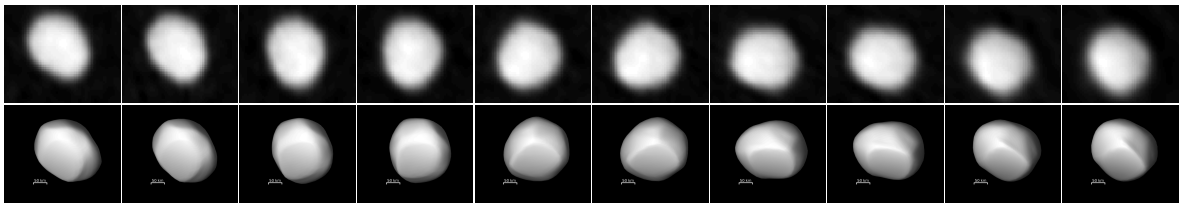

Fig. 4. Adaptive-optics images used for reconstruction (*top*) and corresponding model views (*bottom*). See Table 1 for observing conditions and instruments. The scattering law used for the shading exaggerates surface features.

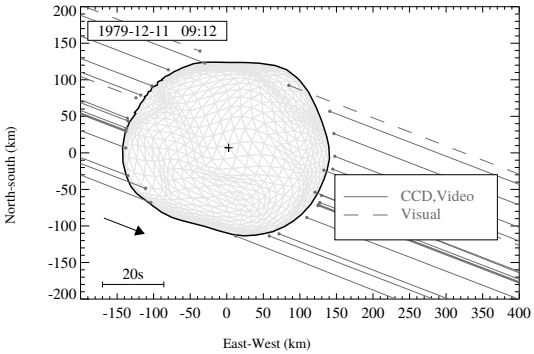

Fig. 5. Comparison of the shape model with the chords from the stellar occultation of 1979. The shape model created without the occultation data is very consistent with the occultation chords, although Juno rotated some 13° during the event.

5. Conclusions

We have reconstructed the shape and spin of (3) Juno from combined thermal interferometry, optical photometry, and adaptive-optics images, and checked its consistency with occultation data. Different and independent shape supports and regularization methods generate similar shapes, suggesting that the main features are actually present in the data, so are not artifacts of the reconstruction. Owing to the restricted observing geometries, the southern hemisphere of Juno is described here better than its northern latitudes. Juno seems to reside in the volumetric and structural transition region from dwarf planets to large and medium-sized asteroids. Its global shape features are apparently molded by other than gravitational processes (likely impacts).

While the angular resolution currently delivered by ALMA is comparable to that of adaptive-optics-fed cameras mounted on 8–10 m telescopes, ALMA will provide a resolution close to 5 mas (Busch 2009) once at full capability. This will convert ALMA into one of the most important sources of disk-resolved asteroid data, alongside adaptive-optics images and range-Doppler radar echoes.

Acknowledgements. This paper makes use of the following ALMA data: ADS/JAO.ALMA#2011.0.00013.SV. ALMA is a partnership of ESO (representing its member states), NSF (USA) and NINS (Japan), together with NRC (Canada) and NSC and ASIAA (Taiwan), in cooperation with the Republic of Chile. The Joint ALMA Observatory is operated by ESO, AUI/NRAO and NAOJ. This research made use of the Keck Observatory Archive (KOA), which is operated by the W. M. Keck Observatory and the NASA Exoplanet Science Institute (NExScI), under contract with the National Aeronautics and Space Administration. The authors wish to recognize and acknowledge the very significant cultural role and reverence that the summit of Mauna Kea has always had within the indigenous Hawaiian community. We are most fortunate to have the opportunity to conduct observations from this mountain. This work was supported by the Centre of Excellence in Inverse Problems Research (Academy of Finland). The work of J.D. was supported by the research grant GACR 15-04816S of the Czech Science Foundation.

Appendix A: Diameter and mass estimates from the literature

There are 11 diameter estimates of (3) Juno in the literature, obtained with a wide variety of techniques (see Fig. A.1 and Barnard 1900; Morrison & Zellner 2007; Tedesco et al. 2004; Millis et al. 1981; Baier & Weigelt 1983; Drummond & Christou 2008; Ryan & Woodward 2010; Ďurech et al. 2011; Usui et al. 2011; Masiero et al. 2012). We determine the average value here following the method by Carry et al. (2012), by rejecting all the estimates that do not fall within one standard deviation of the average value, then by recomputing the average without these values.

Similarly, there are 23 mass estimates for (3) Juno, obtained by studying the orbital deflection of other minor planets (see Fig. A.2 and Chernetenko & Kochetova 2002; Kochetova 2004; Pitjeva 2004, 2005, 2010, 2013; Konopliv et al. 2006, 2011; Baer et al. 2008, 2011; Folkner et al. 2009; Fienga et al. 2010, 2011, 2013, 2014; Somenzi et al. 2010; Zielenbach 2011; Kuchynka & Folkner 2013; Goffin 2014; Kochetova & Chernetenko 2014). Because there is no known satellite of Juno, mass determination relies on these long-range interactions.

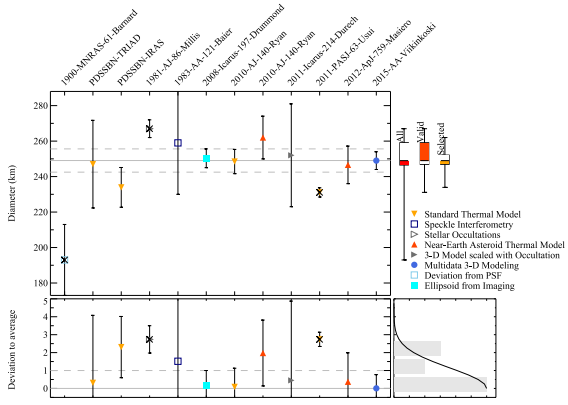

Fig. A.1. Diameter estimates of (3) Juno gathered from the literature. The dashed lines depict 3% deviation from the mean.

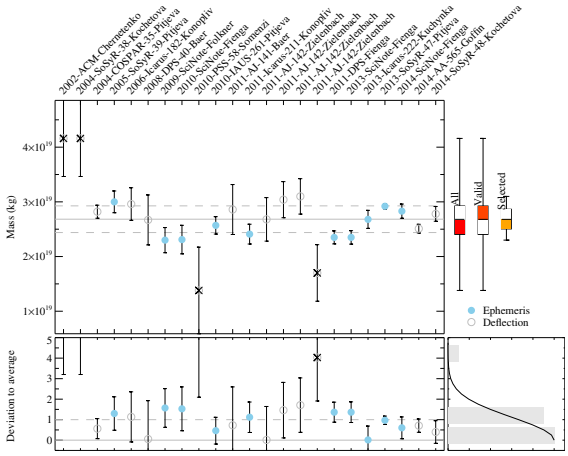

Fig. A.2. Mass estimates of (3) Juno gathered from the literature. The dashed lines depict 10% deviation from the mean.

References

ALMA Partnership, Hunter, T. R., Kneissl, R., et al. 2015, ApJ, 808, L2
Baer, J., Milani, A., Chesley, S. R., & Matson, R. D. 2008, in BAAS, 40, 493
Baer, J., Chesley, S. R., & Matson, R. D. 2011, AJ, 141, 143
Baier, G., & Weigelt, G. 1983, A&A, 121, 137
Baliunas, S., Donahue, R., Rampino, M. R., et al. 2003, Icarus, 163, 135
Barnard, E. E. 1900, MNRAS, 61, 68
Beuzit, J.-L., Feldt, M., Dohlen, K., et al. 2008, Proc. SPIE, 7014, 701418
Busch, M. W. 2009, Icarus, 200, 347
Carry, B., Dumas, C., Fulchignoni, M., et al. 2008, A&A, 478, 235
Carry, B., Dumas, C., Kaasalainen, M., et al. 2010a, Icarus, 205, 460
Carry, B., Kaasalainen, M., Leyrat, C., et al. 2010b, A&A, 523, A94
Carry, B., Kaasalainen, M., Merline, W. J., et al. 2012, Planet. Space Sci., 66, 200
Chernetenko, Y. A., & Kochetova, O. M. 2002, in Asteroids, Comets, and Meteors: ACM 2002, ed. B. Warmbein, ESA SP, 500, 437
Conrad, A. R., Dumas, C., Merline, W. J., et al. 2007, Icarus, 191, 616
Consolmagno, G., Britt, D., & Macke, R. 2008, Chemie der Erde/Geochemistry, 68, 1
Dohlen, K., Langlois, M., Saisse, M., et al. 2008, in SPIE Conf. Ser., 7014, 3
Drummond, J. D., & Christou, J. C. 2008, Icarus, 197, 480
Dunham, D., Herald, D., Frappa, E., et al. 2014, NASA Planetary Data System, EAR-A-3-RDR-OCCULTATIONS-V12.0
Ďurech, J., & Kaasalainen, M. 2003, A&A, 404, 709
Ďurech, J., Sidorin, V., & Kaasalainen, M. 2010, A&A, 513, A46
Ďurech, J., Kaasalainen, M., Herald, D., et al. 2011, Icarus, 214, 652
Fienga, A., Manche, H., Kuchynka, P., Laskar, J., & Gastineau, M. 2010, Scientific Notes(INPOP10a)
Fienga, A., Kuchynka, P., Laskar, J., Manche, H., & Gastineau, M. 2011, EPSC-DPS Joint Meeting 2011, 1879
Fienga, A., Manche, H., Laskar, J., Gastineau, M., & Verma, A. 2013, ArXiv e-prints [arXiv:1301.1510]
Fienga, A., Manche, H., Laskar, J., Gastineau, M., & Verma, A. 2014, ArXiv e-prints [arXiv:1405.0484]
Folkner, W. M., Williams, J. G., & Boggs, D. H. 2009, IPN Progress Report, 42, 1
Fusco, T., Rousset, G., Sauvage, J.-F., et al. 2006, Optics Express, 14, 7515
Goffin, E. 2014, A&A, 565, A56
Hezaveh, Y. D., Marrone, D. P., Fassnacht, C. D., et al. 2013, ApJ, 767, 132
Kaasalainen, M. 2011, Inverse Problems and Imaging, 5, 37
Kaasalainen, M., & Viikinkoski, M. 2012, A&A, 543, A97
Kaasalainen, M., Torppa, J., & Muinonen, K. 2001, Icarus, 153, 37
Kaasalainen, M., Torppa, J., & Piironen, J. 2002, Icarus, 159, 369
Kochetova, O. M. 2004, Solar System Research, 38, 66
Kochetova, O. M., & Chernetenko, Y. A. 2014, Solar System Research, 48, 295
Konopliv, A. S., Asmar, S. W., Folkner, W. M., et al. 2011, Icarus, 211, 401
Konopliv, A. S., Yoder, C. F., Standish, E. M., Yuan, D.-N., & Sjogren, W. L. 2006, Icarus, 182, 23
Kuchynka, P., & Folkner, W. M. 2013, Icarus, 222, 243
Lenzen, R., Hartung, M., Brandner, W., et al. 2003, in SPIE Conf. Ser. 4841, eds. M. Iye, & A. F. M. Moorwood, 944
Masiero, J. R., Mainzer, A. K., Grav, T., et al. 2012, ApJ, 759, L8
Merline, W. J., Drummond, J. D., Carry, B., et al. 2013, Icarus, 225, 794
Millis, R. L., Wasserman, L. H., Bowell, E., et al. 1981, AJ, 86, 306
Morrison, D., & Zellner, B. 2007, TRIAD Radiometric Diameters and Albedos, NASA Planetary Data System, EAR-A-COMPIL-5-TRIADRAD-V1.0
Mueller, T. G., & Lagerros, J. S. V. 1998, A&A, 338, 340
Mugnier, L. M., Fusco, T., & Conan, J.-M. 2004, J. Opt. Soc. Am. A, 21, 1841
Nesvorný, D., & Vokrouhlický, D. 2008, AJ, 136, 291
Pitjeva, E. V. 2004, in COSPAR, Plenary Meeting, Vol. 35, 35th COSPAR Scientific Assembly, ed. J.-P. Paillé, 2014
Pitjeva, E. V. 2005, Solar System Research, 39, 176
Pitjeva, E. V. 2010, in IAU Symp. 261, eds. S. A. Klioner, P. K. Seidelmann, & M. H. Soffel, 170
Pitjeva, E. V. 2013, Solar System Research, 47, 386
Rousset, G., Lacombe, F., Puget, P., et al. 2003, in SPIE Conf. Ser. 4839, eds. P. L. Wizinowich, & D. Bonaccini, 140
Russell, C. T., Raymond, C. A., Coradini, A., et al. 2012, Science, 336, 684
Ryan, E. L., & Woodward, C. E. 2010, AJ, 140, 933
Somenzi, L., Fienga, A., Laskar, J., & Kuchynka, P. 2010, Planet. Space Sci., 58, 858
Tedesco, E. F., Noah, P. V., Noah, M. C., & Price, S. D. 2004, IRAS Minor Planet Survey, NASA Planetary Data System, IRAS-A-FPA-3-RDR-IMPS-V6.0
Thomas, P. C., Parker, J. W., McFadden, L. A., et al. 2005, Nature, 437, 224
Usui, F., Kuroda, D., Müller, T. G., et al. 2011, Pub. Astron. Soc. Japan, 63, 1117
van Dam, M. A., Le Mignant, D., & Macintosh, B. A. 2004, Appl. Opt., 43, 5458
Viikinkoski, M., & Kaasalainen, M. 2014, Inverse Problems and Imaging, 8, 885
Viikinkoski, M., Kaasalainen, M., & Ďurech, J. 2015, A&A, 576, A8
Wizinowich, P. L., Acton, D. S., Lai, O., et al. 2000, in SPIE Conf. Ser. 4007, ed. P. L. Wizinowich, 2
Zielenbach, W. 2011, AJ, 142, 120

A&A 582, C1 (2015)
DOI: 10.1051/0004-6361/201526626e
© ESO 2015

Astronomy & Astrophysics

L E

VLT/SPHERE- and ALMA-based shape reconstruction of asteroid (3) Juno *(Corrigendum)*

M. Viikinkoski[1], M. Kaasalainen[1], J. Ďurech[2], B. Carry[3,4], M. Marsset[5,6], T. Fusco[6,7], C. Dumas[5], W. J. Merline[8], B. Yang[5], J. Berthier[3], P. Kervella[9,10], and P. Vernazza[6]

[1] Department of Mathematics, Tampere University of Technology, PO Box 553, 33101 Tampere, Finland
e-mail: matti.viikinkoski@tut.fi
[2] Astronomical Institute, Faculty of Mathematics and Physics, Charles University in Prague, V Holešovičkách 2, 18000 Prague, Czech Republic
[3] ACME, IMCCE, UMR 8028 du CNRS, UPMC, Université de Lille 1, 77 Av. Denfert-Rochereau, 75014 Paris, France
[4] Laboratoire Lagrange, UMR 7293 CNRS, UNS, Observatoire de la Côte d'Azur, 06304 Nice, France
[5] European Southern Observatory (ESO), Alonso de Còrdova 3107, 1900 Casilla Vitacura, Santiago, Chile
[6] Aix-Marseille University, CNRS, LAM (Laboratoire d'Astrophysique de Marseille) UMR 7326, 13388 Marseille, France
[7] ONERA – Optics Department, 29 avenue de la Division Leclerc, 92322 Chatillon Cedex, France
[8] Southwest Research Institute, 1050 Walnut St., #300 Boulder, CO 80302, USA
[9] Unidad Mixta Internacional FCA (UMI 3386), CNRS/INSU & Universidad de Chile, Las Condes, Santiago, Chile
[10] LESIA (UMR 8109), Observatoire de Paris, CNRS, UPMC, Univ. Paris-Diderot, PSL, 5 place Jules Janssen, 92195 Meudon, France

A&A 581, L3 (2015), DOI: 10.1051/0004-6361/201526626

Key words. instrumentation: interferometers – instrumentation: adaptive optics – minor planets, asteroids: individual: (3) Juno – methods: numerical – errata, addenda

A technical problem occurred during the production process: Fig. 4 was identical to Fig. 3. The correct Fig. 4 is shown here.

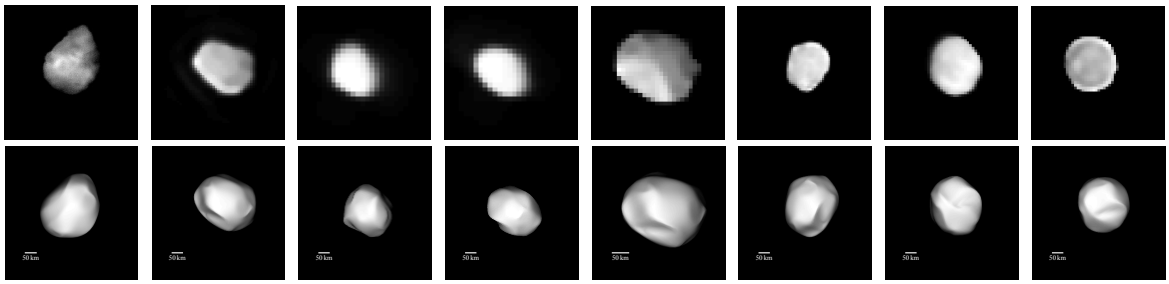

Fig. 4. Adaptive-optics images used for reconstruction (*top*) and corresponding model views (*bottom*). See Table 1 for observing conditions and instruments. The scattering law used for the shading exaggerates surface features.

Tampereen teknillinen yliopisto
PL 527
33101 Tampere

Tampere University of Technology
P.O.B. 527
FI-33101 Tampere, Finland

ISBN 978-952-15-3665-6
ISSN 1459-2045